Double longitudinal spin asymmetries in single hadron photoproduction at high p_T at COMPASS

Maxime Levillain

université PARIS-SACLAY

cea

UNIVERSITÉ PARIS SUD
Comprendre le monde, construire l'avenir®

NNT : 2015SACLXXXX

THESE DE DOCTORAT DE L'UNIVERSITE PARIS-SACLAY, préparée à l'Université Paris-Sud

ECOLE DOCTORALE N°576
Particules, Hadrons, Énergie, Noyau, Instrumentation, Imagerie, Cosmos et Simulation

Spécialité de doctorat: Physique hadronique

Par

M. Maxime Levillain

Double longitudinal spin asymmetries
in single hadron photoproduction
at high p_T at COMPASS

Thèse présentée et soutenue à Gif sur Yvette, le 21 octobre 2015

Composition du Jury:

M. B. Espagnon	Professeur, Université Paris-Saclay	Président
M. W. Vogelsang	Professeur, Université de Tübingen	Rapporteur
M. A. Magnon	Docteur, Université d'Illinois	Rapporteur
M. B. Ketzer	Professeur, Université de Bonn	Examinateur
M. D. de Florian	Professeur, Université de Buenos Aires	Examinateur
M. C. Marchand	Directeur de Recherche, LISAH	Directeur de thèse

Acknowledgements

I first would like to thank my PhD supervisor, Claude Marchand, who has been able to guide me through these three years and in particular help and correct me in the last months during the writing of my thesis, even though he had a lot of responsibilities in an other department.

My thanks goes also to Alain Magnon, without who I would not have found this project of thesis, and who has always shown a lot of interests in my work. I also thank him to have accepted to be on of the referee in the jury of this thesis and for his careful corrections and for his detail report.

I want to thanks all of the other jury members, Bruno Espagnon who accepted to preside this jury, Bernhard Ketzer and Daniel de Florian, who have been able to participate to my defense from Germany and Argentina, even though the timing was really complicated. In particular, my gratitude goes to my other referee, Werner Vogelsang, who provided me with all the information necessary for the theoretical understanding of this thesis and also welcomed me in Tübingen University to work on the comparison of the measurement and the theoretical calculations.

I also would like to thanks the members of the SPhN who welcomed me in this department. In particular Heloise Goutte, Françoise Auger and Jacques Ball who presided it; Isabelle Richard and Valérie Poyeton for their sympathy and their good mood even early in the morning; Gilles Tricoche, Stefano Panebianco and all the other physicists of the service who have followed my work and supported me during these three years and a half.

More particularly I want to thank all the COMPASS members who helped me in my work. In particular Damien Neyret who showed me all there is to know about Micromegas and allowed me to work with him; Yann Bedfer who supervised my internship and guided me in all my analysis work; Fabienne Kunne, Nicole D'Hose and Stephane Platchkov who also supported me in my work; and Eva Maria Kabuss who also supervised the analysis of asymmetries in the COMPASS collaboration.

The other members of the LPN from the COMPASS group, Franck Sabatié, Sébastien Procureur and Hervé Moutarde have also supported me or helped in the beginning of my work or during my travels for international conferences, and for this I would like to express my thanks.

Of course, I would not have survived during these three years without the company of my fellow PhD colleagues, Vincent Andrieux who has always been there to help me in my work or to spend nice moments in front of a coffee or a beer with the company of Florian Thibaud who also introduced me to the analysis of Micromegas, Lucie Grente, Quiela Curiel and Antoine Collin; those were always precious and fruitful times. I would like to thank the other PhD students, Maxime Defurne, Maxime Pequignot and Valerian Sibille with who I shared this ex-

perience. I also want to express my thanks to Erin Seder, Éric Fuchey and Heiner Wollny who helped in different times of my thesis.

I finally would like to thank all the supports that I received from my friends during these three years and in particular from Caroline Chevalier who also helped me for the correction and the page setting of this manuscript; and of course from my mother and brother and the rest of my family who has always been there for me.

Contents

Introduction

The nucleon spin structure is one of the major unresolved puzzles in hadronic physics. The sum of quark and antiquarks spin contribution to the nucleon spin, $\Delta\Sigma$, has been measured to be about 30% [1], whereas the gluon spin contribution ΔG is still not constrained enough after two decades of research. The framework of perturbative Quantum Chromodynamics (pQCD) allows to study the gluon contributions through Deep Inelastic Scattering (DIS) only through higher-order corrections to the cross section. The unpolarised gluon density $g(x_g)$, where x_g is the nucleon momentum fraction carried by the gluons, is well constrained by DIS experiments with unpolarised beam and target thanks to their high statistics and large kinematic coverage, but for polarised beam and target, the statistics is however lacking to sufficiently constrain the gluon helicity distribution $\Delta g(x_g)$. This directly leads to a not well known contribution of the gluon spin to the spin of the nucleon, $\Delta G = \int \Delta g(x_g) dx_g$, and to a lesser extent to the one of the quarks. In order to better constrain $\Delta g(x_g)$, one has to search for processes where the contributions from the gluons appear at leading order. One of the most used is the leptoproduction of hadrons at high transverse momentum p_T in the limit of collinear fragmentation.

The COMPASS collaboration has already studied the asymmetries for leading hadrons (in the sense of the higher p_T), in both the DIS and the quasi-real photoproduction regimes [2] [3]. In terms of pQCD, it is difficult to define a leading hadron cross-section [4], and therefore a model is needed to interpret the results. Some Lund Monte Carlo simulations provide the necessary information to interpret these measurements. Unfortunately such an analysis is restricted to leading order (LO) in the strong coupling constant α_S since there exists no next-to-leading order (NLO) Monte Carlo simulation for leptoproduction yet. Due to the limitation of neglecting gluon contributions at NLO, such results can not be used in recent global fits at NLO of polarised Parton Distribution Functions (PDFs) [5].

The major part of this thesis concerns a new analysis of COMPASS data for single-inclusive hadron quasi-real photoproduction at high p_T, which differs from the previous analysis of COMPASS in that all measured hadrons are taken into account (and not only leading ones). The interpretation is based on a collinear pQCD framework developed up to NLO [4], the theoretical calculations are based on the factorisation theorem to calculate the cross section of single-inclusive hadron production. This method is sensitive to ΔG not only in terms of contributions from "direct" photoabsorption on gluons, $\gamma^* g \to q\bar{q}$ (Photon Gluon Fusion), but also in terms of contributions from "resolved-photon" subprocesses, qg and gg, where the photon acts as a source of partons. Similarly, the direct process $\gamma^* q \to q\bar{q}g$ (QCD Compton) as well as resolved qq and gq subprocesses are taken into account in the theoretical calculations. The same kind of analysis has already been applied to pp collisions at $\sqrt{s} = 200$ GeV for RHIC measurements [6, 7] and bring some interesting constraints on the $\Delta g(x_g)$ distribution [5]. After comparing the prediction of this model to measurements with COMPASS unpolarised data at $\sqrt{s} = 18$ GeV [8], the applicability of this framework brings some new theoretical challenges with the accounting of "threshold resummation" at next-to-leading logarithm (NLL) [9].

This thesis is organised as follows:

- Chapter 1 deals with the theoretical framework needed to explain the analysis of asymmetries for single-inclusive hadron quasi-real photoproduction at high p_T. This includes a brief description of SIDIS framework and variables and the definition of polarised and unpolarised PDFs. The particular theoretical method is then described with a reminder of the unpolarised study and of the expectations presented in [4].
- Chapter 2 presents an overview of the experimental setup of COMPASS, with an emphasis on the polarised beam and targets important for this analysis, as well as on the RICH detector used for the particle identification.
- Chapter 3 is a presentation of a particular tracking detector of COMPASS, the new pixel Micromegas. This includes an overview of gaseous detector history and presentation of former Micromegas. A study of the detector performances is also performed.
- Chapter 4 deals with all the analysis performed to extract the asymmetries from COMPASS data. The calculations and the data selection are first explained, then an accurate systematic study is performed. The results are then presented for unindentified hadrons and then for identified hadrons with an explanation of how the identification is performed.
- Chapter 5 presents the comparison of the experimental results with theoretical calculations, leading to an evaluation of $\int_{0.07}^{0.25} dx_g \Delta g(x_g)$ from these measurements.

Chapter 1

Theoretical Framework

In this chapter, we present the theoretical framework used in Chap. 5 for the interpretation of the double longitudinal spin asymmetries for quasi-real photoproduction at high-p_T.

We will first describe the different physical processes that come to play in Deeply Inelastic Scattering (DIS) in the framework of collinear pQCD. Although the asymmetries measured in quasi-real photoproduction regime do not fall per se in the DIS categorisation, the overall pQCD framework still holds.

We will then detail the nucleon structure description and emphasise the importance of constraining the quarks and especially the gluon helicity distributions.

Finally we describe theoretical calculations performed for the interpretation of the asymmetries, as well as the checks performed on unpolarized data to verify the applicability of the theory at low COMPASS center of mass energy.

1.1 Lepton-Nucleon Scattering at Hard Scales

1.1.1 Semi-Inclusive Deep Inelastic Scattering Framework and Variables

At COMPASS, we will study the lepton-nucleon scattering through the Deep Inelastic Scattering (DIS) framework [10, 11], where a lepton beam scatters off a nucleon target: $l + N \rightarrow l' + X$. By requiring to detect a hadron in the final state, one talks about Semi-Inclusive Deep Inelastic Scattering (SIDIS) $l + N \rightarrow l' + h + X$, as opposed to inclusive scattering where the hadronic final state is ignored.

The interaction between the lepton l and the partons of the nucleon N takes place via a virtual photon γ^*. The simplified Feynman diagram of a SIDIS process is shown in Fig. 1.1.

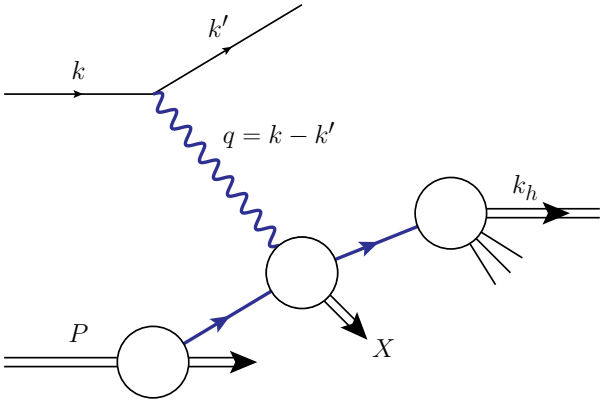

Figure 1.1: Feynman diagram of SIDIS

All the 4-momenta of the initial state and final state particles are known except for the particles comprised in X. Since COMPASS is a fixed target experiment the nucleon 4-momentum can be written $P = (M, \vec{0})$. All the common variables of DIS and SIDIS are summarised in Tab. 1.1.

variable	expression	signification
P	$(M, \vec{0})$	nucleon 4-momentum
k	$(E, \vec{k})$	incoming lepton 4-momentum
k'	$(E', \vec{k'})$	scattered lepton 4-momentum
q	$k - k'$	virtual photon 4-momentum
ν	$E - E'$	energy loss of the lepton
y	ν/E	fractional energy loss of the lepton
Q^2	$-q^2$	"virtuality" of the photon
x_{Bj}	$Q^2/2M\nu$	Bjorken variable
w^2	$(P+q)^2$	squared invariant mass of the hadronic system
k_h	$(E_h, \vec{k_h})$	final state hadron 4-momentum
p_T	$\|\|\vec{k_h} - \vec{q}(\vec{k_h} \cdot \vec{q})/\|\|\vec{q}\|\|^2\|\|$	transverse momentum of the final state hadron
θ_h		final state hadron angle w.r.t. the virtual photon
η_h	$-log(tan(\theta_h/2)) - 0.5\, log(2E/M)$	final state hadron pseudorapidity in the c.m.s.
z	E_h/E	fractional energy of the final state hadron

Table 1.1: Common variables of DIS and SIDIS (in the laboratory frame if not specified)

The virtuality of the photon Q^2, which is the negative of the four momentum transfer squared of the virtual photon, characterises the domain separation between DIS regime ($Q^2 \gtrsim 1$ GeV^2) and the quasi-real photoproduction regime ($Q^2 \lesssim 1$ GeV^2), which will be the domain studied in the analysis of this thesis. The hard scale necessary in the factorisation and renormalisation schemes, which is provided by Q^2 in the DIS regime, is in this study given by the transverse momentum of the final state hadron ($p_T > 1$ GeV/c).

The Bjorken scaling variable x_{Bj}, comprised between 0 and 1, represents the elasticity of the event. In the parton model it can be interpreted as the fraction of the nucleon momentum carried by the parton responsible of the interaction.

The pseudo-rapidity η_h of the final state hadron plays also a particular role in this analysis. It is comprised in this analysis between -0.1 and 2.4, the negative values correspond to large angles of the hadrons, whereas the large positive values are for small angles.

1.1.2 Wigner Distributions and Integrated Distributions

The study of the structure of the nucleon goes through the modelisation of his non-perturbative structure. Partons inside the nucleon can have a specific momentum at a specific position, hence their state can be described in six dimensions by the so called Wigner distributions $W(\vec{r}, \vec{k})$, where $\vec{r}$ is the position vector and $\vec{k}$ is the 3-momentum vector. Heisenberg's uncertaintiy relations prevent these distributions from being real probability distributions, they are only defined as quasi-probability distributions since they are not positive definite. These distributions can be reduced to a five dimensions distributions in the infinite momentum frame: $W(x, k_\perp, b_\perp)$ where x is the longitudinal momentum, $k_\perp$ the momentum in the transverse plane and $b_\perp$ the position in the transverse plane (or impact parameter) [12]. Naturally the experiments cannot probe the structure of the nucleon for all these dimensions at the same time. By integrating or projecting the Wigner distributions, like described in Fig. 1.2, one can obtain all the distributions studied in actual experiments.

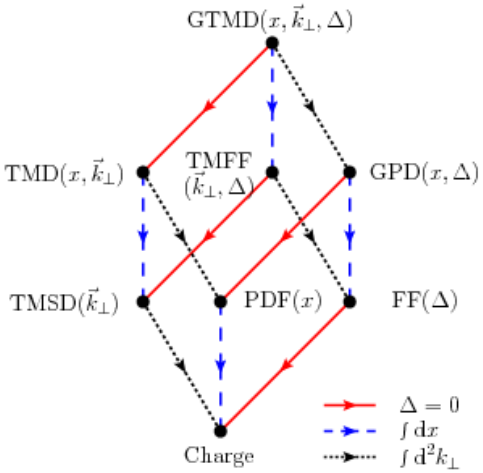

Figure 1.2: Illustration of the decomposition of the different distributions from the Wigner distributions. Δ is the Fourier conjugate of $b_\perp$ and setting it to 0 amounts to the same thing as integrating over $b_\perp$ [12]

By integrating over the position or momentum variables, one can find back genuine probability distributions. One will just describe the four most famous ones:

Transverse Momentum-dependent Distributions (TMDs)

These TMDs can be obtained by integrating $b_\perp$: $f(x, k_\perp)$. They can be interpreted as quark densities in the 3-dimensional momentum space.

Generalised Parton Distributions (GPDs)

By integrating over $k_\perp$, one obtains the GPDs: $f(x, b_\perp)$. These distributions can be studied through Deeply Virtual Compton Scattering (DVCS) or Deeply Virtual Meson Production (DVMP).

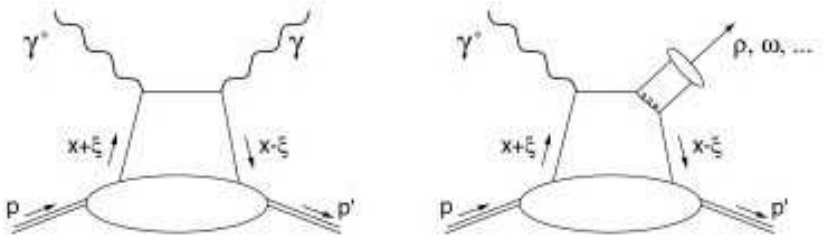

Figure 1.3: Feynman diagram for DVCS (left) and DVMP (right) processes

Form Factors (FFs)

The form factor distributions $F(b_\perp)$ were the first one to be studied [13], they can be interpreted as electric charge and electric current distribution in space (for the electric G_E and magnetic G_M form factor). They can also regrouped as structure functions F_1, F_2 and F_3.

Parton Distribution Functions (PDFs)

Finally the one we need and the one we study, the PDFs can be extracted from the Wigner distributions by integrating over $k_\perp$ and $b_\perp$. As the form factors, it is a one dimensional distribution. The experiment providing the data to extract these distributions will be more detailed in the next section, as well as the final results of global fits.

1.1.3 Unpolarized PDFs

The PDFs represent the probability densities in the nucleon as function of the momentum fraction for each quark f_q (or q to simplify) and antiquark $f_{\bar{q}}$ ($\bar{q}$) flavor and for the gluon f_g (g). These densities respect a simple 0^{th} moment sum rule:

$$\int_0^1 \left(\sum_{q\in\{u,d,s,c\}} [q(x) + \bar{q}(x)] + g(x) \right) dx = 1 \tag{1.1}$$

The interactions between partons in the nucleon are mainly ruled by QCD (Quantum Chromodynamics), the main feature of these interactions being the asymptotic freedom discovered in 1973 [14]. This property leads to the introduction of a hard scale μ^2 for the non-perturbative distributions ($f(x, \mu^2)$), knowing that with $\mu^2 \to \infty$, these distributions should tend to the perturbative calculations. The evolution of these distributions with μ^2 is governed by the DGLAP equations [15].

The first parameterisation of these PDFs were computed around 1978 [16] for SLAC and Fermilab data, as illustrated in Fig. 1.4.

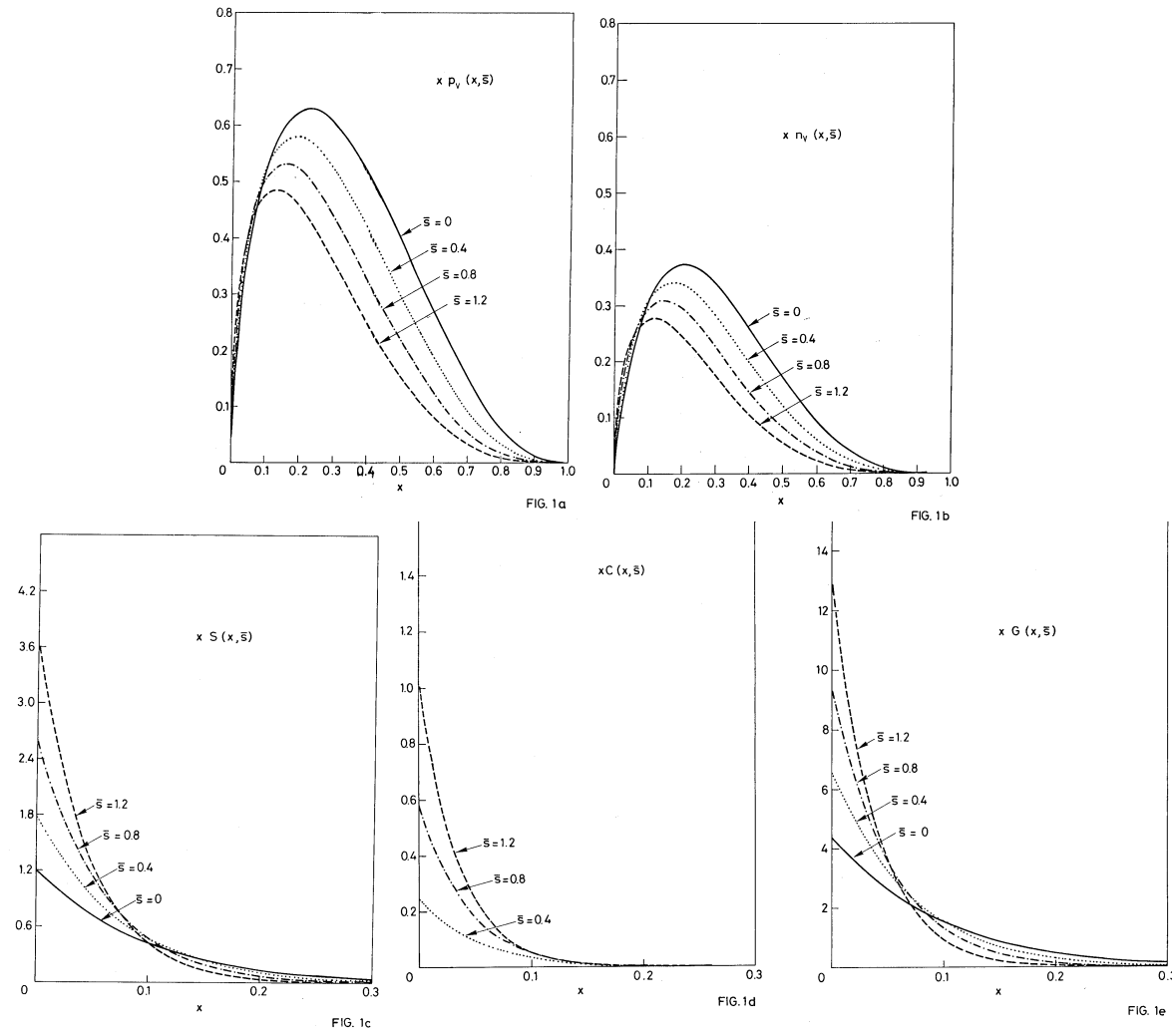

Figure 1.4: First parameterisations of PDFs depending on $\bar{s}$ (quarks of proton, quarks of neutron, non charmed sea quarks, charmed sea quarks, gluons) [16]

Nowadays the PDFs are determined by world data fits. The most famous ones are CTEQ, MSTW and NNPDF, which use not only DIS data but also Drell Yan production, hadron-electron collision (HERA), hadron-hadron collision (LHC). The range of μ^2 goes from 1 GeV^2 to 10^{10} GeV^2. Fig. 1.5 shows the PDF for all partons for NNPDF2.3 fit.

1.1.4 Polarized PDFs and the Gluon Contribution to the Spin Crisis

In the same way as for the unpolarised PDFs, one can investigate the probability densities of spin or helicities in the nucleon as function of the momentum fraction for each quark Δf_q (or Δq to simplify) and antiquark $\Delta f_{\bar{q}}$ ($\Delta \bar{q}$) flavor and for the gluon Δf_g (Δg), through what is called polarised PDFs. Respecting the fermionic or bosonic property of the different particles, the helicities follow the first moment rule:

$$\frac{1}{2} = \int_0^1 dx \frac{1}{2}\Big(\sum_{q\in\{u,d,s,c\}} \Delta q(x) + \Delta\bar{q}(x)\Big) + \Delta g(x) + L_{q,g} \tag{1.2}$$

$$= \frac{1}{2}\Delta\Sigma + \Delta G + L_{q,g} \tag{1.3}$$

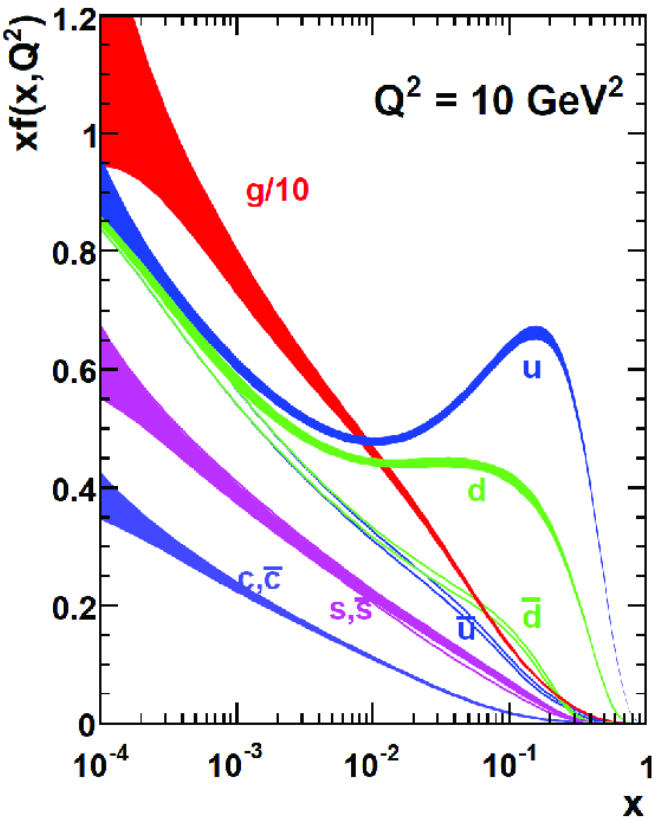

Figure 1.5: NNPDF2.3 PDFs set at $\mu^2 = 10$ GeV^2 with error bands corresponding to a one sigma interval

, where L_{q+g} is the relativistic contribution from the orbital momentum of quarks and anti-quarks and gluons.

The first experiments to study nucleon spin structure were E130 at SLAC in the early 1980's followed by EMC at CERN. The latter experiment found out that the quark contribution were lower than expected in the prediction of Ellis-Jaffe sum rule [17]: $\Delta\Sigma \approx 0.12$.

These results led to the "spin crisis", and other experiments were planned to find out from where this unexpected distribution of the nucleon spin comes from: gluons, strange quarks or orbital momenta. Among these experiments one can cite HERMES, STAR, PHENIX and COMPASS.

As showed in Fig. 1.6, the quark contribution is now relatively well known and has been evaluated as $\Delta\Sigma \approx 0.3$ [19]. However the contribution from the quarks of the sea: $\Delta\bar{u}$, $\Delta\bar{d}$, Δs and $\Delta\bar{s}$ are less constrained [18] and one needs more results to separate for instance Δs from $\Delta\bar{s}$.

The gluon polarisation remains one of the major insufficiently constrained piece of the nucleon puzzle. The most recent results from world data fits seem to tend to a positive ΔG with the inclusion of new data from RHIC [5], but the uncertainties remain strong and the possibility of a changing sign gluon helicity distribution is not yet ruled out [18].

Fig. 1.7 shows the current COMPASS results for the gluon polarisation $\Delta G/G$ at LO (high p_T analysis) and NLO (open charm analysis) compared to SMC and HERMES results and also to DSSV08 and LSS10 world data fits.

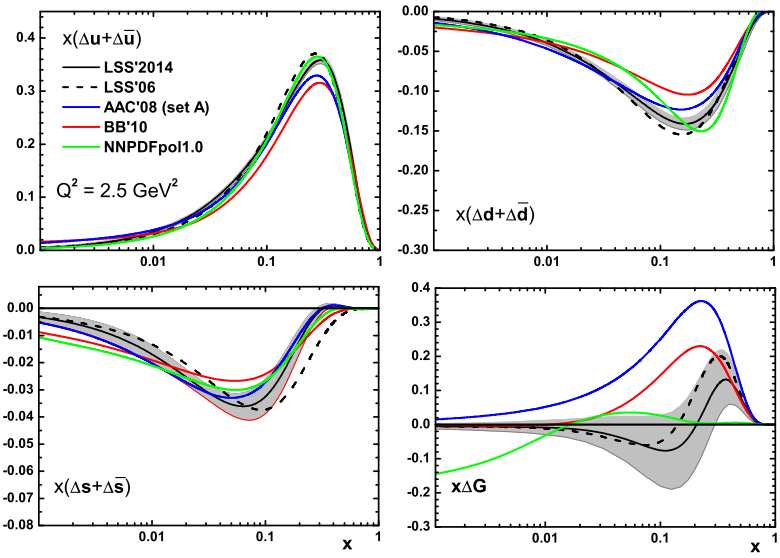

Figure 1.6: Polarised PDFs ($\Delta u + \Delta\bar{u}$, $\Delta d + \Delta\bar{d}$, $\Delta s + \Delta\bar{s}$ and Δg at $\mu^2 = 2.5$ GeV^2) for different fits [18]

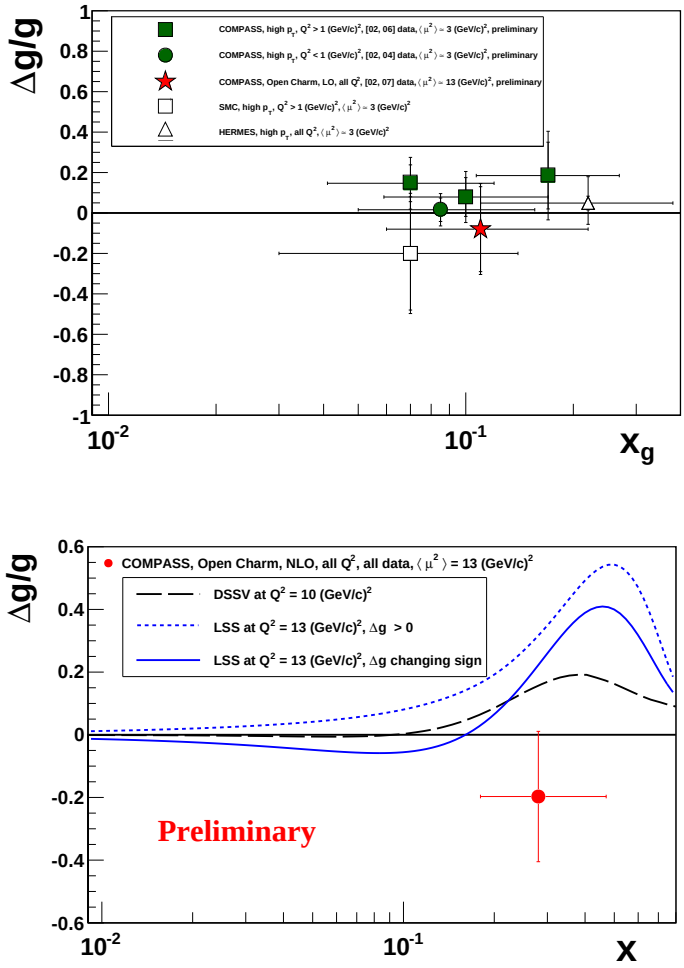

Figure 1.7: Direct measurements of $\Delta G/G$ via Photon Gluon Fusion. On the left: : LO extraction from open charm [20] and high p_T [21, 22], and on the right: first NLO extraction from open charm at COMPASS [23], compared to DSSV [19] and LSS [24] global fits

1.2 Theoretical Framework for Double Spin Asymmetries at high p_T

1.2.1 Different Processes in the Photoproduction Regime

The studies of hadron-pair production $l + N \rightarrow l' + h_1 + h_2 + X$ done at HERMES and COMPASS focusing on the signatures of the Photon Gluon Fusion (PGF) (Fig. 1.8) lead to rather complex calculations which are still lacking at Next-to-Leading Order (NLO) in α_S (coupling constant of the strong interaction).

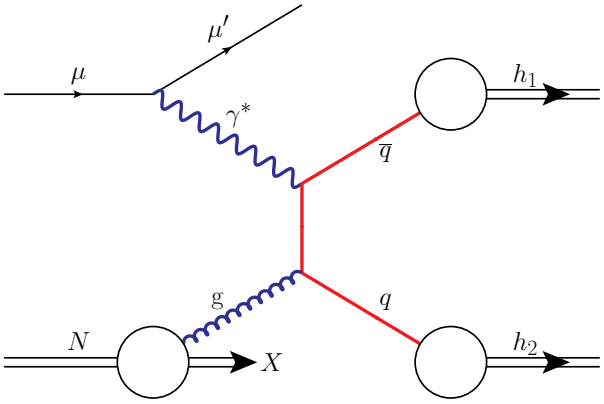

Figure 1.8: Feynman diagram of the Photon Gluon Fusion (PGF)

The regime of quasi-real photoproduction for single-inclusive hadrons allows calculations at NLO and has the advantage of much higher rates than DIS electroproduction of hadrons. Unfortunately this regime involves also the inclusion of other processes called resolved processes (in opposition to direct processes) where the virtual (quasi-real) photon fluctuates into a hadronic state as illustrated in Fig. 1.9 (for review, see [25]). In the left figure (resolved contribution), the a stands a parton.

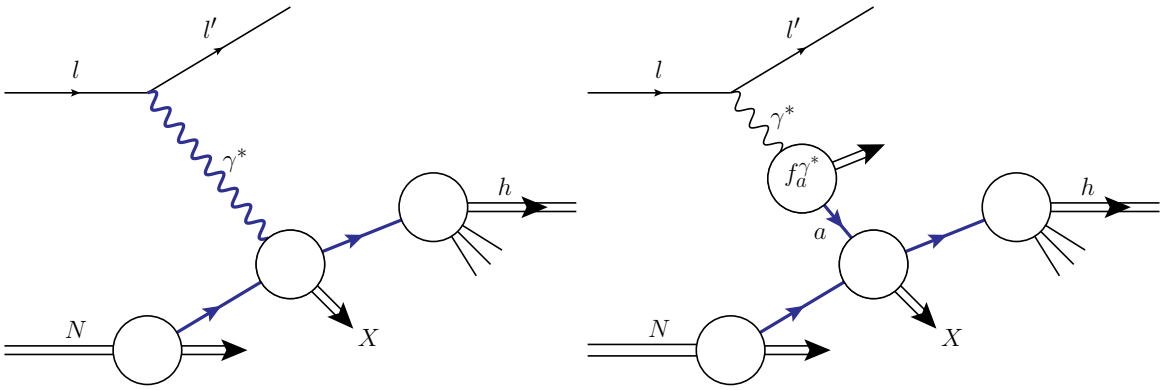

Figure 1.9: Feynman diagrams for the direct (left) and resolved (right) processes

The calculation of resolved processes cross-sections requires the knowledge of parton density $f_a^{\gamma^*}$ and helicity $\Delta f_a^{\gamma^*}$ distributions. The parton density distributions are shown in Fig. 1.10 at a reference scale $\mu^2 = 5$ GeV^2. The helicity distributions are unfortunately lacking at the moment and one chose two different parameterisations to be used as uncertainties $\Delta f_a^{\gamma^*} = 0$ and $\Delta f_a^{\gamma^*} = |f_a^{\gamma^*}|$. One will later see that these uncertainties do not impact too much the study on the nucleon helicity structure [4].

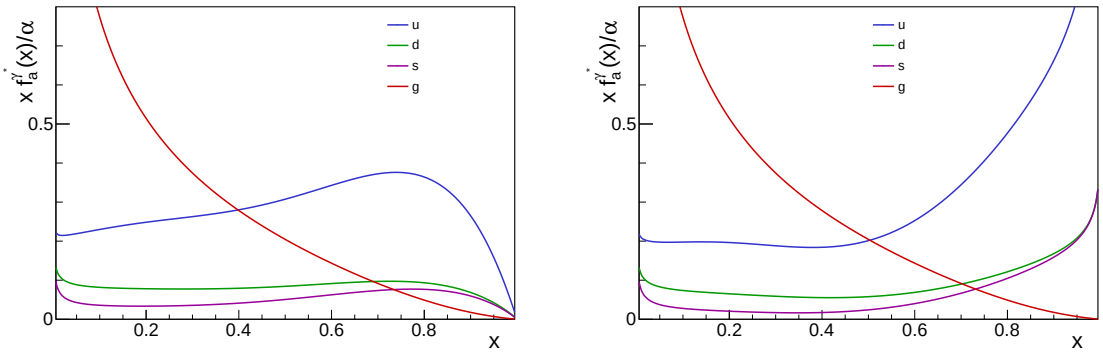

Figure 1.10: Parton density functions of a virtual photon at $\mu^2 = 5$ GeV^2 originally performed in DIS$_\gamma$ scheme (left) and recalculated in $\overline{MS}$ scheme (right) from GRV analysis [26]

1.2.2 Details of Calculations of Cross-sections and Asymmetries

Calculation of Theoretical Cross-sections

Cross-sections of SIDIS processes depends on PDFs and one can express the first one with the latter depending on the theoretical hypotheses we choose. In a reverse process, one can extract the PDFs from the measurements of cross-section. These theoretical calculations are based on the framework described in [4].

The choice of the quasi-real photoproduction regime for hadron at high transverse momentum allows to theoretically calculate the partonic cross-sections at NLO and express the SIDIS cross-sections as a function of p_T and η_h, using non-perturbative parameterisation for the description of the nucleon, the virtual photon in the resolved processes and the fragmentation of the partons into hadrons Eq. 1.5:

$$d\sigma^{SIDIS}(p_T,\eta_h) = \sum_{a,b,c}\int dx_a dx_b dz_c f_a^{\mu}(x_a,\mu_f) f_b^{N}(x_b,\mu_f) d\hat{\sigma}_{ab\to cX}(s,x_a,x_b,p_h,z_c,\mu_r,\mu_f,\mu_f') D_c^h(z_c,\mu_f') \quad (1.4)$$

$$d\sigma^{SIDIS}(p_T,\eta_h) = \sum_{a,b,c} f_a^{\mu}\otimes f_b^{N}\otimes d\hat{\sigma}_{ab\to cX}\otimes D_c^h \quad (1.5)$$

, where a is the virtual photon in direct processes and a parton from the virtual photon in the resolved processes, b is the parton probed in the nucleon (and x_b its fraction of the nucleon momentum), c is the parton coming from the partonic reaction $a + b \to c + X$ (and z_c the fraction of parton c's momentum taken by the hadron h), μ corresponds to the incoming muon, N is the nucleon, and h is the single inclusive hadron detected (and p_h its momentum). s is the *cms* energy and μ_r, μ_f and μ_f' are the scales of the renormalisation, and the factorisation of the different part of the processes. These factors are arbitrary but have to be of the order of the hard scale. Here they are chosen to be equal: $\mu_r = \mu_f = \mu_f' = p_T$.
The SIDIS cross-section is calculated as a convolution of $d\hat{\sigma}$ or $d\hat{\sigma}_{ab\to cX}$ (Fig. 1.11) representing the perturbative partonic cross-section with several non-perturbative distributions:

- the nucleon PDFs f_b^N already detailed in the previous sections Sec. 1.1.3.
- the fragmentation functions (FFs) D_c^h which describe the fragmentation of a parton c into a hadron h
- the "muon PDFs" f_a^{μ} which can be described as the convolution of a Weizsäcker-Williams probability $P_{\gamma\mu}$ to produce a virtual photon in a quasi-real photoproduction regime with a photon-parton density $f_a^{\gamma}(x_a,\mu_f)$ ([27]):

$$f_a^{\mu}(x_a) = \int_{x_a}^{1}\frac{dy}{y} P_{\gamma\mu} f_a^{\gamma}(x_\gamma = \frac{x_a}{y}) \quad (1.6)$$

, with

$$P_{\gamma\mu}(y) = \frac{\alpha_e}{2\pi}\left(\left(\frac{1+(1-y)^2}{y}\cdot ln\frac{Q^2_{max}(1-y)}{m_\mu y^2}\right) + 2m^2_\mu y\left(\frac{1}{Q^2_{max}} - \frac{1-y}{m^2_\mu y^2}\right)\right) \tag{1.7}$$

The distribution f_a^γ differentiates between the direct and resolved processes:

- for the direct photon contribution, the parton a has to be identified with an elementary photon, so that x_a must be identified with y. One gets:

$$f_a^\gamma = \delta(1-x_\gamma) \tag{1.8}$$

- for the resolved photon contribution, f_a^γ represents the parton densities of a circularly polarised photon, as presented in Sec. 1.2.1. These distributions are decomposed into a photonic part perturbatively calculable and a hadronic non-perturbative part. The photonic part dominates at large momentum fraction x_γ

The separation of these processes leads to express the measured cross-section as the sum of a direct and resolved photon contributions:

$$d\sigma^{SIDIS} = d\sigma^{SIDIS}_{dir} + d\sigma^{SIDIS}_{res} \tag{1.9}$$

All these notations are illustrated in the reminder figures Fig. 1.11.

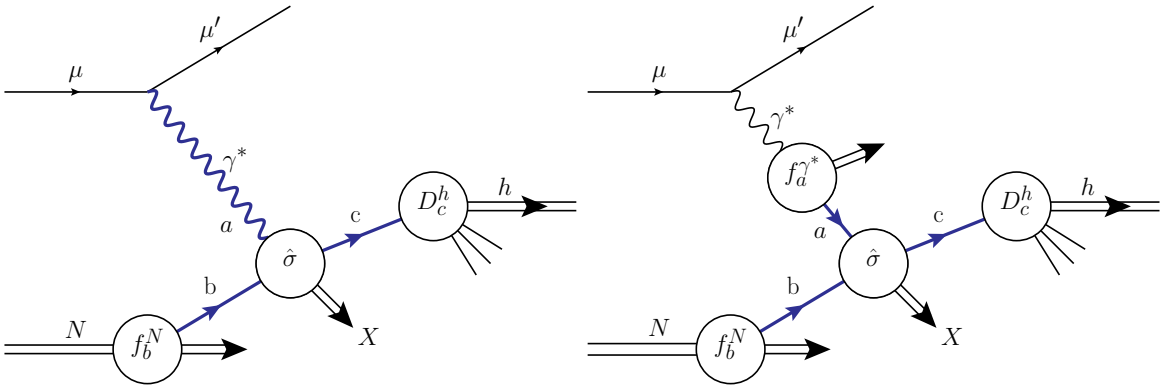

Figure 1.11: Feynman diagrams for the direct (left) and resolved (right) processes

Calculation of Asymmetries

To describe the theoretical asymmetries calculations, one first needs to define the differential polarised cross-sections $d\Delta\sigma^{SIDIS}$. Using the same formalism as for the unpolarised cross-sections, it can be expressed as:

$$d\Delta\sigma^{SIDIS}(p_T,\eta_h) = \sum_{a,b,c}\Delta f_a^\mu \otimes \Delta f_b^N \otimes d\Delta\hat{\sigma}_{ab\to cX} \otimes D_c^h \tag{1.10}$$

For the nucleon part, the polarised parton distribution Δf_b^N is defined as:

$$\Delta f_b^N(x_b,\mu_f) = f^N_{b+}(x_b,\mu_f) - f^N_{b-}(x_b,\mu_f) \tag{1.11}$$

, where the subscripts $+$ and $-$ indicate the helicity of the parton b in the nucleon N of positive helicity. For the virtual photon part, the polarised Weiszäcker-Williams probability $\Delta P_{\gamma\mu}$ ([27]) is slightly different from the unpolarised one and is expressed as:

$$\Delta P_{\gamma\mu}(y) = \frac{\alpha_e}{2\pi}\left(\left(\frac{1-(1-y)^2}{y}\cdot ln\frac{Q^2_{max}(1-y)}{m_\mu y^2}\right) + 2m^2_\mu y^2\left(\frac{1}{Q^2_{max}} - \frac{1-y}{m^2_\mu y^2}\right)\right) \tag{1.12}$$

And as previously mentioned in Sec. 1.2.1, the helicity parton distribution of the virtual photon is unknown, so that the polarized cross-sections are computed with two different parameterisations taken at reference scale as $\Delta f_a^{\gamma^*}(x,\mu_0^2) = 0$ and $\Delta f_a^{\gamma^*}(x,\mu_0^2) = |f_a^{\gamma^*}(x,\mu_0^2)|$ and evolved with DGLAP equations. The difference between the asymmetries with these two distributions is used as uncertainty.

Finally, one can compute the asymmetries:

$$A_{LL}(p_T,\eta_h) = \frac{d\Delta\sigma^{SIDIS}}{d\sigma^{SIDIS}} = \frac{\sum_{a,b,c}\Delta f_a^{\mu}\otimes\Delta f_b^{N}\otimes d\Delta\hat{\sigma}_{ab\to cX}\otimes D_c^h}{\sum_{a,b,c} f_a^{\mu}\otimes f_b^{N}\otimes d\hat{\sigma}_{ab\to cX}\otimes D_c^h} \tag{1.13}$$

1.2.3 Benchmarking the Model on Unpolarised Cross-sections

Following the advice of the article [4] to verify the applicability of the this theoretical framework to the COMPASS kinematic domain, a study on unpolarised cross-section was performed by C. Höppner and A. Morreale presented in [8].

Some different parameter were used for this study:

- Since it is an unpolarised study, the acceptance of the spectrometer limited by the aperture of the polarised target could be expanded (one does not need the same acceptance for the different cells of the target) to $0.01 < \theta_h < 0.12$rad, which gives an integration domain for η_h of [-0.1,2.4].
- for analysis purposes which are explained in Sec. 4.2.3, a selection on the hadron fractional energy $0.2 < z < 0.8$.
- finally since the statistics are not an issue for the measurement of unpolarised cross-section, the previous cuts were made more strict: $Q^2 < 0.1$ GeV^2 and $0.2 < y < 0.8$

Fig. 1.12 shows the measurements of COMPASS cross-section for the reaction $\mu d \to \mu' hX$ compared to three theoretical calculations at different order of corrections, whose uncertainties come from varying the hard scale factor from $\mu^2 = p_T^2/4$ to $\mu^2 = 4p_T^2$. LO and NLO calculations show to be significantly lower (by a factor 3-4 for the NLO) than the measured cross-section. This issue which has an increasing impact when one goes to low center of mass energies had already been seen in [28, 29]. To reconcile the theory and the measurements, the calculations were improved by including an all-order resummation of threshold logarithm, which are related to soft gluon emissions and are performed up to next-to-leading logarithm (NLL) accuracy.

These last calculations are still in below the measurements by a factor 2, but they agree within the hard scale uncertainties.

y-dependent Cross-sections

Several other studies were performed to see the impact of the resummation calculation on its comparison with the measurements. In particular since the partonic center of mass energy $\sqrt{s}$ is correlated to the square root of the fractional energy loss $\sqrt{y}$ of the muon, it is specially interesting to look at the y-dependent cross-sections.

Fig. 1.13 shows the ratio of these cross-sections over the different versions of the theoretical calculations. One can clearly note the rising discrepancy between experiment and theory at low y for the NLO calculations. This worrying shape is well corrected by the resummation calculations, which give a much flatter ratio of 2 as a function of y.

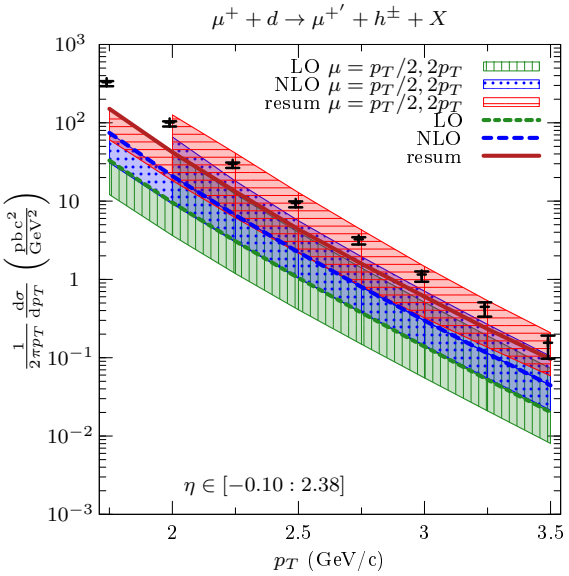

Figure 1.12: Unpolarised cross-sections as a function of p_T integrated over η_h. The theoretical calculations are presented at three different order (LO: red, NLO: blue, resum: red) with uncertainties corresponding to the scale factor uncertainty between $\mu^2 = p_T^2/4$ and $\mu^2 = 4p_T^2$. The measurements of COMPASS are presented in black [8]

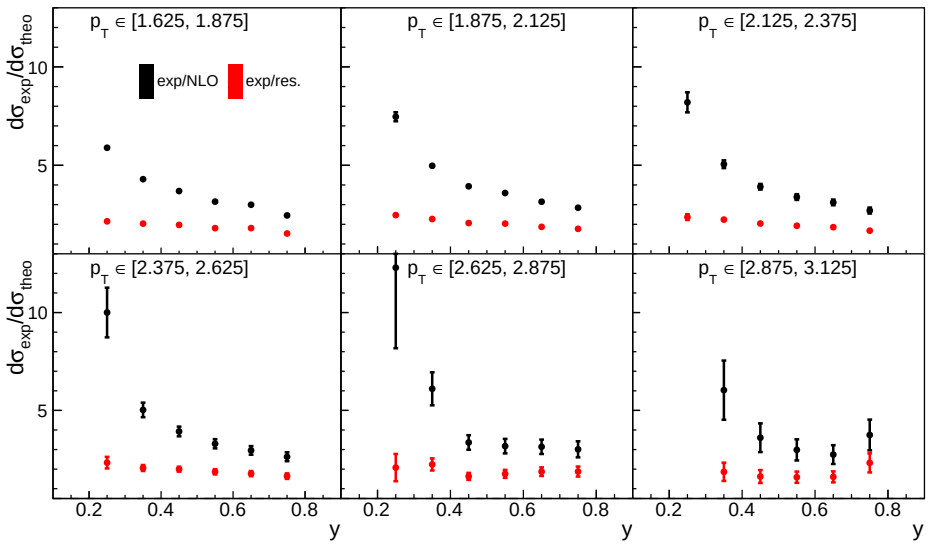

Figure 1.13: ratio of y-dependent cross-section measured at COMPASS over theoretical calculations for 5 bins of p_T for both NLO and resummed calculations [9] [30]

η-dependent Cross-sections

Since the theoretical calculations and the measurements only agrees within a factor 2, it is more important to search for agreement of the shape of the cross-sections. The calculations are done with two fundamental variables p_T and η_h, one can then study the shape of the cross-sections as a function of p_T for different η_h bins.

The theoretical curves with logarithmic resummation describe well the different steepnesses

of the p_T slopes of the cross sections for the different bins of pseudorapidities. Moreover the factor between theory and experiment remains the same for all these bins. This is a positive indication for the consistency of the theoretical calculation applicability to the COMPASS kinematic domain.

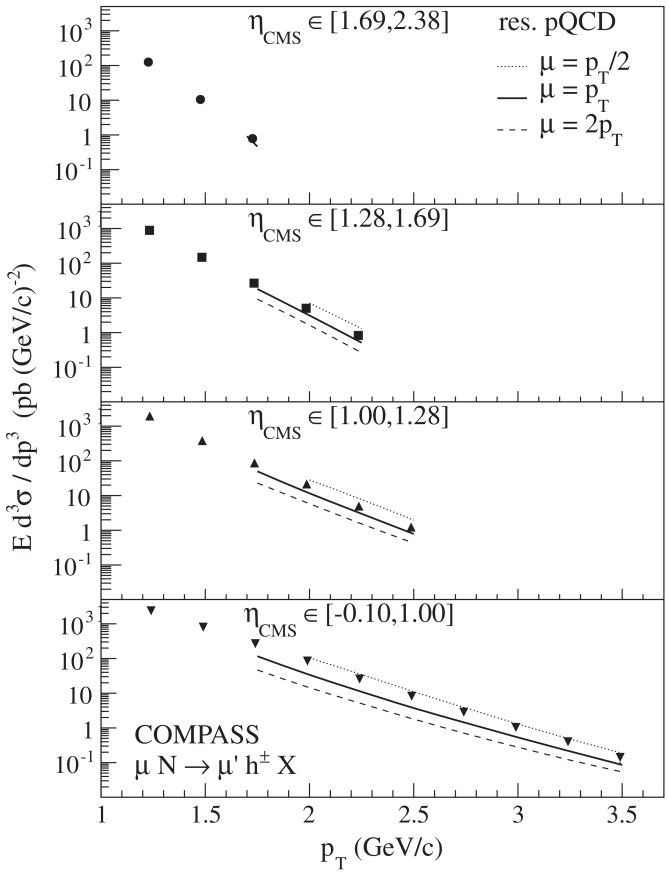

Figure 1.14: COMPASS cross-section in 4 bins of η_h compared to theoretical calculations with logarithmic resummation [8]

In the thesis [30], the measurements are shown with a comparison to only NLO theoretical predictions. The agreement between the curves are worse than with the ones shown here. In particular, one can see that the impact of resummation is stronger à low η_h.

1.2.4 Threshold Gluon Resummation

The cross-sections observable at COMPASS go to relatively low hard scale, $p_T = 1$ GeV/c, which brings the applicability of perturbative QCD (pQCD) to its limits. The value of the hadron's transverse momentum over the available center-of-mass energy $\sqrt{s}$ is relatively large, typically $x_T = 2p_T/\sqrt{s} \in [0.1, 0.5]$. Hence the partonic cross section is close to the threshold. All the partonic center-of-mass energy is just used to produce the high-transverse momentum parton, that one observes through its hadronisation (and also an other complementary parton). Other real gluon radiation is strongly suppressed and it is therefore mostly constrained to the emission of soft and/or collinear gluons. Hence the cancellation of infrared singularities leaves behind large logarithmic corrections for all orders of the form:

$$\alpha_S^k ln^{2k}(1 - x_T^2) \tag{1.14}$$

To take into account these large logarithms, a technique called *threshold resummation* first developed for Drell-Yan processes [31, 32] can be used for SIDIS processes. For these particular processes, double and single-logarithmic corrections appear from the NLO expression of the cross-section. Since the NLO calculations are done as a function of p_T and η_h, the resummation were performed with the same requirement following the techniques developed in [33]. The cross-section expressed in Eq. 1.4 is reminded with more details:

$$\frac{Ed^3\sigma}{dp^3} = \sum_{a,b,c} \int_{x_l^{min}}^1 dx_l \int_{x_n^{min}}^1 dx_n \int_x^1 dz \frac{\hat{x}_T^4 z^2}{16v\pi^2 p_T^4} f_a^l(x_l, \mu_{fi}) f_b^N(x_n, \mu_{fi}) D_h^C(z, \mu_{ff}) \frac{\hat{s} d\hat{\sigma}_{ab\to cX}}{dvdw} \tag{1.15}$$

, where $\mu_{fi} = \mu_{ff} = p_T$ are the factorisation scales, $x_{l,n}$ are the lepton and nucleon momentum fraction carried by the partons a and b, z the momentum fraction carried by the parton c. The lower bounds in the integration over the various momentum fractions are given in Eq. 1.16:

$$x_l^{min} = \frac{x_T e^{\eta}}{2 - x_T e^{-\eta}}, \;\; x_n^{min} = \frac{x_T e^{-\eta}}{2 - \frac{x_T}{x_l} e^{\eta}}, \;\; x = \frac{x_T cosh\hat{\eta}}{\sqrt{x_n x_l}} \tag{1.16}$$

$\hat{s} = x_n x_l s$ is one of the Mandelstam variables, $\hat{\eta}$ and $\hat{x}_T$ are the partonic counterparts to the pseudorapidity η and the hadronic scaling variable $x_T = 2p_T/\sqrt{s}$.

$$\hat{\eta} = \eta + \frac{1}{2} ln \frac{x_n}{x_l}, \;\; \hat{x}_T = \frac{x_T}{z\sqrt{x_l x_n}} \tag{1.17}$$

The common variables for the partonic cross-section, v and w are expressed as:

$$v = 1 - \frac{\hat{x}_T}{2} e^{-\hat{\eta}}, \;\; w = \frac{1}{v} \frac{\hat{x}_T}{2} e^{\hat{\eta}} \tag{1.18}$$

To speed up and facilitate these calculations, the z integration of the cross-sections and the resummation calculations are performed in the Mellin Space where the factorisation of the cross-section to logarithmic accuracy is possible:

$$\frac{Ed^3\sigma}{dp^3} = \sum_{a,b,c} \int_{x_l^{min}}^1 dx_l \int_{x_n^{min}}^1 dx_n \int_0^1 \frac{dN}{2\pi i} (x^2)^{-N} (D_h^c)^{2N+3} (\mu_{ff}) \tilde{w}^{2N}(\hat{\eta}) \tag{1.19}$$

, where $(D_h^c)^N(\mu_{ff})$ are the Mellin moments of the fragmentation function (Eq. 1.20), which tame the behavior of the cross-section in the Mellin space $\tilde{w}^{2N}(\hat{\eta})$ at large N.

$$(D_h^c)^N(\mu_{ff}) = \int_0^1 dz z^{N-1} D_h^c(z, \mu_{ff}) \tag{1.20}$$

The details on the factorisation of the cross-section and the computation are described in [9].

To make the best use of the already known cross-sections at NLO, the resummed cross-sections are matched with the NLO ones by subtracting the expansion of the resummed cross-sections to the first non-trivial order in α_S from the resummed cross-sections and adding the NLO cross-sections:

$$\frac{Ed^3\sigma^{matched}}{dp^3} = \sum_{a,b,c} \int_{x_l^{min}}^1 dx_l \int_{x_n^{min}}^1 dx_n \int_0^1 \frac{dN}{2\pi i} (x^2)^{-N} (D_h^c)^{2N+3} (\mu_{ff}) \tag{1.21}$$

$$\times [\tilde{w}^{resum,2N}(\hat{\eta}) - \tilde{w}^{resum,2N}(\hat{\eta})|_{firstorder}] \tag{1.22}$$

$$+ \frac{Ed\sigma^{NLO}}{d^3p} \tag{1.23}$$

1.2.5 Predictions of the model for COMPASS asymmetries at high p_T

The first theoretical calculations for single hadron production at high p_T in quasi-real photoproduction were done in 2004-2005 and presented in [4]. This article presents the overall theoretical framework, as well as predictions for unpolarised and polarised cross-sections, as well as asymmetries, for both COMPASS and HERMES. In this section, using the code provided by the authors of [4] we present the expected cross-sections and asymmetries for the COMPASS experiment. The code allows to adjust parameters or cuts on kinematic variables, the PDFs and FFs can also be changed. In particular, using different sets of polarised PDFs will allow us to compute the asymmetries for different hypotheses of Δg parameterisation.

The kinematic parameters and cuts used for the predicted COMPASS asymmetries published in [4], and redone by us as a cross check are:

- $p_\mu = 160$ GeV/c, which corresponds to an energy in the center of mass system of 18 GeV.
- Q^2_{max} is chosen to ensure the photoproduction regime for the Weizsäcker-Williams probability. In [4], it is 0.5 GeV^2.
- $0.2 < y < 0.9$ to avoid the dilution of the photon polarisation at low y which would increase the uncertainties of the asymmetries.
- The cross-sections are integrated over η_h from 0.44 to 2.4 in the center of mass system, which corresponds to $0.01 < \theta_h < 0.07 rad$, the angular acceptance of COMPASS spectrometer up to 2004.

The different parton distributions were chosen among the most updated ones at the time [4] was published:

- The unpolarised parton densities of the nucleon come from CTEQ65 [34]. The ones of the photon come from GRV [35].
- The fragmentation functions used were KKP [36], which were known to describe well the π^0 production at PHENIX and STAR [37].
- For the parton helicities, several sets of the GRSV analysis were used to show the effect of ΔG on the asymmetries:
  - the standard GRSV [38] set corresponding to the best fit of the GRSV analysis was used.
  - two extreme sets corresponding to $\Delta g(x, \mu_0^2) = g(x, \mu_0^2)$ and $\Delta g(x, \mu_0^2) = -g(x, \mu_0^2)$ for a reference scale μ_0^2 and then evolved with DGLAP equations.

One shows here some theoretical expectations for this choice of parameters and inputs. All the quantities presented are relative to the reaction $\mu p \to \mu' h X$ for a choice of the parton helicity of a photon $\Delta f_a^\gamma = |f_a^\gamma|$ (in the polarised case) and they are integrated of η_h from 0.44 to 2.4.

In Sec. 1.2.3, we did present all the unpolarised cross-section study done to verify the applicability of this theoretical framework to COMPASS kinematic domain. We now show here the ratio of NLO over LO unpolarised cross-sections Fig. 1.15, and the ratio of unpolarised cross-section for each process separated between quarks and gluons Fig. 1.16. This can be achieved in the calculations by cancelling the parton densities (or helicities for further polarised studies) of the processes not involved in the process. For instance, if one wants to study the partonic

reaction $qg \to cX$, one puts $f_q^N = f_{\bar{q}}^N = 0$ and $f_g^\gamma = 0$.

Fig. 1.15 shows also the ratio of polarised cross-sections expected for NLO over LO. One can see that both polarised and unpolarised ratios rise at $1 < p_T < 2$ GeV/c were COMPASS data are expected to be the most sensitive to ΔG. These NLO calculations are hence essential to understand the measurements of both polarised and unpolarised the cross-sections, as well as the asymmetries.

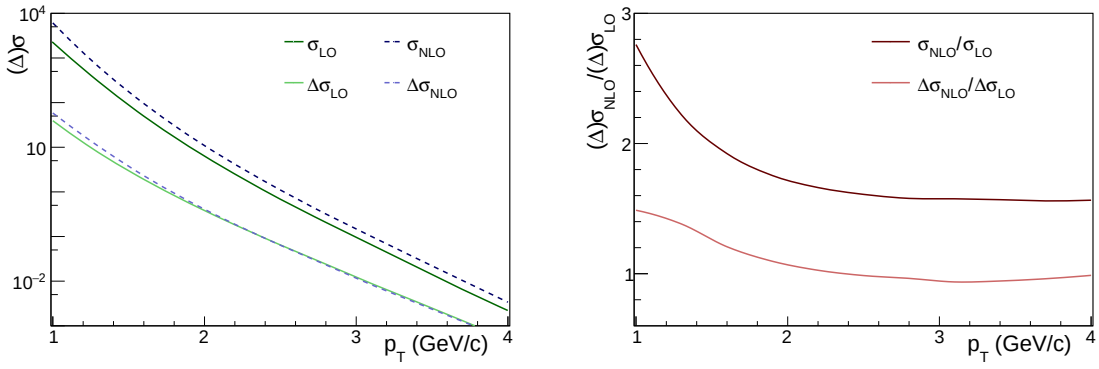

Figure 1.15: $d(\Delta)\sigma_{NLO}$ and $d(\Delta)\sigma_{LO}$ (left) and their ratios $d(\Delta)\sigma_{NLO}/d(\Delta)\sigma_{LO}$ (right)

Fig. 1.16 and Fig. 1.17 show the ratio of polarised cross-sections for the different processes completely separated between gluons and quarks, and separated between direct and resolved processes.

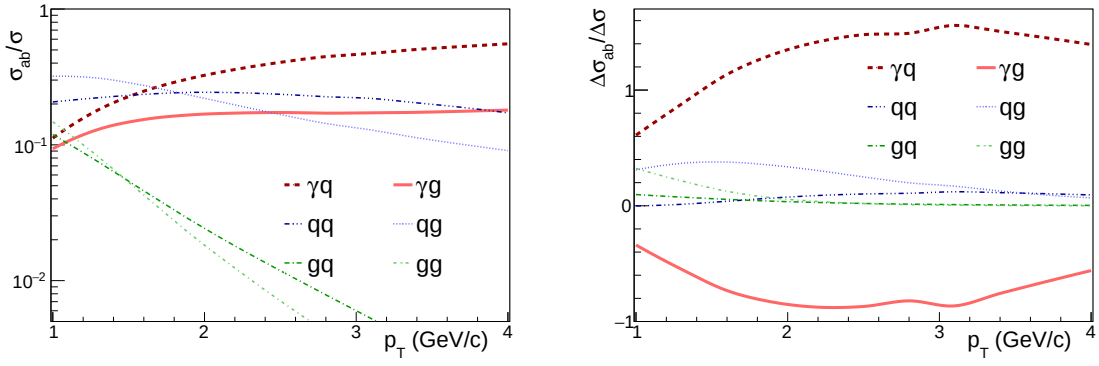

Figure 1.16: $d(\Delta)\sigma_{ab}/d(\Delta)\sigma_{tot}$ at NLO

The results from this study of 2004-2005 [4] show a cancellation between γq (QCD Compton Scattering) and γg (PGF) (Fig. 1.18), which at low p_T is responsible for the rise of the resolved processes cross-section. The direct processes still remain dominant at high p_T.

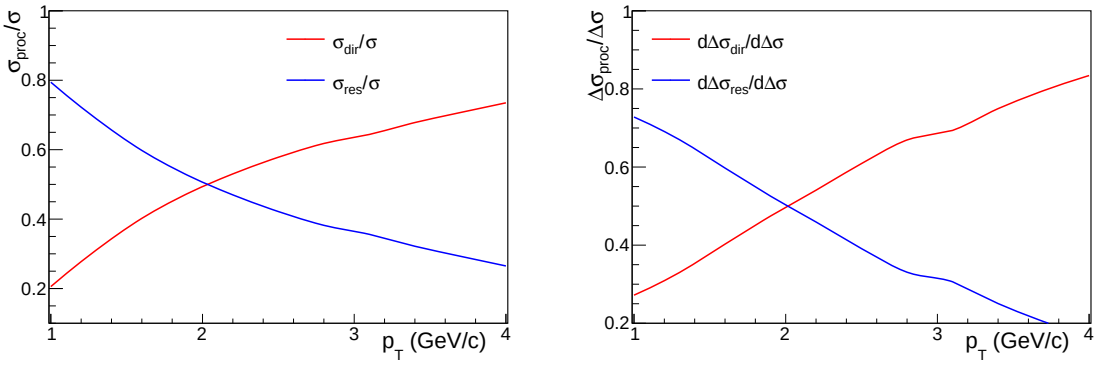

Figure 1.17: $d(\Delta)\sigma_{dir}/d(\Delta)\sigma_{tot}$ and $d(\Delta)\sigma_{res}/d(\Delta)\sigma_{tot}$

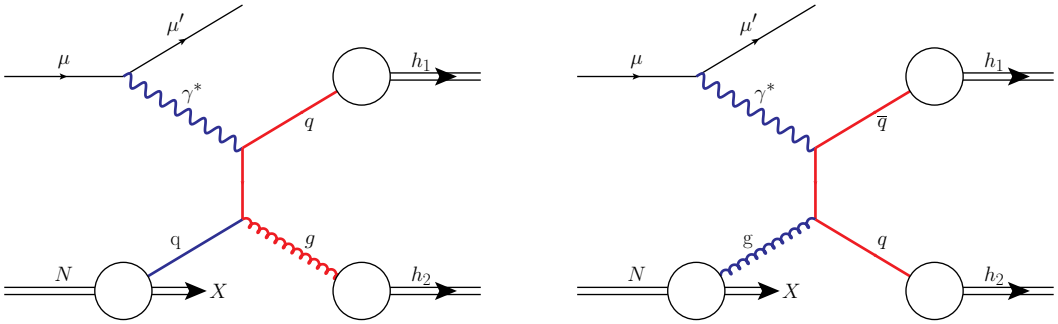

Figure 1.18: LO Feynman diagrams for QCDC and PGF reactions

Finally one can compute the asymmetries for $\mu d \to \mu' hX$ and $\mu p \to \mu' hX$ for the three sets of GRSV polarised PDFs. They are shown in Fig. 1.19 with COMPASS projection of uncertainties for all the statistics taken by the experiment (for a deuteron target and a proton target).

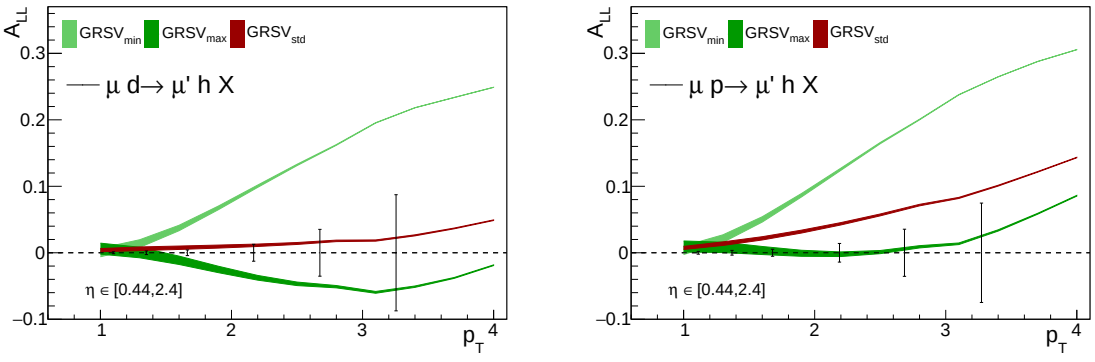

Figure 1.19: Asymmetries for $\mu d \to \mu' hX$ (left) and $\mu p \to \mu' hX$ (right) for the parameter choice and the input distributions of the 2004-2005 study. In black COMPASS projection of uncertainties for all the data taken between 2002 and 2011

It is possible to show (Sec. 5.4) that this single hadron photoproduction asymmetries analysis is sensitive to x_g (the fraction of momentum carried by a gluon of the nucleon) between 0.05 and 0.2 for a hard scale of $< p_T^2 > \approx 5$ GeV^2. At these range, the gluon PDF can be integrated

to get an idea of the different truncated gluon polarisation ΔG^{trunc} ($= \int_{x_{min}}^{x_{max}} \Delta g(x_g) dx_g$) for the different sets of GRSV. These values are summarised in Tab. 1.2.

set	$GRSV_{min}$	$GRSV_{std}$	$GRSV_{max}$
ΔG^{trunc}	-0.62	0.20	0.74

Table 1.2: Values of ΔG^{trunc} for each parameterisation of GRSV for $\mu^2 = 3$ GeV^2 and $x_g \in [0.07, 0.25]$

Comparing the gap between $GRSV_{min}$ and $GRSV_{max}$ asymmetries to the uncertainties expected by COMPASS data, one can get an idea of the sensitivity of this method on ΔG^{trunc}. Estimations of ΔG^{trunc} are performed in Sec. 5.4.

Chapter 2

The COMPASS Experiment

COMPASS (COmmon Muon Proton Apparatus for Structure and Spectroscopy) or NA58 is a fixed target experiment located at CERN in the north area Fig. 2.1. This experiment aims to study two different physics fields: the nucleon spin structure and the hadron spectroscopy. For this purpose the experiment uses both muon and hadron beams.

The first experiment proposal [39, 40] was first accepted in 1998. The main goal for the nucleon structure was then to measure directly the gluon polarisation [3, 20, 21], but it also allowed to provide data for DIS and SIDIS improving the statistical accuracy of quarks and antiquarks polarised distributions [41], or parton fragmentation functions through multiplicity measurements [42].

In a second phase, which started in 2012 [43], it was decided to extend the study to the generalised parton distributions (GPDs) through deeply virtual Compton scattering (DVCS), to the nucleon transverse momentum dependent distributions (TMDs) through Drell-Yan process and also to the chiral perturbation theory through Primakoff reactions [44].

This chapter will describe the experimental setup used with a muon beam for spin structure measurements. From the upstream part to the downstream part of the setup, the polarised muon beam from the SPS, the polarised target, some elements of the spectrometer and also the data acquisition system of COMPASS will be described.

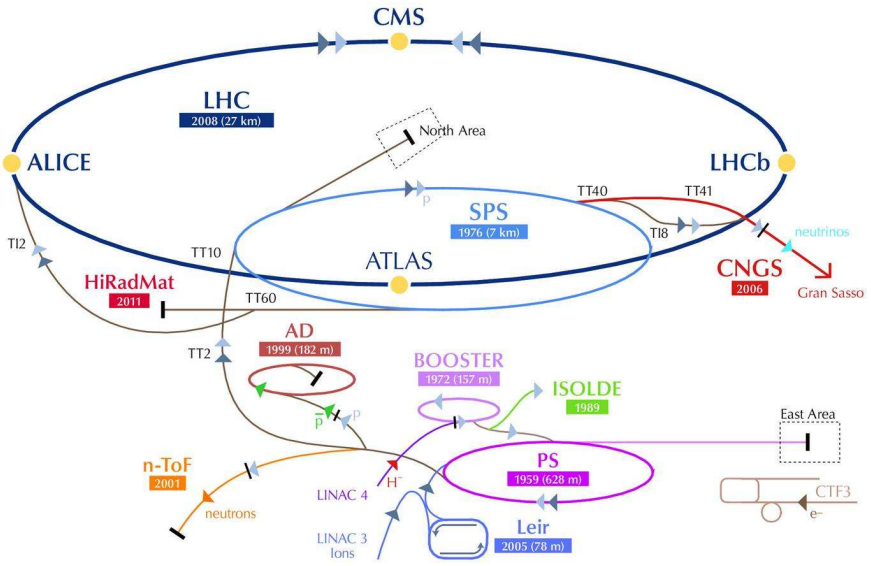

Figure 2.1: CERN web of accelerators and experiments

2.1 The Beam from the SPS

COMPASS receives its beam from the M2 extraction line (Fig. 2.2) of the SPS (Super Proton Synchrotron). The SPS provides a high intensity proton beam ($\sim 10^{13}$ protons for 2002-2007 years (resp. 2011) in 5 s (resp. 10 s) spill for a SPS cycle of 17 s (resp. 40s)) with a momentum of about 400 GeV/c.

This beam collides with a berylium target, whose thickness can vary between 100mm and 500mm depending on the intensity required. This results in a hadron beam, mainly consisting on pions ($\sim 96\%$), the rest being kaons and a few protons.

In order to get a muon beam into the COMPASS hall, these pions are allowed to decay in the 600 m channel of the M2 beamline. During this travel, 5 to 10% of these hadrons decay into muons and neutrinos; the remaining hadrons are stopped at the end of the tunnel by a large Beryllium absorber ($\sim 10\ m$). The muon beam is then steered to the experimental setup through a series of dipoles and magnetic collimators that selects the momentum and through quadrupoles that keep it focused. The muons momentum is also measured with an accuracy of 0.5% for an intensity of 2 to $4 \cdot 10^8$ muons per spill by four hodoscopes and two scintillating fibers stations, which are part of the beam momentum station (BMS) Fig. 2.3. This nominal momentum can be changed: 160 GeV/c for 2002-2007 and 200 GeV/c 2011.

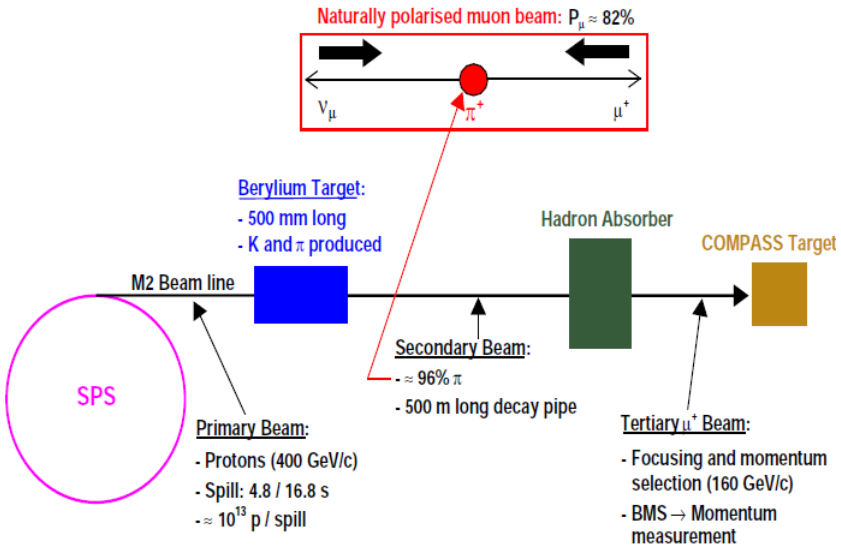

Figure 2.2: Sketch of the M2 beam line with the polarised muon beam production [45]

The parity violation of the weak decay $\pi \to \mu\,\nu$ allows the muon beam to be naturally polarised. In the rest frame of the pion, the muon is 100% polarised, but since the helicity is not Lorentz invariant, this polarisation needs to be calculated for a given momentum through Eq. 2.1. In practice it is estimated with Monte-Carlo simulation of the BMS [46].

$$P_\mu = -\frac{m_{\pi,K}^2 + (1 - 2E_{\pi,K}/E_\mu)m_\mu^2}{m_{\pi,K}^2 - m_\mu^2} \tag{2.1}$$

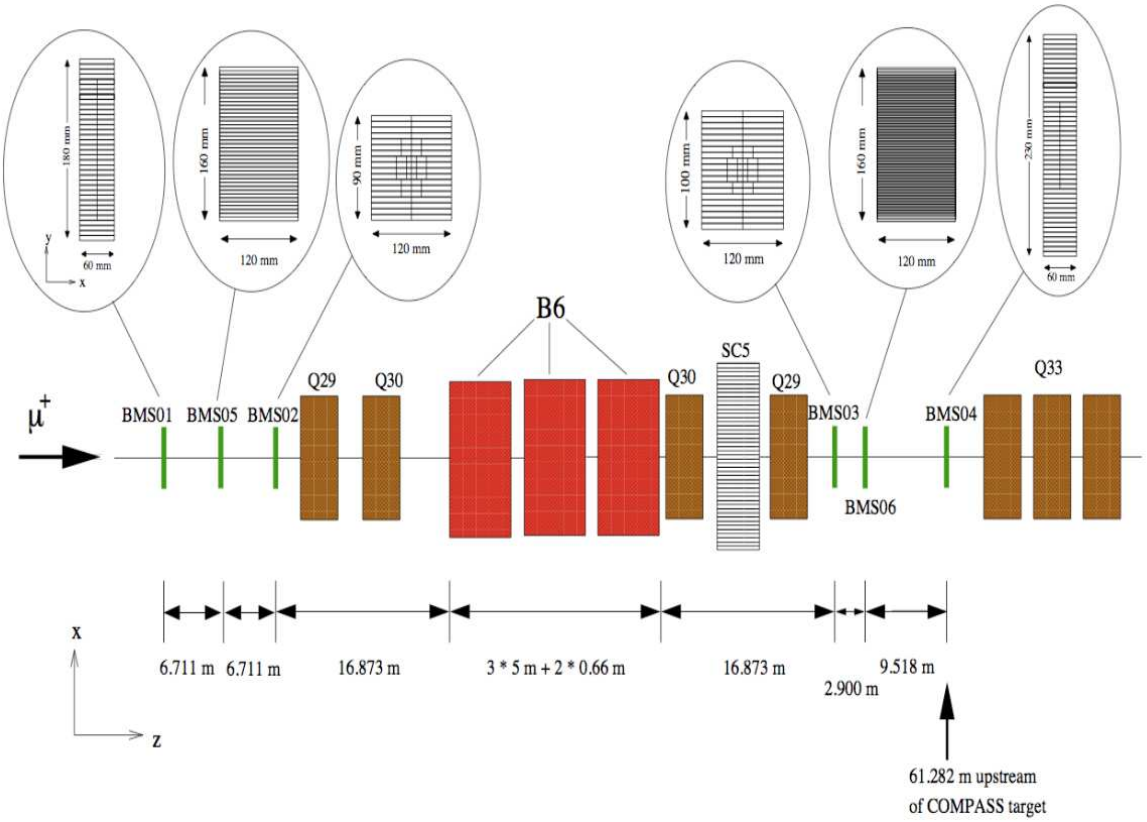

Figure 2.3: Layout of the beam momentum station. The hodoscopes are denoted BM01 to BM04, the scintillating fibre stations BM05 and BM06, the dipoles B6 and the quadrupoles Q29 to Q32

2.2 The Polarised Targets

The polarised muon beam will then interact with a polarised target containing protons or neutrons. From 2002 to 2006, the target contained deuteron lithium (^{6}LiD) and for 2007 and 2011 it contained ammonia crystals (NH_3). The material is first irradiated by an electron beam at low temperature to create paramagnetic centers in the crystal lattice of the material. The unpaired electrons can be polarised through Zeeman effect in a presence of an intense and homogeneous magnetic field of 2.5 T in the direction of the beam, which is provided by a solenoid magnet surrounding the target. At equilibrium the electrons are polarised to 99% using the Curie law for spin 1/2 particles at a few Kelvin Eq. 2.2.

$$P_{1/2} = tanh(\frac{\mu B}{kT}) \tag{2.2}$$

In order to transfer dynamically the polarisation from the electron to the nucleus, the dynamic nuclear polarisation (DNP) technique is used [47, 48]. The electron spin couples to the nucleus hyperfine structure and a polarisation state can be induced by microwave radiations Fig. 2.4. At equilibrium, only B and D states are equally populated. By applying a microwave radiation with a frequency $\omega_e + \omega_p$ ($\omega_e - \omega_p$), a transition from the B(D) state to the C(A) state is induced. After $\sim$ 1 ms the electron spin relaxes and can then be used to polarise other nuclei. The nucleus time of relaxation is much longer (1 min) so the material remains in a polarised state. By operating in a "frozen spin mode", the time of relaxation of the system can be several months. This state is achieved by lowering the temperature to 55-95 mK thanks to a ^{3}He-^{4}He refrigerator system (Fig. 2.5 and Fig. 2.6).

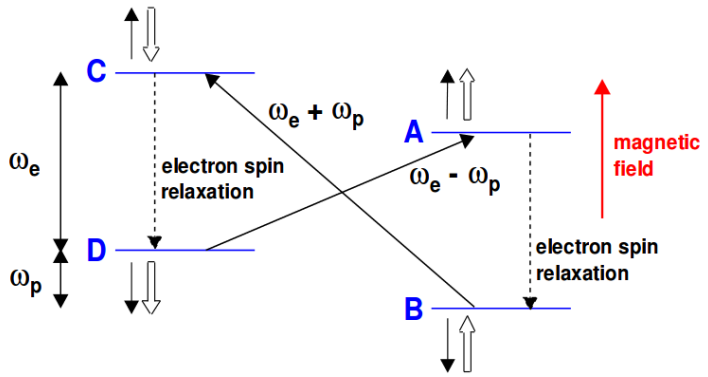

Figure 2.4: The four energy levels defined by the sin projections of an electron-nucleus system (electron spin with a single arrow and nucleon spin with a wide arrow)

Thanks to this technique, one can polarise two consecutive target cells with opposite polarisations using microwave radiations with the two different frequency $\omega_e + \omega_p$ and $\omega_e - \omega_p$, knowing that the cells are separated by a microwave stopper. This ensures to have roughly the same luminosity for the two different spin states.

The target polarisation can be measured using Nuclear Magnetic Resonance (NMR) [49] by means of 10 coils made of cupronickel (CuNi) alloy located around the target cells.

For the longitudinal polarisation runs, COMPASS have used two different polarised target:

- From 2002 to 2004 COMPASS used a two cylindrical cells target Fig. 2.5. Each cell was 60 cm long and had a radius of 3 cm. The solenoid vessel had an angular aperture of ∼70 mrad.

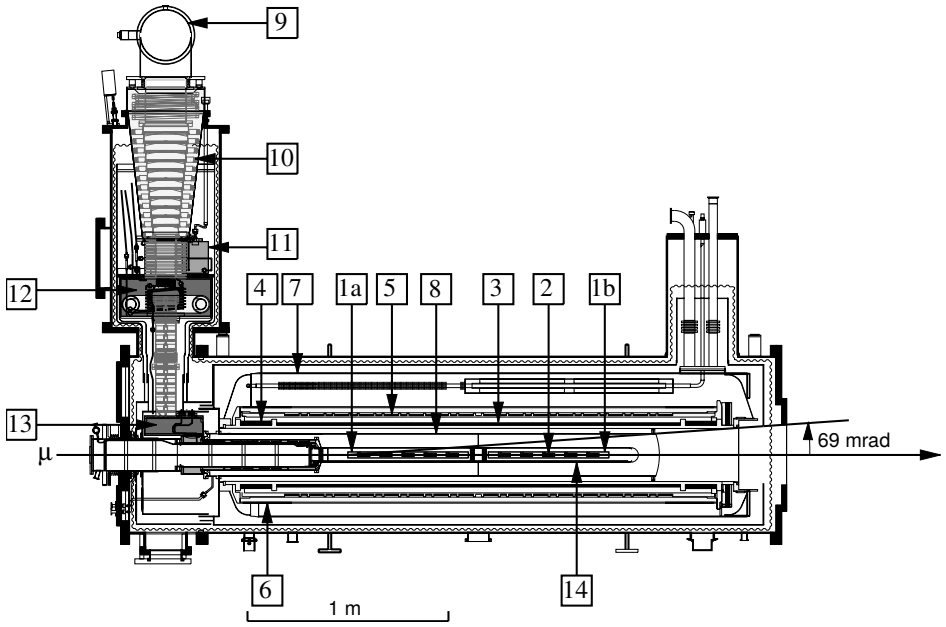

Figure 2.5: COMPASS polarised target from 2002 to 2004

- For 2006, 2007 and 2011 COMPASS used a three cylindrical target Fig. 2.6. The cell were 30 cm (upstream), 60 cm (central) and 30 cm (downstream) long and had a radius of 4 cm. The upstream and downstream cells had the same polarisation, while the central one had an opposite polarisation. The solenoid vessel had an angular aperture of ∼180 mrad.

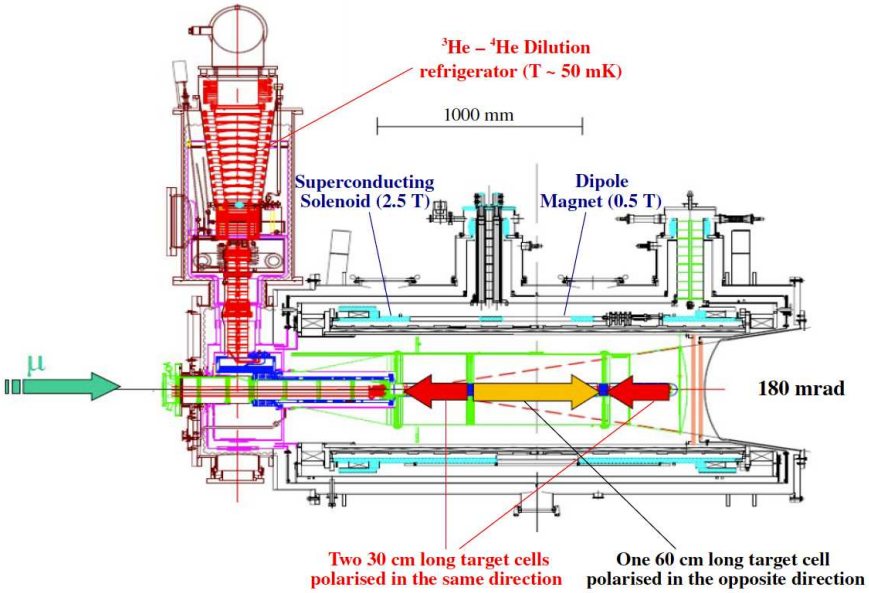

Figure 2.6: COMPASS polarised target for 2006-2007 and 2011

The accuracy of this polarisation measurement is of the order of 5%. For the ^{6}LiD target, the polarisation was around 40-50%, whereas for the NH_3 target, it could reach 90%.

2.3 The Spectrometer

The COMPASS spectrometer is composed of two stages represented in Fig. 2.7 which stretches on 50 m:

- The first stage, named Large Angle Spectrometer (LAS), dedicates to low energy particles detection emitted at large angles. This stage starts by some tracking detectors detailed later and a first dipole magnet (SM1) creating a magnetic field perpendicular to the beam [50]. The aperture of this magnet is of 180 mrad (same as the largest aperture of the targets).

- The second stage, named Small Angle Spectrometer (SAS), is used for particles with a momenta larger than 5 GeV/c. and with an angle lower than 30 mrad. This stage starts by the dipole magnet SM2 creating also a magnetic field perpendicular to the beam.

These two stages are equipped with different types of detectors with different functions:

- tracking detectors.

- identification detectors/calorimeter detectors.

- trigger detectors.

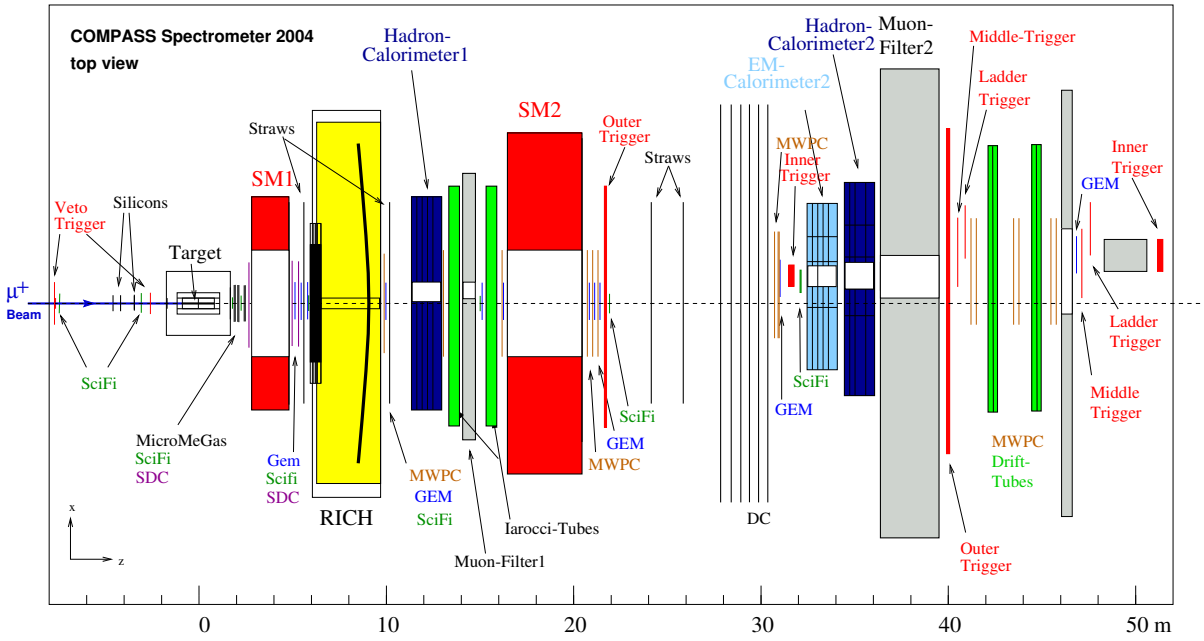

Figure 2.7: Skectch of the top view of COMPASS setup

2.3.1 Tracking Detectors

These are used coupled with the dipole magnets to measure the momentum and the angle of the charged particles (for this, one needs detectors before and after the dipole magnet). The Lorentz force curves the trajectory of a charged particle in a magnetic field. In the simple case where the magnetic field $\vec{B}$ is perpendicular to the trajectory, for a particle of momentum p and charge q, one gets:

$$\frac{p}{q} = 0.3BR \tag{2.3}$$

And on the case of small angle deviation:

$$\frac{p}{q} = \frac{0.3 \int Bdl}{\theta} \tag{2.4}$$

, where the magnetic field is integrated on the length of the dipole.

Different technologies are used in the different angular acceptances regions (which are linked with different luminosity and different needs of accuracy):

Very Small Area Trackers (VSAT)

The detectors of this region have to sustain a maximal flux of $5 \cdot 10^7$ Hz/cm^2. This region is covered by the 9 stations of scintillating fibres detectors (SIFI) and 6 silicon microstrips detectors ($3\,stations \times 2$). They are mainly used to track the beam particles like the incoming muons and the tracks are reconstructed using the information of the BMS.

- The SCIFI [51] are placed along the beam axis in the LAS and in the SAS with an active area from 4×4 cm^2 to 12×12 cm^2. Each station consists of 2 orthogonal planes and sometime a plane oriented at 45°. These detectors have an excellent time resolution of ∼500 ps and a spatial resolution of 0.1-0.2 mm.

- The silicon microstrips detectors [52] have an active area of 5×7 cm^2 and are placed before the target. Each detector measures 2 projections of the trajectory, and for one

plane the other detector is inclined of 5° to get two more projections. These detectors have a time resolution of 2.5 ns and a spatial resolution of 10 μm.

Small Area Trackers (SAT)

The detectors of this region have to sustain a maximal flux of $3 \cdot 10^5$ Hz/cm^2. This region goes from a few centimeters to a few dozen of centimeters around the beam. It is made up of two kinds of microstrips gaseous detectors: the GEM (Gas Electron Multiplier) [53] and Micromegas (MICRO MEsh GAseous Structure) [54]. These detectors have a really good efficiency ($> 95\%$) and spatial and time resolution (< 100 μm and ≈ 10 ns).

- There are 3 stations of Micromegas consisting of 4 detectors each (horizontal, vertical and $\pm 45°$) located in the LAS between the target and SM1. Their active area is 40×40 cm^2 with a dead zone in the center with a diameter of 5 cm. These detectors will be further detailed in the next chapter Chap. 3 with an upgrade whose one of its goal is to fill this dead zone.
- The GEM detectors are located after SM1 in the SAS, there are 11 stations of 2 detectors with an active area of 30×30 cm^2. Each detector consists of two orthogonal planes, and among a station, one of the detector is oriented at 45°. Each plane is made of 3 stages of GEM foils which are 50 μm thick and drilled with holes of 70 μm diameter. Each side of the foil is submitted to a different potential to create a strong electric field in the holes. Primary electrons are created in the drift gap and multiplied in each GEM foil when passing a hole which ensures the amplification and the collection of ions (Fig. 2.8).

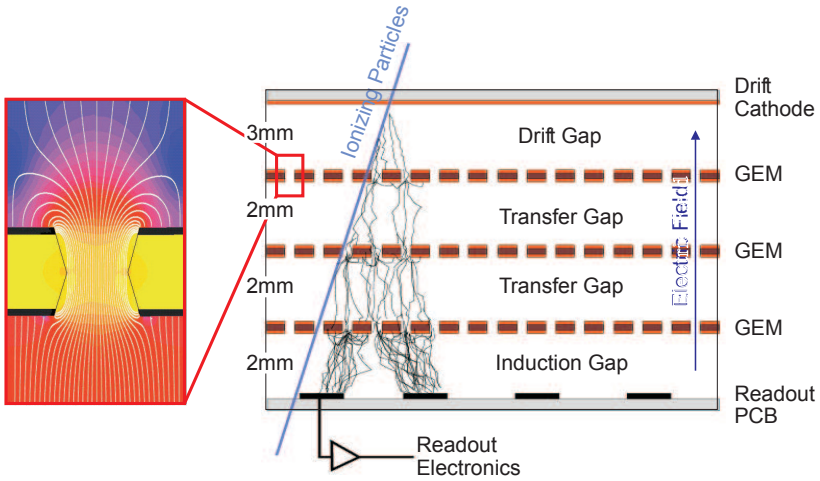

Figure 2.8: Schematic side view of a triple GEM detector. The inset shows the electric field configuration in the vicinity of a hole

Large Area Tracking (LAT)

The detectors of this region have to sustain a maximal flux of $10^4 Hz/cm^2$. This region is covered by 3 drifts chambers [55], 9 straw tube chambers and 14 multiwire proportional chambers (MWPC) [56].

- The drift chambers are large gaseous volumes comprised between two cathodes made of Mylar coated with graphite between which is placed alternately a potential wire of 100 μm diameter and a readout wire of 20 μm diameter. A cascade of electrons is created when an ionising particle crosses a drift cell and is collected by the readout wires (Fig. 2.9). Each

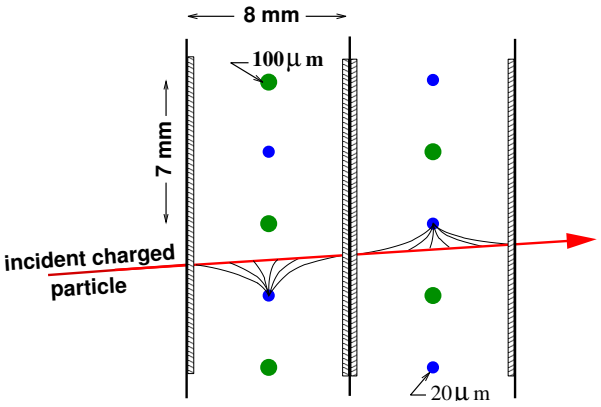

Figure 2.9: Drift cell geometry of the drift chambers as delimited by the two cathode foils and the two potential wires

station of the drift chambers is equipped with eight detection planes in four orientations (horizontal, vertical, ±20° for the small DCs and ±10° for the large DCs). Two of them are located before the SM1 magnetic dipole with an active area of 180 × 127 cm^2. The third one is located after SM1 with a larger active area of 240 × 104 cm^2. All these chambers have an inactive central area of 30 cm diameter which can be switched on for alignment purposes.

- The straw tube chambers are also gaseous detectors similar in principle to the drift chambers. They are made up of aluminum cathode tubes of 6mm diameter enclosing an anode wire of 30 μm diameter made of gold-plated tungsten. Each detector consists of two layers of tubes which measures one component. They have an active area of 323 × 280 cm^2 and are located between the two dipoles SM1 and SM2.

- The MWPC are used for large radial distance tracking in the SAS. They have an active area of 178 × 120 cm^2 and an inactive central one of 16 cm to 22 cm diameter. They consists of 2 to 4 planes with different orientations. They are located before and after the SM2 magnetic dipole.

Along with the information on the beam particles, the tracking detectors provide a vertex longitudinal position resolution of 0.2 cm and a vertex transversal position resolution of 1 μm.

2.3.2 Particle Identification Detectors

Depending on the nature of the considered particle, one can use several techniques of identifications. In the COMPASS spectrometers there are 2 electromagnetic calorimeters [57] to detect photons or electrons, 2 hadronic calorimeters to distinguish hadrons from muons [58], 2 muon filters to identify the muons and a RICH detector (Ring Imaging CHerenkov) [59] which allows to distinguish between the different types of hadrons. This last detector will be detailed in Sec. 2.4.

- **The electromagnetic calorimeters**: these detectors are located after each magnetic dipole. They are used to measure the energy of electrons, positrons and high energy photons. When a photon interacts with one of these calorimeters, it triggers a electromagnetic shower. The electrons and positrons cross lead glass cells emitting Cherenkov radiations, whose energy is proportional to the one detected in the photomultipliers.

- **The hadronic calorimeters**: Each stage of the spectrometer is equipped with a hadronic calorimeter located after the electromagnetic calorimeter. They are used to measure the hadrons energy. They are made of an alternation of iron plates and scintillating strips. When a hadron crosses them, it produces a hadronic shower which delivers a signal proportional to its energy. Whereas for a minimum ionizing particle as the muon, the signal is much lower.

- **The muon filters**: they are located after each calorimeter set, made up of one iron absorber of 60cm wide for the LAS or one concrete absorber of 2,4m wide for the SAS, enclosed in two stations of low resolution tracking detectors. Only the muons can go through the absorber, so that a matching signal in the two stations signs the passage if a muon.

2.3.3 Trigger System

The COMPASS trigger system is used for selecting the interesting events among all tracks in a very short time (<500 ns) [60]. The trigger system then collects the data of all the detectors through the data acquisition system which is detailed in Sec. 2.6 and provide the reference time of the event. For this purpose, it uses signals from some hodoscopes (scintillators with photomultipliers), the energy measured in the hadronic calorimeters, and a veto system (Fig. 2.10). The veto system consists of three scintillating counters located 10m, 8m and 3m before the target with central holes of 10 cm, 4 cm and 4 cm in diameter. These counters are used to reject tracks from the halo of the beam.

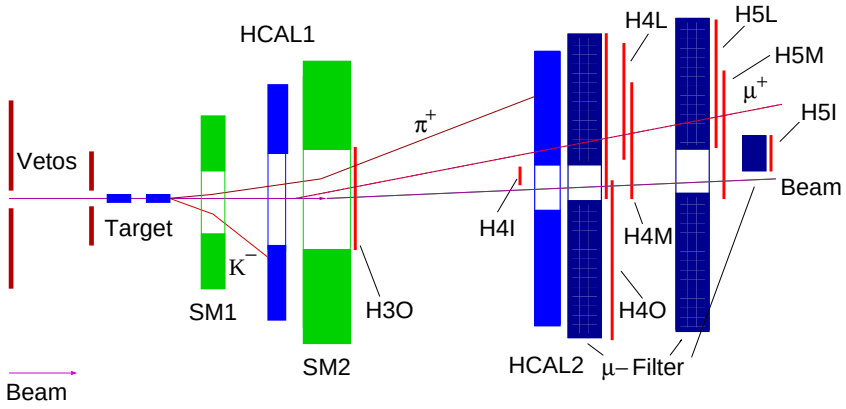

Figure 2.10: Schematic view of the trigger system. The most upstream veto and the H1G and H2G hodoscopes are not shown

The trigger system is used differently for different type of events or different kinematic domains (Fig. 2.11). For the muon program, there are six main triggers:

- The Outer Trigger (OT) is a purely inclusive trigger for recording high-Q^2 events. Therefore it uses only the hits in the hodoscopes H3O or H4O.

- The Calorimeter trigger (CT) is a purely calorimetric trigger, it does not analyse the scattered muons, but just requires a large energy deposit of more than ∼20 GeV in one HCAL.

- The inclusive Middle Trigger (incMT) is also a purely inclusive trigger for recording inclusive muon-scattering. It uses only the hits in the hodoscopes H4M and H5M to select the events at an average Q^2.

- The Middle Trigger (MT) is the semi-inclusive analog of incMT. It requires an energy deposit in one of the HCALs.
- The Ladder Trigger (LT) is a semi-inclusive trigger for recording low-Q^2 events. It uses the hodoscopes H4L and H5L and requires an energy deposit in one of the HCALs.
- The Inner Trigger (IT) is a semi-inclusive trigger for recording low-Q^2 events with a lower Q^2- and y-range. It requires hits in H4I and H5I, and also requires energy deposits in one of HCALs.

For the analysis treated in Chap. 4, all triggers which could have low-Q^2 events, i.e. events in the quasi-real photoproduction regime, have been used to maximise the statistics: CT, MT, incMT, LT and IT. Of course the most important ones are the LT and IT:

$$IT = (H4I \wedge H5I)_{0.1<y<0.6} \wedge (HCAL1 \vee HCAL2) \quad (2.5)$$

$$LT = (H4L \wedge H5L)_{0.5<y<0.9} \wedge (HCAL1 \vee HCAL2) \quad (2.6)$$

In the photoproduction regime, one encounters several background processes: elastic scattering of muons off electrons in the target at a fixed value of $x_{Bj} = m_e/m_N$ or the radiative tail of the elastic scattering off target nucleons. But these background processes are suppressed by semi-inclusive triggers by requiring the energy deposit in one of the HCALs or in the case of inclusive triggers by a selection on high-p_T hadrons.

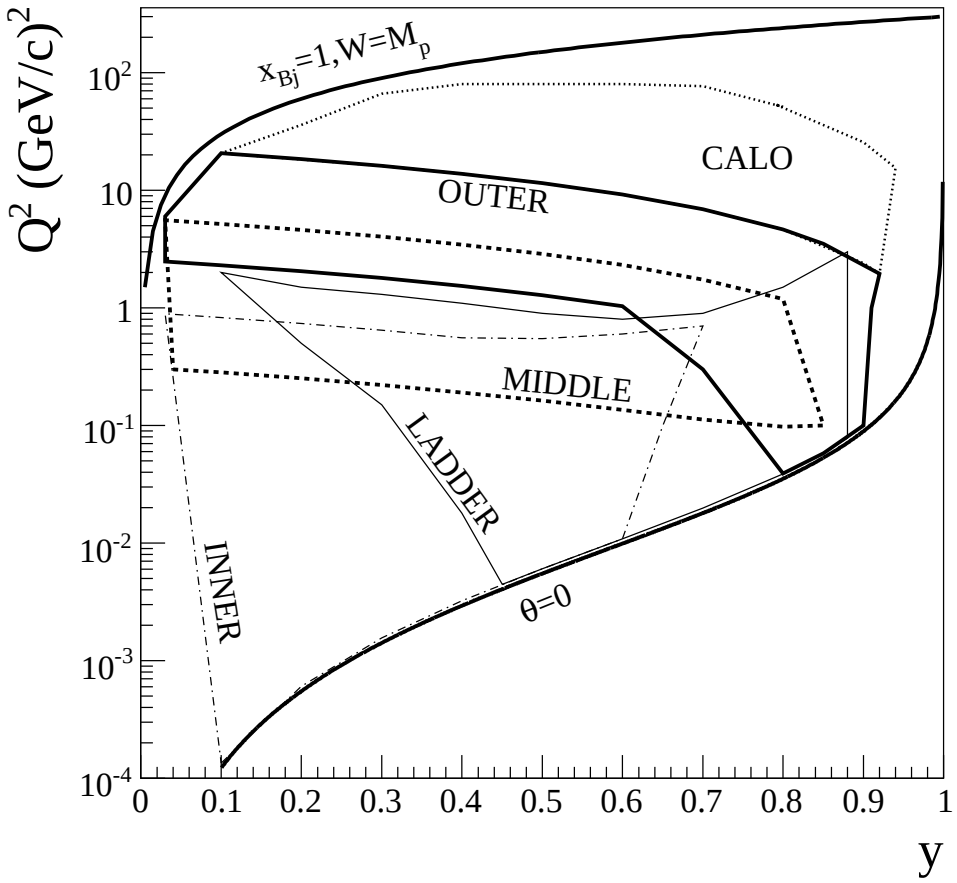

Figure 2.11: $y - Q^2$ coverage of the trigger subsystems for a 160 GeV muon beam. The two lines, ($x_{Bj} = 1$, $W = M_p$) and ($\theta = 0$) show the kinematic limits of elastic scattering and forward scattering, respectively

2.4 The Particle Identification with the RICH Detector

This section will treat in detail the RICH detector, which is used for the identification of the hadrons in pions, kaons, protons or other. The information from this detector will be used in Sec. 4.5 for the analysis of the asymmetries for identified final state hadrons.

2.4.1 Cherenkov Effect

The RICH detector system is based on the Cherenkov effect: when a charged particle goes through a transparent medium with a speed v greater than the speed of light ($v_{light} = c/n$, with n the medium refractive index), a radiation called Cherenkov radiation is produced by the medium.

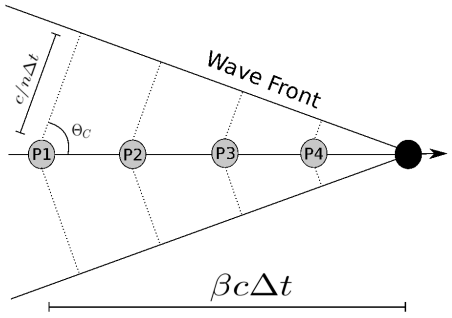

Figure 2.12: Cherenkov radiation schematic geometry

A particle of mass m_h with a momentum p_h produces a Cherenkov radiation at a particular angle Θ_C with respect to the particle track. The coherence between waves (emitted between A and B) is achieved when the particle traverses AB at the same time as the radiation travels from A to C. Thanks to this, one can define the Cherenkov angle Θ_C:

$$cos\,\Theta_C = \frac{c/n\Delta t}{\beta c\Delta t} = \frac{1}{n\beta} \tag{2.7}$$

, where β is the particle velocity. This leads to some properties of this radiation:

- Threshold limit: if $\beta < 1/n$, no Cherenkov radiation can be emitted.
- Maximum emission angle: $cos\,\Theta_C = 1/n$, it is reached for ultra-relativistic particles.

Θ_C can be obtained from the radius of the reconstructed photon ring image in the detection plane. From this measurement and knowing the momentum p_h with the spectrometer reconstruction, one can extract the mass m_h which allows us to identify the particle:

$$m_h = p_h\sqrt{n^2 cos^2\,\Theta_C - 1} \tag{2.8}$$

2.4.2 The COMPASS RICH Detector

The RICH is a large size detector ($\sim 3 \times 5 \times 6\text{m}^3$) filled with a gaseous radiator. In the downstream part, two spherical sets of mirrors reflect the photons into an array of photon detector (placed in the upstream part) placed outside of the spectrometer acceptance.

The gaseous radiator is C_4F_10, it has a refractive index n of 1.0015 and a low chromaticity ($dn/dE \approx 5 \cdot 10^{-5}$ eV^{-1}), which allows a particle identification in a wide momentum range

(from 2 to 60 GeV/c). There can be some imperfection due to contamination by water vapor or oxygen, or stratification of the gas causing a gradient of the refractive index, that's why the gas is constantly circulating, filtered and reshuffled at a pressure of 1 mbar above the atmospheric pressure. To avoid a huge amount of photons that could be created by the muon beam interacting with the heavy RICH gas, a 10 cm diameter pipe filled with helium surrounds the vessel around the beam path.

The two spherical mirrors consist actually of 58 smaller mirror with different shapes with a reflectance of 80% in the UV region. They cover an total area of 21m^2. The mirror system is placed at 1.6 m above and below the beam axis and its radius of curvature is 6.6 m. Some imperfections on this radius slightly blur the image (more for larger angles particles) and this affects the resolution of the detection.

The photon detection system and the read-out have been upgraded in 2006. From 2002 to 2004, it was consisting of eight identical MWPCs for a total active surface of 5.4 m^2, equipped with UV sensitive CsI photocathodes segmented in pads of 8×8 mm^2. Unfortunately this system was dead time limited in COMPASS environment, reducing then the efficiency for particles scattered at small angles. Since then it consists of two symmetric parts (below and above the beam) composed of 8 modules (Fig. 2.13): in the external region it is still MWPCs with CsI photocathodes and the central area is now composed of fast MultiAnode PhotoMultipliers Tubes (MAPMT) coupled to individual telescopes of fused silica lenses. This last region detects photons in a lower wavelength range. The read-out system has also been adapted for this particular region.

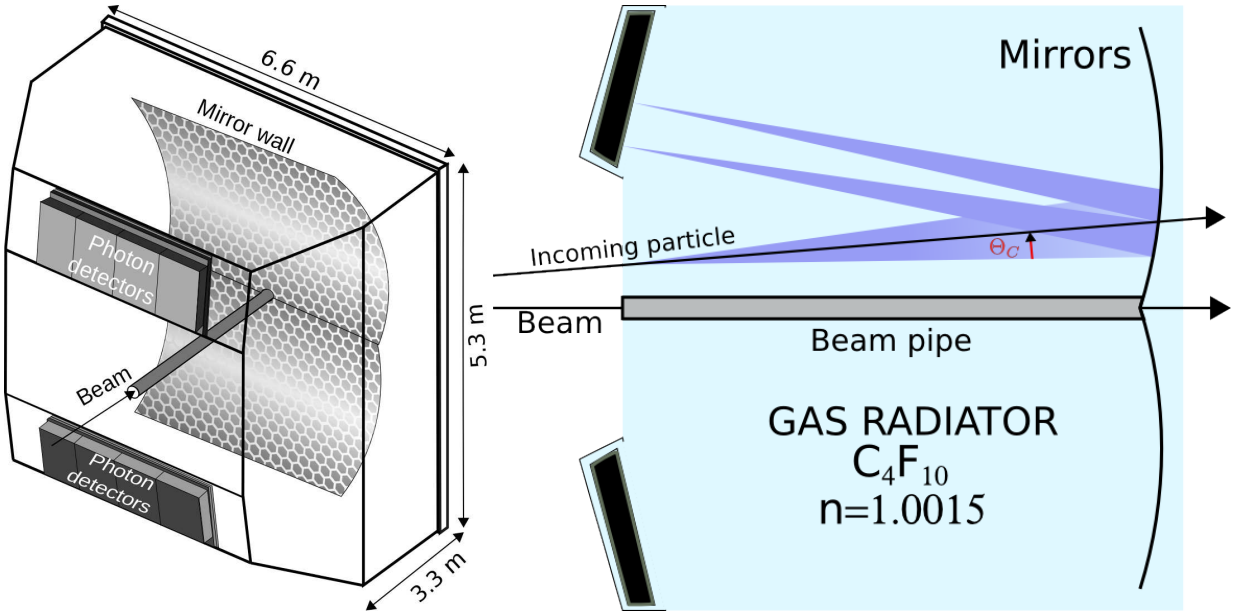

Figure 2.13: Schematics of RICH detector. The left figure shows a side cut with the angle of the particles and radiation

2.4.3 RICH Event Reconstruction and Mass Separation

The reconstruction of RICH events is part of the full reconstruction by CORAL Fig. 2.16 and it is managed by RICHONE, a package contained in CORAL. This reconstruction is divided in several stages:

- Since the photon detectors are composed of several parts, the first step is the clustering of the measurement (the pad with the maximum pulse strength is identified and then

regrouped with the adjacent ones with a signal). This allows to determine the weighted center of the cluster. The time information comes from MAPMT hits that don't need clustering.

- The next step is to reconstruct the photon rings and determine the Cherenkov angle. For this, the trajectory of each Cherenkov photon is calculated with respect to the plane containing the particle track and its reflection in the mirror. All the photons are expected to have the same Θ_C and to be uniformely distributed in ϕ (the angle between the photon trajectory and X on the XY plane), whereas the photons emitted from other particles or background have a flat Θ_C distribution. The emitted photons with the same (Θ_C, ϕ) are reflected on the same point of the focal surface, therefore it shows a ring image on the detector plane.

The Θ_C measurement allows us to determine the mass m_h of the particle, but as shown in Fig. 2.14 it is sometimes difficult to separate the different particles in some momentum domain: the bands corresponding to kaons and protons are only visible from $p_h \approx 9.45$ GeV/c and $p_h \approx 17.95$ GeV/c respectively; and at high momentum ($p_h > 40$ GeV/c), the Cherenkov angle reaches an asymptote and pions are not distinguishable from kaons.

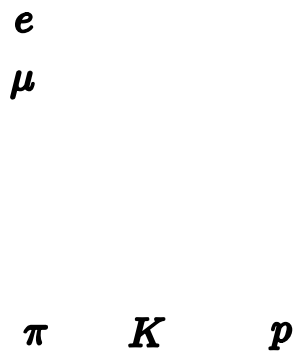

Figure 2.14: Measured Cherenkov angle Θ_C as a function of p_h for 2006 data

2.5 Data Acquisition System

The goal of the acquisition system is to collect the data coming from detectors and to save them. The main constraint at COMPASS is the high frequency of the triggers going from 10kHz to 100kHz. The electronic front-end cards of each detector preamplify the signals. These signals are then digitised by TDC (Time-toDigital Converter) or ADC (Analog-toDigital Converter) modules, which are located close or in the detectors. These digital signals are then sent to the CATCH and GeSiCA modules which gather the data from several TDC or ADC sometime representing several thousands of detection channels. These modules are directly connected to the Trigger Control System (TCS) which transmit the trigger signals to the TDC and ADC modules and then to the front-end cards.

The modules CATCH [61] and GeSiCA [57] then transmit the data through an optical link (S-LINK) [62] to computers called Read-Out Buffers (ROB), whose role is to temporarily store these data, to let the time to other computers called Event Builders (EB) (connected by Gigabit ethernet links) to reconstruct the full events. These EB copy then the data on a local hard drive before sending them to the CERN central data recording system where they are saved on magnetic tapes. The data collected amounts up to 1 Pb for each year of data taking.

The data acquisition system is managed by the DATE software [63], which was originally developed for the ALICE experiment. It allows to manage the trigger configuration and to supervise the errors and numbers of ROB and EB needed. All this system allows a great flexibility to add detectors, to change front-end cards or to change the triggers.

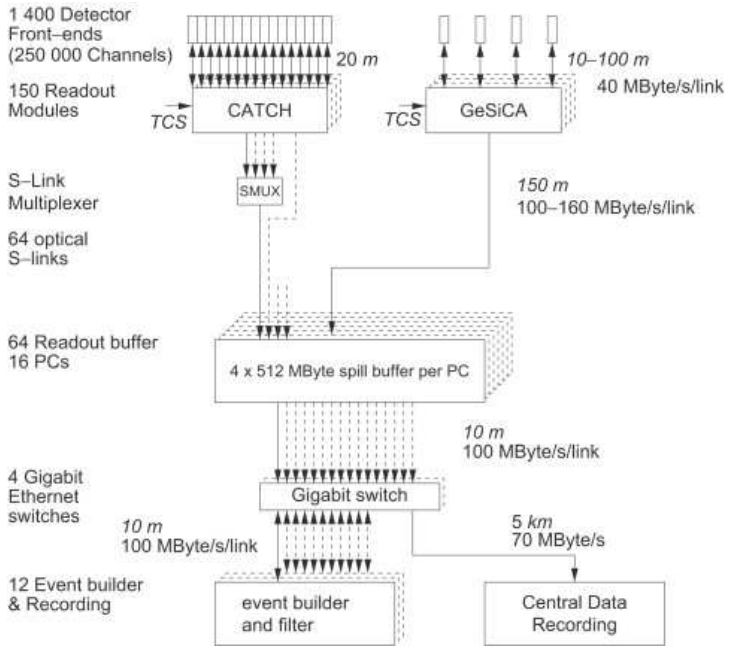

Figure 2.15: General structure of the DAQ system. It mainly consists on three stages: digital signals collection, the readout modules, partial events storage, the readout buffer PCs, and event records, the event builder [64]

2.6 Data Reconstruction and Analysis

The raw events saved by the data acquisition system do not contain any physical information on the detected particles but only raw data from the detectors like the amplitude of signals measured for the passage of a particle. In order to get interesting data, one needs to add some information on the detectors like their position in the spectrometer, the position of the channels in the detectors, or the magnetic field maps. All this information is gathered by the CORAL (COMPASS Recontruction Algorithm Library) software, which will reconstruct the event and bring the information about:

- parameters of the particles trajectory.
- parameter of vertices.
- identification of the particles.
- energy deposit in the calorimeters.

The complete steps of the event reconstruction by CORAL is summarised in Fig. 2.16. One will briefly describe the steps to reconstruct the tracks and the vertices.

To reconstruct the tracks in the spectrometer (after the target) CORAL needs three inputs to compute the track reconstruction:

- The link between an electronic channel and a physical channel which is given in a mapping file particular to every detector.

- The position of the detector in the spectrometer which is given in a geometry file particular to every period of data taking. This file is made before the period during an alignment run, which allows to update the position of every detector.
- The position of the physical channel on the detector, which is written in CORAL code. This information allows also to do a clustering: regrouping physically adjacent channels, to improve determining the coordinates and the time of the particle passage.

CORAL then try to find favourable combinations of clusters in every region of the spectrometer. The regions are defined in a way that the tracks are straight lines inside the regions, which excludes the zones close to the magnets and the zone with too much material. These clusters are then linked to form a track and a final adjustment is performed to take into account the material crossed by the track. One can then extract the information about the position and momentum for one reference z_0. To get information in another z requires then the magnetic field map of the spectrometer.

For the tracks of incoming particles, CORAL uses the measurements of the BMS, which already gives the information on the position and momentum.

The extrapolation of the incoming tracks and the ones reconstructed in the spectrometer gives a first estimation of the position of the vertex. It is then adjusted by getting rid of the tracks too far from the vertex. One extract then the information of position and momentum at the vertex point by taking into account the distribution of material inside the target.

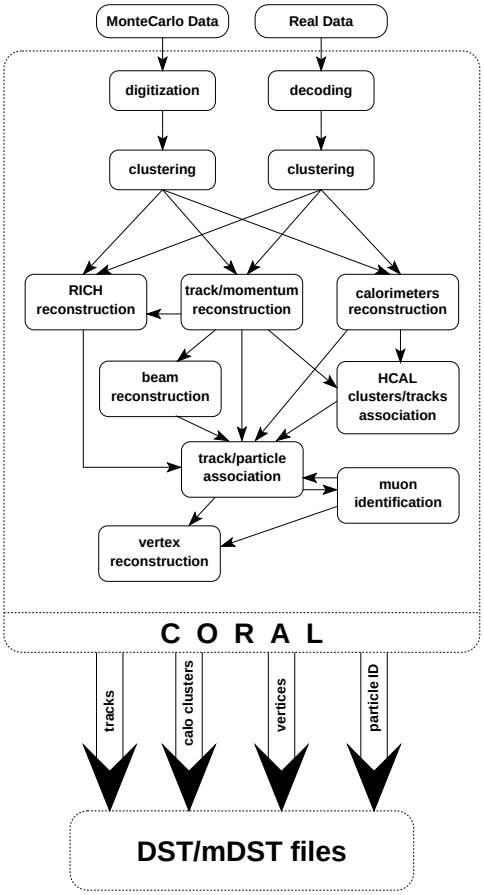

Figure 2.16: Schematics summarising the reconstruction of events by CORAL [65]

All the reconstructed information given by CORAL is stored in the form of Data Summary Tape (DST). These files are the processed by PHAST (PHysics Analysis Software Tools) soft-

ware, which allows to extract and calculate the kinematic variable desired for a given analysis. It also allows to save the data in ROOT objects like TH (histogramms) or TTree (trees) which are more convenient for a further analysis [66].

Chapter 3

Micromegas Detectors Study

Gaseous detectors use the ionisation of gas by charged particles to detect their passage. The invention of the wire counter in the early twentieth century have allowed to put into practice this principle. From then on, the detectors have evolved to gaseous detectors with microstructures, to which the Micromegas detectors belong.

In this chapter, we will review this evolution to explain the composition of the Micromegas and we will then detail these detectors and the improvements achieved. Finally, we will describe a study of the characterisation of new Micromegas.

3.1 Principles of Gaseous Detector

3.1.1 Wire Chambers

The first wire counters have been build in 1908 by Rutherford and Geiger to detect alpha particles [67]. Nowadays they are still used in Geiger counter to evaluate the radiation level [68].

This devices consists in a metallic tube filled with a certain gas, crossed by an electrical wire at potential $+V$ with respect to the tube (Fig. 3.1). It creates an electric field (Eq. 3.1):

$$\vec{E} = \frac{V}{rln\frac{b}{a}}\vec{e_r} \tag{3.1}$$

, where a and b are the radius of the exterior of the wire and the interior of the tube, and $\vec{e_r}$ is the vector unit in the radial direction.

The passage of a charged particle ionises the atoms of the gas and if the field amplitude is high enough, the electron are guided to the wire and the ions to the tube. The displacement of the electrons and ions close to the wire induces a measurable electric current.

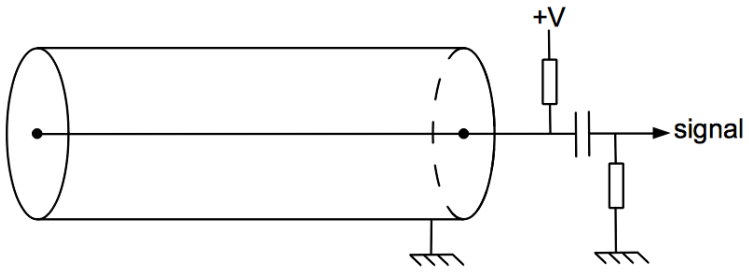

Figure 3.1: Schematic figure of a wire counter

Depending on the amplitude of the field, several cases are possible:

- The amplitude is high enough and all the charges are collected, which induces a weak signal only efficient to measure fluxes but not to detect single particles.
- The amplitude is higher than a certain value and the electrons have also enough energy to ionise the atoms of the gas, creating a shower of electrons. This phenomenon happens closer to the wire since the amplitude is higher (Eq. 3.1). The signal induced is then stronger by a factor G called the gain of the detector, the latter being then called a proportional detector. In this case the detector can detect single particles.
- For even higher amplitudes, there are multiple showers on the passage of the charged particle and the signal is not proportional to the energy deposit of the particle. This is the case of the Geiger-Müller counters.

3.1.2 MultiWire Proportional Chambers

The MultiWire Proportional Chamber or MWPC is the next step to detect a particle and track its position [69]. The principle of detection is the same but one has now a succession of cathodic wires which are able to provide the position of the particle passage. The gas is located in a volume crossed by a succession anode wires delimited by two anodic planes. Each anode wire is linked to an electronic channel which amplifies the signal received and allows to distinguish between the different wires to transmit the information about one coordinate of the point of passage of the particle Fig. 3.2). To get the other projections, one needs several detectors with different orientations.

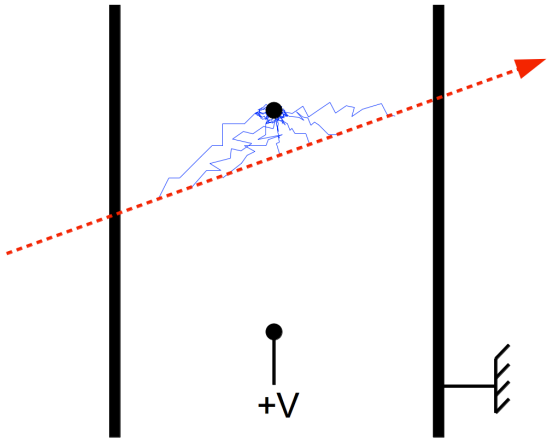

Figure 3.2: Schema representing the principle of a MWPC

The spatial resolution of the detector is limited by the distance between the wires [70]. This has been improved by a factor 5 in the drift chambers [71], by measuring the time between the passage of the particle and the signal generated. To have a constant drift velocity, the electric field is made uniform thanks to electric wires placed between the anodes and cathodes, as shown in Fig. 2.9.

These detectors are used in most particle physics experiments but they are limited by the flux which can not exceed 10 kHz/mm [70]. This is due to the slowness of the ions to go to the cathode. They are mainly created close to the anode and then create a field that can screen the field of the wire. At high flux the ions have not the time to go far enough and still screen the anode wire.

3.1.3 Micro Pattern Gas Detectors (MPGD)

The Micro Pattern Gas Detectors (MPGD) are the last generation of gaseous detectors. The innovation rests on one hand on the replacement of the wires by strips or pixels of copper engraved in a support (like in a printed circuit board), which solves the problem of electrostatic repulsion between the anode wires limiting the spatial resolution. On another hand the primary ionisation stage and the amplification stage are separated so that the space of the amplification can be reduced to catch the ions in a limited time. The dead time of the anode is then reduced and it allows the detector to work with higher fluxes.

Nowadays the main types of MPGD used in the particle physics experiment are the GEMs (Gas Electron Multiplier) [72] and the Micromegas (MICRO-Mesh Gaseous Structure) [73] which are described in the next section (Sec. 3.2.1).

The GEM are composed of a kapton foil of 50 μm thick covered by a layer of copper on each side with holes of 70 μm diameter, separated by 140 μm. The application of a 200-300 V voltage between the copper foils is enough to trigger showers of electrons in the holes. The ions are quickly caught on the cathode side (only partially but they are in every case not seen by the readout strips). The principle of the GEM is illustrated in Fig. 3.3.

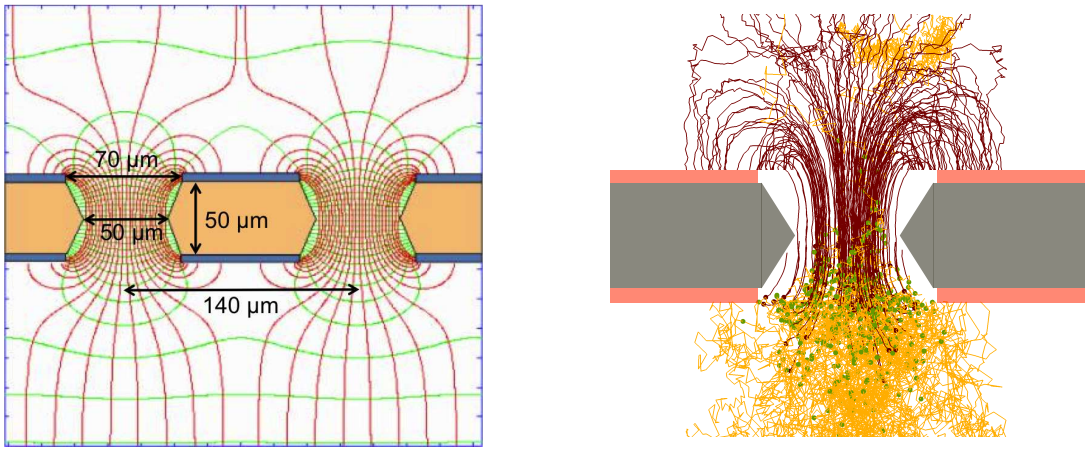

Figure 3.3: Principle of the GEM foil. On the left: electrostatic field configuration, on the right: simulation of a shower in a hole (ions in red and electrons in yellow

3.2 The Micromegas

3.2.1 Description

Micromegas detectors have been developed since 1996 and upgraded for the use of COMPASS experiment since 2001. The gaseous volume is comprised between a drift cathode and readout anode strips. This volume is separated in two by a micro-grid, also called mesh:

- A conversion space between the drift cathode and the micro-grid, measuring 3 to 5 mm with a voltage of ∼500 V.
- An amplification space between the micro-grid and the readout strips, measuring 100 μm with a voltage of ∼500 V.

The principle of the Micromegas is illustrated in Fig. 3.4. The voltage in the conversion space is high enough to avoid the recombination of ions and electrons produced by the ionisation

but low enough to avoid electron avalanches in this space. The amplification by avalanches happens in the amplification space where the ions are quickly caught by the micro-grid and the electrons are guided to the readout strips.

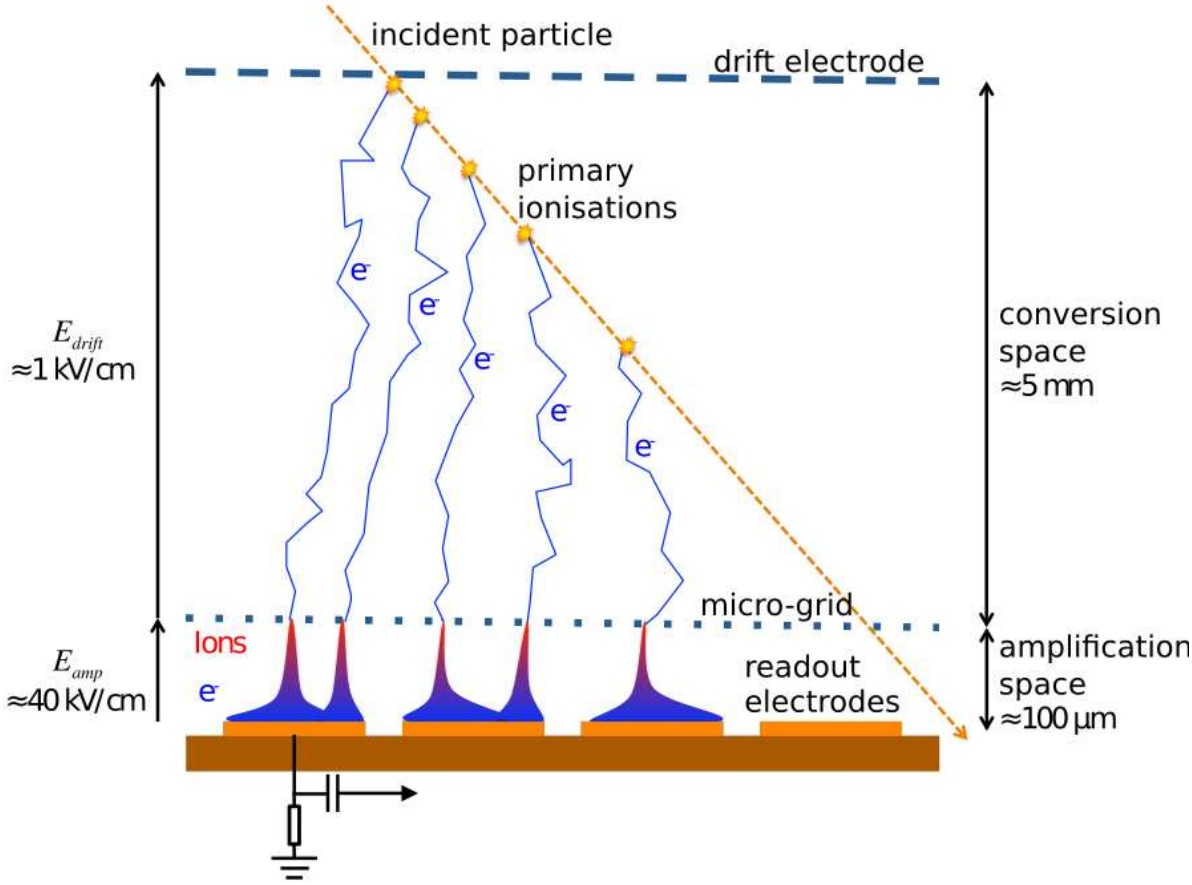

Figure 3.4: Principle of Micromegas functioning

3.2.2 Detailed Functioning

Most of the following information apply not only to Micromegas but also to MPGD and are inspired by [70].

The gas used for the ionisation is composed of a noble gas (He, Ar, Ne or Xe) and an organic gas, the quencher (CF_4, CO_2, CH_4, C_2H_6 or C_4H_{10}). The passage of a particle can directly cause the ionisation, or only excite an atom which then ionise another atom of the same quencher molecule by Penning effect. The number of electron/ion pairs created $\langle N_T \rangle$ is about 2 to 10 times larger than the number of primary ionisations and is proportional to the length of gas crossed L:

$$\langle N_T \rangle = \frac{dE/dx \times L}{w_i} \tag{3.2}$$

, where dE/dx is the energy deposit of the incident particle per centimeter and w_i the average energy to create an electron/ion pair.

If the amplitude of the drift electric field is high enough, the electrons move to the micro-grid

and the ions to the drift electrode with an average velocity $\langle v \rangle$:

$$\langle v \rangle = \mu E \tag{3.3}$$

, where μ is the mobility and depends on the particle (ion or electron) and on the property of the gas (pressure and energy). For the ions, which are close to the thermal equilibrium, the mobility does not depend on the field intensity:

$$\mu = \frac{eD}{kT} \tag{3.4}$$

, where k, T, and e are the Boltzmann constant, the temperature and the elementary charge. D is the diffusion factor which depends on the gas properties and is inversely proportional to the elastic cross section between the ion and an atom of the gas.

For the electrons, it is almost three times larger, but since they are not on thermal equilibrium, the increase of the diffusion factor imply a deterioration of the spatial resolution. This can be solved using gases like CF_4 which compensate the increase of the diffusion factor thanks to a larger elastic collision cross section.

Most of the electrons go through the micro-grid into the amplification space since $E_{amp}/E_{drift} \gg 1$. The electric field is there intense enough to favour the avalanches. These avalanches have the shape of a drop with a head of electrons and a tail of ions (Fig. 3.5). The number of incident electrons can be expressed by:

$$dn = n\alpha_T dx \tag{3.5}$$

, where α_T is the first coefficient of Townsend, which represents the number of ionisation by length unit, it depends on the pressure and on the electrostatic field. By integrating on the avalanche path, one can extract the gain of the detector:

$$G = \frac{n}{n_0} = e^{\alpha_T L_{amp}} \tag{3.6}$$

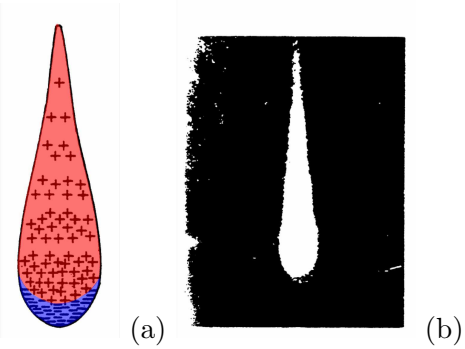

(a) (b)

Figure 3.5: (a) Model of an avalanche showing the distribution of the different charge carriers. The electrons in blue and the ions in red. (b) Photo in a cloud chamber showing the shape of the avalanche [72]

The signal is created in the readout strips by the movement of the charge carrier between the micro-grid and the strips. The electrons, which are mostly created close to the readout strips, have a really short distance to reach and give a short and intense signal. The ions, which have a lower mobility, take 100 ns to reach the micro-grid, which remain a short time

and allow the detector to work at fluxes up to the GHz/mm^2 without much loss of efficiency [74].

If the charge density in the amplification space exceeds the limit of Raether [75], a plasma is created between the micro-grid and the readout strips. It results in a short circuit which reduces the difference of potential between the micro-grid and the strips. These discharges can damage the electronics. They are caused by the passage of high ionising particles (electron δ, α particles or hadrons), a too high intensity of the beam, or by a too high difference of potential in the amplification space.

3.2.3 Characteristics and Limitations at COMPASS

At COMPASS, twelve Micromegas detectors are in the LAS region (Sec. 2.3). They contribute to the tracking at small angles, together with the GEM detectors. The detectors of this region are exposed to a high flux of low energy electromagnetic showers not screened by SM1 (up to 300 kHz/cm^2) and also to the influence of the fringe field of SM1.

The detectors have an active area of 40×40 cm^2 with an inactive central area of 5 cm diameter. The conversion space measures 5 mm and the amplification one 100 μm. The drift electrode and the micro-grid are in copper to render the detector structure insensitive to the magnetic field. The readout strips consist of 1024 200 μm thick strips made of copper with a 360 μm gap for the strips in the center of the detector and with a 420 μm gap for the ones on the sides. The strips are glued to a 58x114 cm^2 board.

The gas is a mix of 80% of Ne, 10% of C_2H_6 and 10% of CF_4 for a muon beam [76]. It allows a good compromise between spatial and time resolution [77]. The efficiency reaches 96 to 98%. The time resolution is of 9 ns and the spatial one is of 90 μm. The probability of discharge per muon is $5 \cdot 10^{-11}$ at high fluxes. For a hadron beam, the discharge rate raises, therefore the voltage of the micro-grid is decreased to lower the gain and the CF_4 percentage is reduced to lower the number of primary ionisations. Due to these changes, the time and spatial resolutions worsen.

In spite of the good performances of these detectors, there remains some limitations and some place for improvement. First the existing detectors have a central inactive area of 5cm diameter, which can not be activated without a big loss of efficiency, because the beam flux would create a too high occupation of the electronics [74]. Concerning the hadron beams, the detectors can not work for higher intensities. Finally, the detectors show some ageing and some zones become blind due to a detachment of the grid.

3.3 The New Pixelised Micromegas

3.3.1 Motivations for Improved Micromegas Detectors

In order to make up for the limitations of the detectors described in the previous section, it has been decided to install new Micromegas detectors for the second phase of COMPASS. The DVCS program needs measurements at low Q^2, meaning at very small angles with better spatial resolution than the scintillating fibers (150 μm), and with less material reducing the probability of interaction of the real photons. To achieve this goal, the new detectors must have an active central area.

One will now describe the different solutions considered for the new Micromegas detectors.

Activation of the central area with pixels

The solution to limit the flux by electronic channel in the central area is to use pixels instead of strips. The flux can reach 20 MHz/cm^2 in this region, meaning 500 kHz by strip (if strips are used), knowing that the electronics can only take care of 200 kHz. The first prototypes used 32x32 square pixels of 1 mm^2 [45], but a study showed that the spatial resolution was degraded due to a not thin enough segmentation. It was then decided to use rectangular pixels with the same width than the strips (400 μm) and with variable length depending on the proximity to the center as shown in Fig. 3.6.

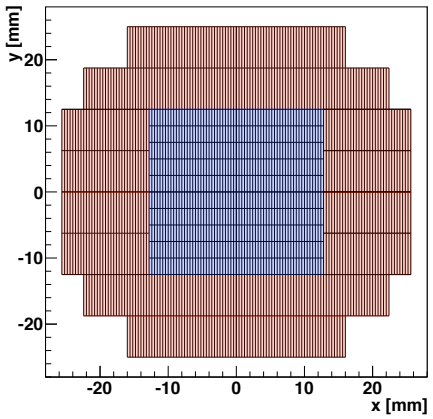

Figure 3.6: Geometry of the pixelised region of the new Micromegas detectors. The blue region consists of 400 μm×2.5 mm pixels and the red region consists of 400 μm×6.25 mm pixels

Decrease of the discharge rate/probability

To reduce the discharge rate, two solutions were envisaged: adding a GEM foil in the conversion space or using a new resistive technology for the readout strips.

Adding a GEM foil (Sec. 2.3) in the conversion space allows to create a preamplification space between the GEM and the micro-grid with a gain of 10-20, reducing a little the voltage between the micro-grid and the readout strips. More importantly it allows to the electronic clouds to transversely scatter which reduce the density in the amplification space.

The resistive technology consists of the addition of a resistive layer under the readout strips, which reduces the amplitude of the discharge from hundreds of volts to less than one volt [78]: during a discharge the potential of the resistive substrate increases until it reaches the potential of the micro-grid, which cuts off the discharge. Unfortunately these technologies are not compatible yet with the pixels of the central area, therefore it is not retained for the new project.

Electronics and support

The signals generated on the strips in the new detectors are read out by APV25-S1 chips developed for CMS [79] (this chips can read 128 channels, it is composed of an amplifier and an analogic memory). They are coupled with ADC cards to digitise the signal. These cards are shown in Fig. 3.7. The ADC card can extract 3 samples for each channel every 75 ns from the APV chips, which allows to study the time of passage of the particle. A study to calibrate this

timing is presented in Sec. 3.4.1.

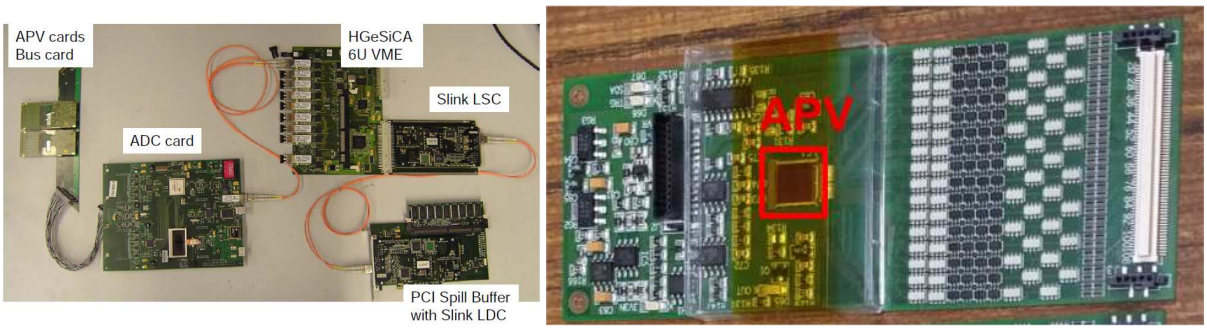

Figure 3.7: Acquisition cards for the pixel Micromegas

To solve the problems of detachment of the grids, a new technique of manufacturing was established: the "bulk" technology [80]. This process allows to industrially produce micro mesh directly fixed to the support board.

3.3.2 Description of the new Pixel Micromegas

We summarise here the composition of the pixel Micromegas which are studied in the next section.

The detectors have an active area of 40×40 cm^2. The central area is composed of 1280 pixels (400 μm×2.5 mm or 400 μm×6.25 mm). The rest of the detector consists of 1280 strips:

- a central region of 15 cm wide with 768 strips of 20 cm long. Each strip is 400 μm wide. This region is divided in two hemispheres.
- two lateral bands with 512 strips of 480 μm wide and 40 cm long.

The configuration is illustrated in Fig. 3.8.

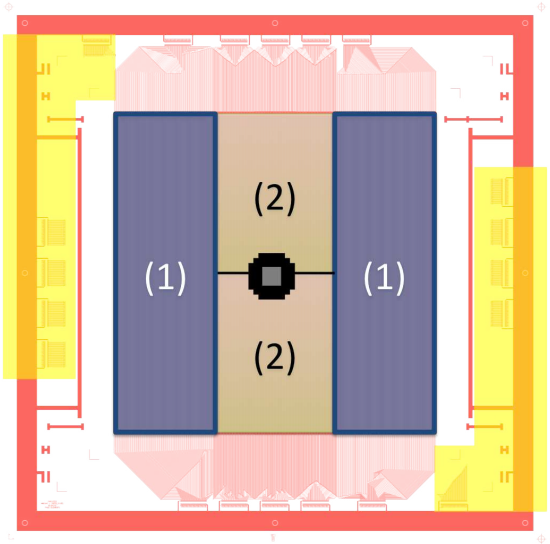

Figure 3.8: Geometry of the pixel Micromegas. (1) strips of 40cm×480μm, (2) strips of 20cm×400μm

The pixels are connected to the electronics via link strips in the verso of the printed circuit board of 200 μm thick. The amplification space between the readout strips and the micro-grid is 128 μm thick, resulting from the "bulk" process.

The new detectors use the hybrid technology Micromegas + GEM, whose principle is illustrated in Fig. 3.9. The GEM foil is located at 2 mm to the micro-grid, it is divided in 16 independent areas separated by an 100 μm inactive area. These areas are connected to the high voltage by 1 MΩ resistor. This segmentation allows to limit the charge during a discharge between the two copper foils. The copper foils are 5 μm thick.

The drift electrode, composed of 5 μm copper foil with holes, is located at 5 mm of the GEM foil.

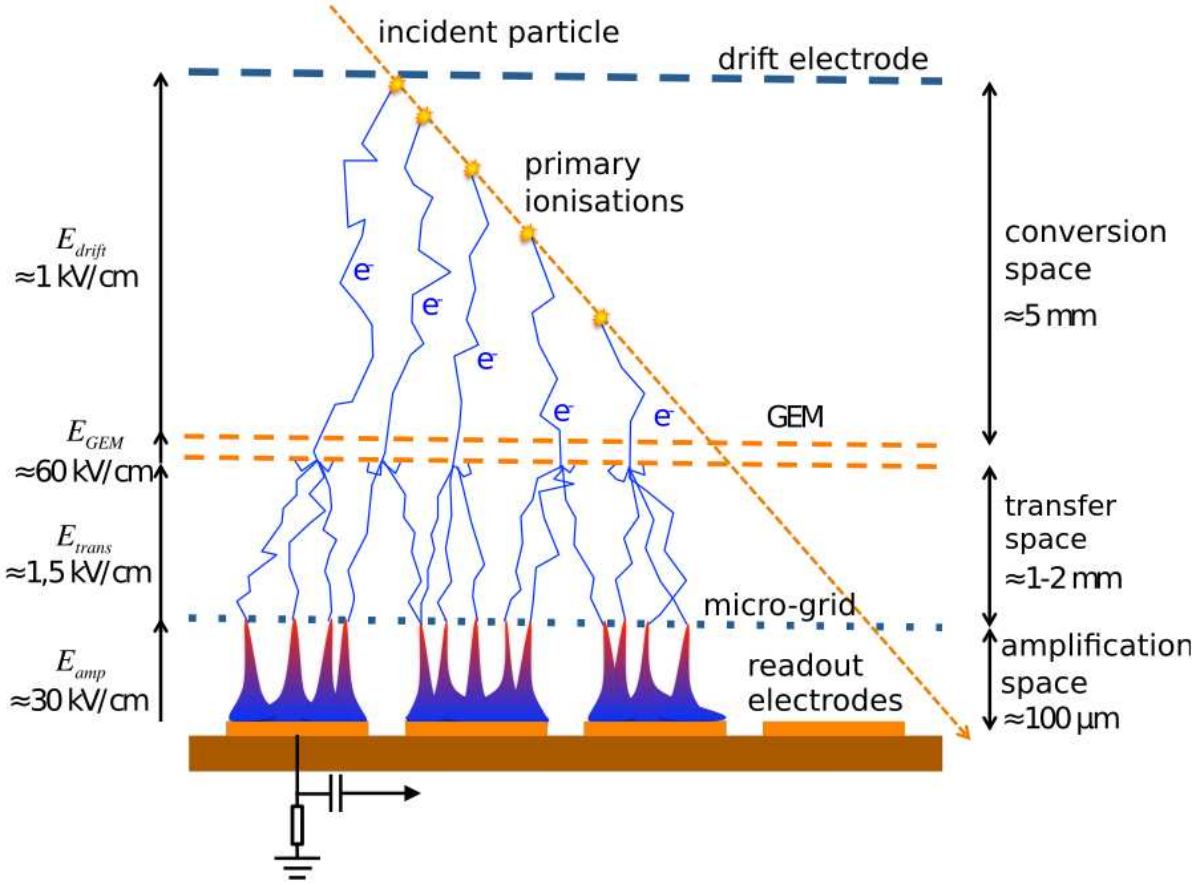

Figure 3.9: Functioning principle of the Micromegas + GEM

Measurements of the gain have been performed depending on the different potentials. They show exponential curves as a function of the GEM potential (V_{GEM}) or of the micro-grid potential (V_{MESH}). Compared to the former detectors, these hybrid detectors reach gains 2.5 times greater (8000 $\rightarrow$ 20000) for reasonable voltages.

For the year 2014, only 4 planes of hybrid Micromegas were installed in the most upstream station in the COMPASS spectrometer. As for all Micromegas stations, it is composed of 4 planes: X (horizontal coordinate), Y (vertical coordinate), U and V ($\pm$45°).

In the following studies, the pixel part of the detector X is called MP01MX and the strip part is called MP01X1. The same nomenclature is used for the other planes U, V and Y.

3.4 Calibration and Efficiency Study

A study of the performances of the new hybrid Micromegas used in 2014 in the first station has been performed. For this study, 4 runs with different beams (hadron or muon) and different intensities were used.

Before studying the efficiency and the spatial resolution of the detectors, the detectors need some calibrations to remove some noise and to synchronise the different chipsets.

3.4.1 Calibrations

Pedestal calibrations

The first calibration aims to remove the noise of electronics. For this the amplitude of the signal (pedestal) and the amplitude of its variations (σ) are extracted from the data without beam for each channel of the detector, and loaded in a database. Then the ADC cards corrects or suppresses any data taken: the pedestal is removed from the amplitude measured and a correction of the common mode is applied to remove all the variations of amplitude shared by all the channels, and finally only the signals with more than a threshold of amplitude are kept. A threshlod of 6σ was chosen after study on the prototypes showing the appearance of false clusters below the threshold of 3.5σ, as shown in Fig. 3.10.

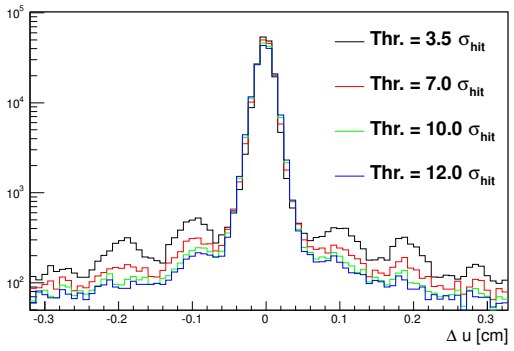

Figure 3.10: Residual distribution Δu for different thresholds (for the strip part of the 2011 prototype)

This calibration is performed for every detector and for every period of data taking, i.e. every time that the detectors are changed or moved, or that the electronics is changed.

APV timing synchronisation

As it was previously seen in Sec. 3.3.1, three amplitude samples can be taken off the APV card signal, 75 ns apart (this period is chosen to match the duration of the signal of the hybrid pixel Micromegas). These samples a_0, a_1 and a_2 are taken off during the rising edge of the signal (Fig. 3.11).

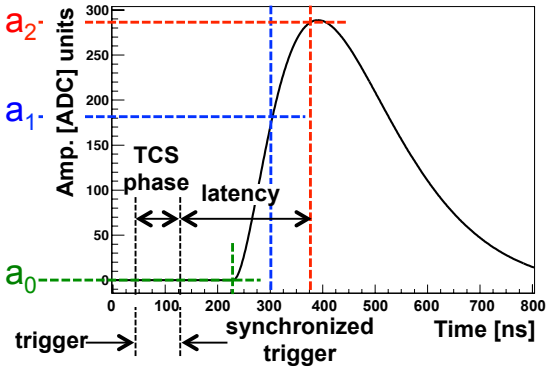

Figure 3.11: APV signal after amplification. The three samples a_0, a_1 and a_2 are taken off during the rising edge of the signal. The TCS phase is the duration between a physical trigger and the time of the next rising edge of the 38.88 MHz clock of the trigger control system. The latency is the duration between the rising edge of the TCS clock and a_2

The clusters are reconstructed with the amplitudes samples of every hits of all the channels of the detectors. The hits are regrouped by cluster and then the position of the cluster is calculated using a center of gravity method weighted with the a_2 amplitude. The main hit is the closest one to this center of gravity.

The cluster time is reconstructed using the ratio $\frac{a_1}{a_2}$ and the TCS phase Δt_{TCS} (duration between a physical trigger and the time between the next rising edge of the 38.88 MHz clock of the trigger control system) of the main hit of the cluster. The observation of $\frac{a_1}{a_2}$ as a function of Δt_{TCS} for all the main hits of an APV card shows a affine relation:

$$\langle \frac{a_1}{a_2} \rangle = \alpha(\Delta t_{TCS}) + \beta \tag{3.7}$$

, where α and β are free parameters of the time calibration for an APV card. These parameters are found using a method of gaussian fitting by slice. Once they are calculated, they are written in files for each APV cards and are communicated to CORAL for the reconstruction of the tracks. The time of each hit can then be determined with:

$$t_{hit} = \frac{\frac{a_1}{a_2} - \beta}{\alpha} - \Delta t_{TCS} \tag{3.8}$$

Fig. 3.12 and Fig. 3.13 shows the raw relation between $\frac{a_1}{a_2}$ with Δt_{TCS} and then the corrected one. The study shows that the parameters are different for all the APV card due to their physical position on the detector. This calibration synchronise then all the APV card of the detector.

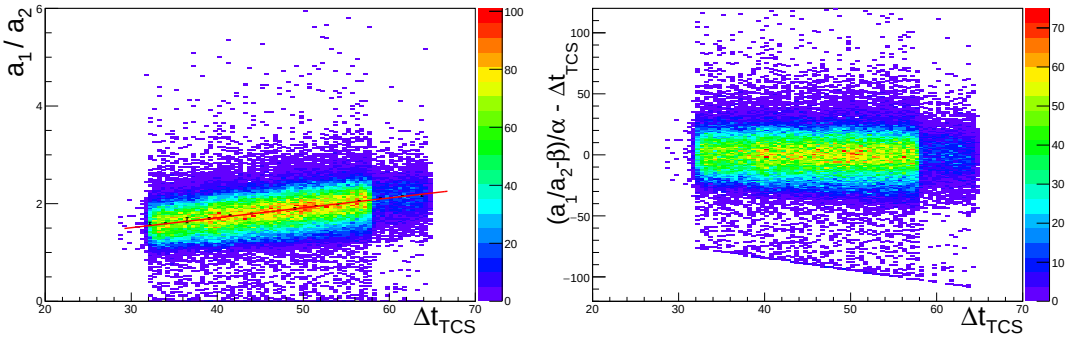

Figure 3.12: Distribution of $\frac{a_1}{a_2}$ with Δt_{TCS} (left) and $\frac{\frac{a_1}{a_2}-\beta}{\alpha}$ (right) for an APV of MP01MV (pixel) for the run 253851 of 2014

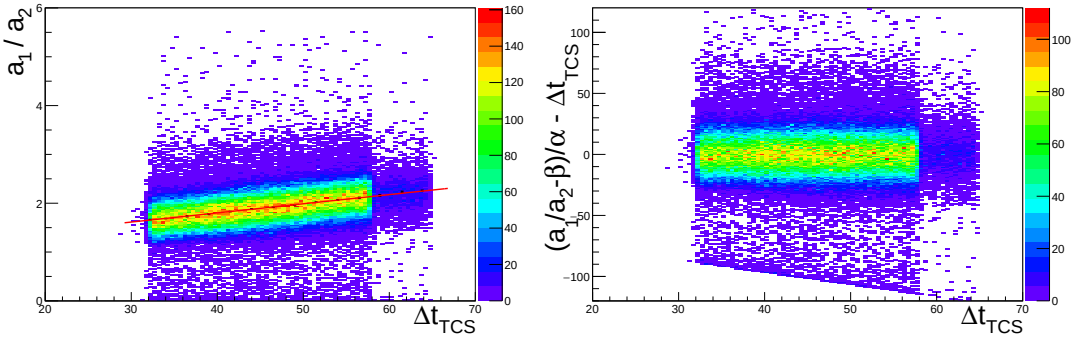

Figure 3.13: Distribution of $\frac{a_1}{a_2}$ with Δt_{TCS} (left) and $\frac{\frac{a_1}{a_2}-\beta}{\alpha}$ (right) for an APV of MP01V1 (strips) for the run 253851 of 2014

From the calculated times of all the APV of a detector, the time resolution of this detector can be measured. The t_{hit} distribution is fitted by two gaussian to take into account the dispersion of the distribution (Fig. 3.14). The time resolution can then be calculated as the weighted width of the two gaussian:

$$\sigma_{tot} = \frac{A_1\sigma_{A_1}^2 + A_2\sigma_{A_2}^2}{A_1\sigma_{A_1} + A_2\sigma_{A_2}} \tag{3.9}$$

For the 2014 runs, the time resolution for all the hybrid detectors is around 15 ns.

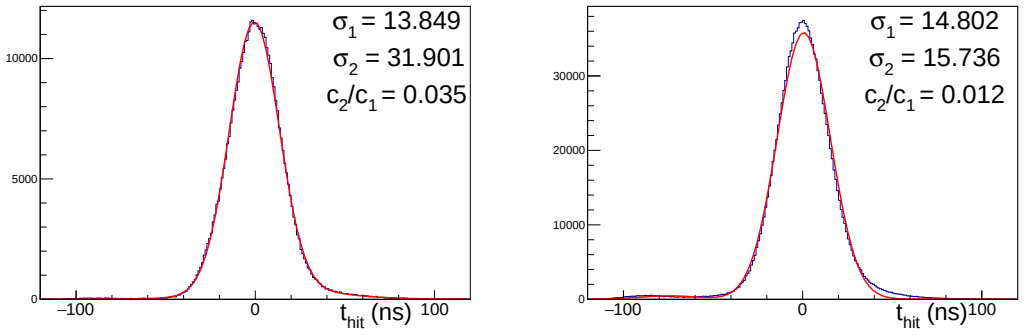

Figure 3.14: Distribution of t_{hit} for an APV of MP01MV (left) and an APV of MP01V1 (right) for the run 253851 of 2014

Time cross-talk

When the multiplexed signal is transmitted from the APV to the ADC with a frequency of 20 MHz, a part of the signal amplitude can be attributed to the previous or next channel. This phenomenon is called time cross-talk. In spite of the attempt to synchronise the APVs with the ADC, this problem can not be completely solved.

For a particular channel, the composition of the multiplexed signal leads to the fact that only certain channels will be affected by the time cross-talk. This phenomenon can therefore be seen on the distribution of residuals ($\Delta u = u_{cluster} - u_{reconstructedtrack}$, with u the coordinate of the detector plane). The peaks seen on the residual distribution in red Fig. 3.15 (left) show the hits likely to come from the time cross-talk.

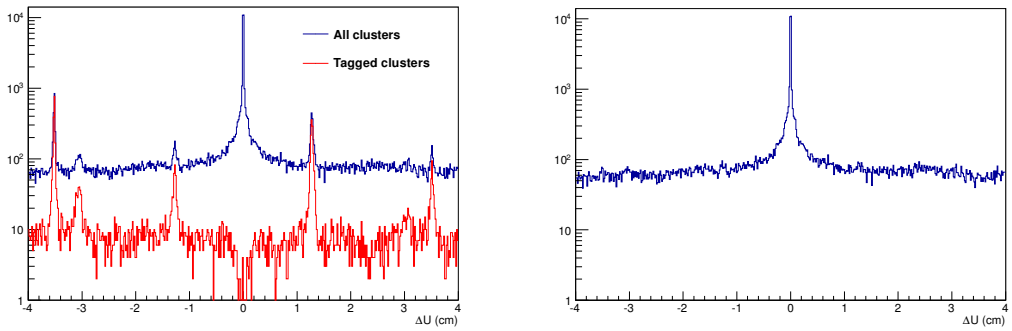

Figure 3.15: Residu distributions without cross-talk correction (left): the red curve shows the hits likely to be from the time cross-talk (in the "close" channels of the hits in the main peak); and after correction (right)

To solve this problem the distribution of the amplitude of two consecutive hits in the multiplexed signal is extracted for each APV card (Fig. 3.16). The value of the peak is saved in a calibration file, and during the reconstruction process, the amplitude of each hit is corrected by this value times the amplitude of the next or previous hit (in the mutiplexed signal). Fig. 3.15 (right) shows the residu distribution after the correction of the time cross-talk calibration.

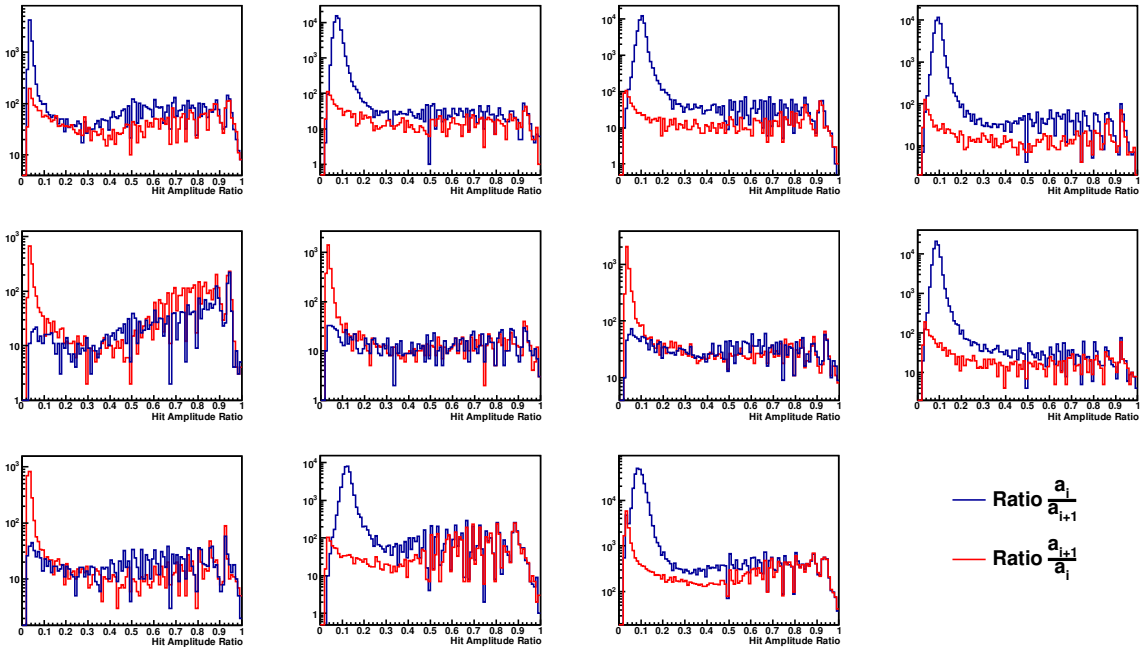

Figure 3.16: Distribution of amplitude ratios between one hit and the next or previous one in the multiplexed signal

3.4.2 Efficiency Study

The efficiency of a detector is the probability of the detector to detect a track crossing its active area. In a first place, the efficiency can be defined as:

$$\epsilon_{raw} = \frac{N_{det}}{N_{tot}} \tag{3.10}$$

, where N_{tot} the number of track crossing the active area and N_{det} the number of tracks of this sample associated with at least one cluster. But this cluster can result of another track due to the high flux or the electronic noise. The efficiency must be corrected with a background probability ϵ_{bg}, which is calculated by comparing the reconstructed tracks of an event with the detector clusters of another random event:

$$\epsilon_{bg} = \frac{N_{bg}}{N_{tot}} \tag{3.11}$$

, where N_{bg} is the number of tracks of the sample associated with at least one cluster of the other random event. This gives us a final efficiency:

$$\epsilon = \frac{\epsilon_{raw} - \epsilon_{bg}}{1 - \epsilon_{bg}} = \frac{N_{det} - N_{bg}}{N_{tot} - N_{bg}} \tag{3.12}$$

Several studies can be performed on the efficiency of the detector:

- Study the efficiency as a function of the micro-grid potential to find out in which configuration one gets the best performances, called plateau study.
- Study of 2D efficiency maps to find out local problems on the detectors or on the tracking system.

For these studies the data are reconstructed without the input of the studied detector. To gain in speed, one deals with 2 planes at once (X with Y and U with V), so for example for the X plane, the data will be reconstructed without information from the X and Y planes.

Plateau study

This study shows from which high voltage of the micro-grid the efficiency saturates (if possible with a value close to 1). The standard value used in the physics runs is $V_{mesh} = 320$ V.

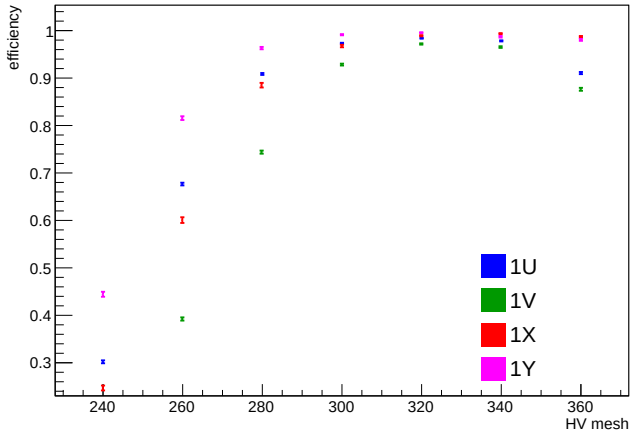

Figure 3.17: Efficiency as a function of the micro-grid potential (HV mesh) for the four detectors of the hybrid Micromegas station

Fig. 3.17 shows this study performed just after the detector of the hybrid Micromegas station were installed: the planes X and Y were new, and U and V for were already there for the past years. It shows a good efficiency at the standard value of V_{mesh} but the plane V reaches the plateau only at this value and falls at higher voltage, which does not allow much space to change this potential. This lower efficiency for U and V plane could be explained by the higher fluxes and lower energy magnetic showers since these planes are the closest to the absorber.

2D efficiency map

This study is useful to see if there is problems of tracking on particular areas of the detector. One can see on Fig. 3.18 the 2D efficiency map for the detector MP01X1 (strips).

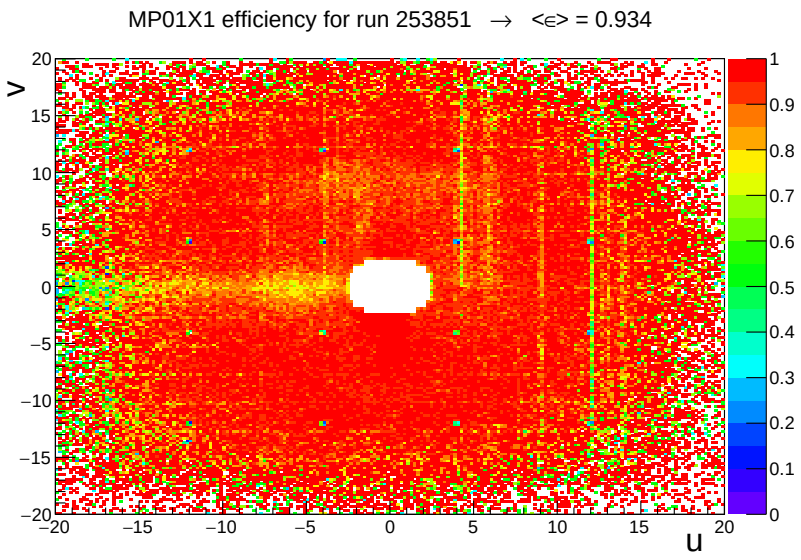

Figure 3.18: 2D efficiency map for MP01X1 for the run 253851

The overall efficiency of 93% is good but one can see a less efficient area along the X axis (u axis for this detector) on the left, as well as on the peripheral area. This could be a flaw of the detector but this less efficient areas are found also on the other planes of this station, leading to a problem of tracking coming from other detectors or from the track reconstruction. To remove this problem one can require another hit in one of the other plane of the same station of detectors. The result is shown in Fig. 3.19. The less efficient area are now fully efficient with this track selection and the overall efficiency of 97% is very good. This track selection also limits the detection area: for the X detector, this selection requires a hit in U or V since the data are reconstructed without the Y plane information, and the U and V planes are oriented at $\pm 45°$ which gives this diamond shape to the 2D efficiency map.

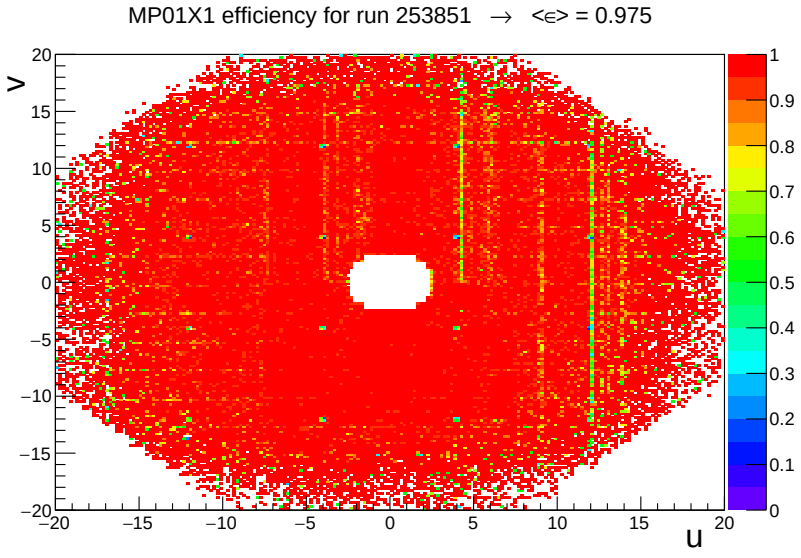

Figure 3.19: 2D efficiency map for MP01X1 for the run 253851 with requirement of a hit in another plane of the detector

There can also be some issues on the detector or known areas with less efficiency:

- One can see the 16 spacing balls (16 points which divide the detector into squares) that support the GEM foils.
- Some vertical lines (which corresponds to the orientation of the strips) shows some missing or noisy channels mostly due to the electronics.
- Fig. 3.20 shows an inefficient area in the bottom right part due to a detachment of the micro-grid.
- On the same figure, one can see a less efficient area in the right which is due to one (or several) APV card accidentally missing, which implies here that the information comes from only one strip over two.

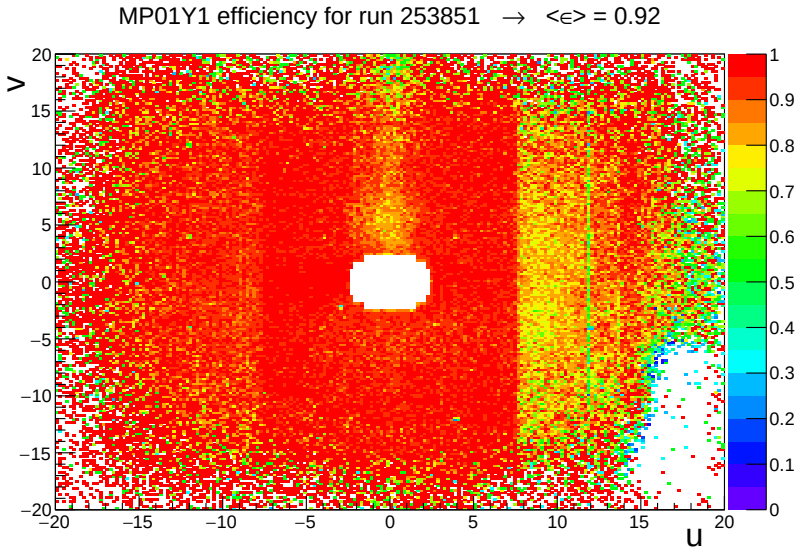

Figure 3.20: 2D efficiency map for MP01Y1 for the run 253851

This study is also done for the pixel part of the detectors. Fig. 3.21 (left) illustrates the pixel part of the MP01U detector with a few noisy channels and Fig. 3.21 (right) shows what happens when some APV cards are missing (the blue band is just some edge effects due to the binning of the histogramm).

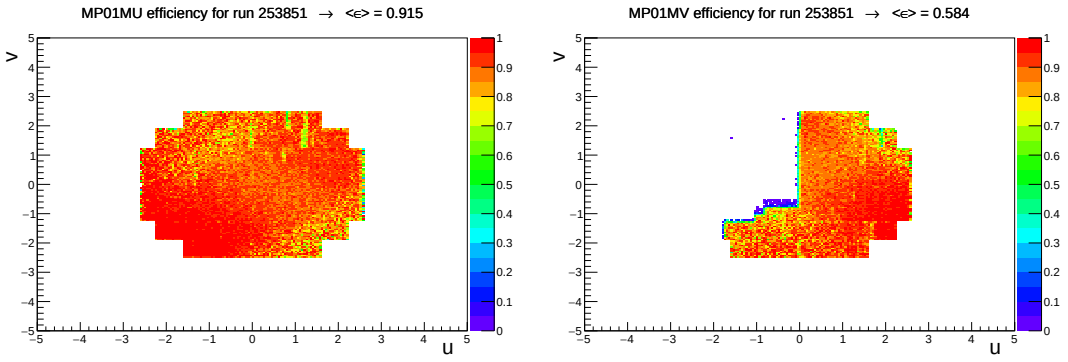

Figure 3.21: 2D efficiency map for MP0MU (left) and MP0MV (right) for the run 253851

Tab. 3.1 and Tab. 3.2 present a summary of the efficiency of all the detectors of the hybrid

Micromegas station for all the runs studied in 2014 with different types of incoming particles (muons or hadrons) and with different intensities.

run	particles	intensity ($\times 10^{11} p/spill$)	ϵ_{MP01U1}	ϵ_{MP01V1}	ϵ_{MP01X1}	ϵ_{MP01Y1}
253002	hadrons	30	0.982	×	0.943	0.968
253844	muons	25	0.991	0.971	0.983	0.980
253851	hadrons	34	0.981	0.944	0.975	0.952
254759	hadrons	100	0.821	0.748	0.958	0.925

Table 3.1: Summary of the efficiency for the strip part of the four planes of the hybrid Micromegas station for all the runs studied in 2014 with the requirement of a hit in the same detector station

The strip part of detectors shows a really good efficiency (except for MP01V1 for the run 253002 that was not working) for both muon and hadron beams. The results of the run 254759 at higher intensity show that the detectors MP01U1 and MP01V1, more upstream and closer to the hadron absorber are affected by low energy electromagnetic showers, and hence have a lower efficiency.

run	particles	intensity ($\times 10^{11} p/spill$)	ϵ_{MP01MU}	ϵ_{MP01MV}	ϵ_{MP01MX}	ϵ_{MP01MY}
253002	hadrons	30	0.803	×	0.35	0.483
253844	muons	25	0.95	0.532	×	0.968
253851	hadrons	34	0.915	0.584	×	0.917
254759	hadrons	100	0.841	0.319	×	0.879

Table 3.2: Summary of the efficiency for the pixel part of the for the four planes of the hybrid Micromegas station for all the runs studied in 2014

The pixel parts show also good results in the zones where the electronic was activated. For the run 253002, only a few electronic cards were active so the results won't be discussed. For the other run, MP01MX had no electronic cards and MP01MV had only 6 of them connected. One can see that the efficiency is affected both by the change of type of incoming particles: the efficiency decreases for hadron beams, and with the intensity of the beam: all the planes have a lower efficiency for the run 254759. Even though the detectors are sensitive to these changes, they show an efficiency higher than 80% in a zone, which was not covered before and which is subject to very high intensities.

3.4.3 Spatial Resolution

The spatial resolution measures the uncertainty on the position of a passage of a track through the detector. It is calculated using the distribution of residuals $\Delta u = u_{track} - u_{hit}$. For this analysis also, the studied detector is left out of the reconstruction (and as the efficiency study, the detector were treated two at a time, U with V and X with Y). Thanks to this the position u_{track} and u_{hit} are independent, so that:

$$\sigma^2_{\Delta u} = \sigma^2_{u_{track}} + \sigma^2_{u_{hit}} \tag{3.13}$$

$$\sigma_{det} = \sqrt{\sigma^2_{\Delta u} - \sigma^2_{u_{track}}} \tag{3.14}$$

Unfortunately the tracks can have sometime a deteriorated tracking and a selection on the track resolution is required to extract a realistic spatial resolution of the detector (one needs

$\sigma^2_{\Delta u} \geq \sigma^2_{u_{track}}$). This selection is done by hand by looking at the track resolution distribution. For most of the cases, it was chosen to remove the tracks with a resolution greater than 70 μm.

Before looking at the distributions, one first needs to correct some alignment errors:

- Correction of a rotation in the plane perpendicular to the beam through the 2D distribution Δu as a function of v.
- Correction of the bias in the 2D distribution Δu as a function of u.

Correction of a rotation in the plane perpendicular to the beam

A rotation of an angle ϕ introduces a bias in the measurement of the position u as illustrated in Fig. 3.22.

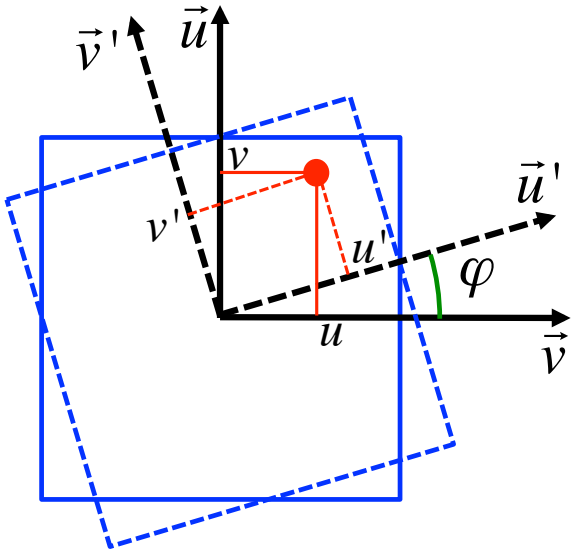

Figure 3.22: Schema of a rotation of angle ϕ between the orientation in the alignment file and the real one

Let us call u' and v' the position the rotation, one gets the equations:

$$u' = u\cos\phi + v\sin\phi \quad (3.15)$$
$$v' = -v\sin\phi + u\cos\phi \quad (3.16)$$

Which gives us at the first order:

$$\delta u = u - u' \approx v \cdot \phi \quad (3.17)$$

By identifying δu with $\langle \Delta u \rangle$ in the 2D distribution of Δu as a function of v, one can measure the angle ϕ. This angle can then be subtracted of the angle in the alignment file. Fig. 3.23 shows the 2D distribution of Δu as a function of v before and after the correction of the angle of the detector.

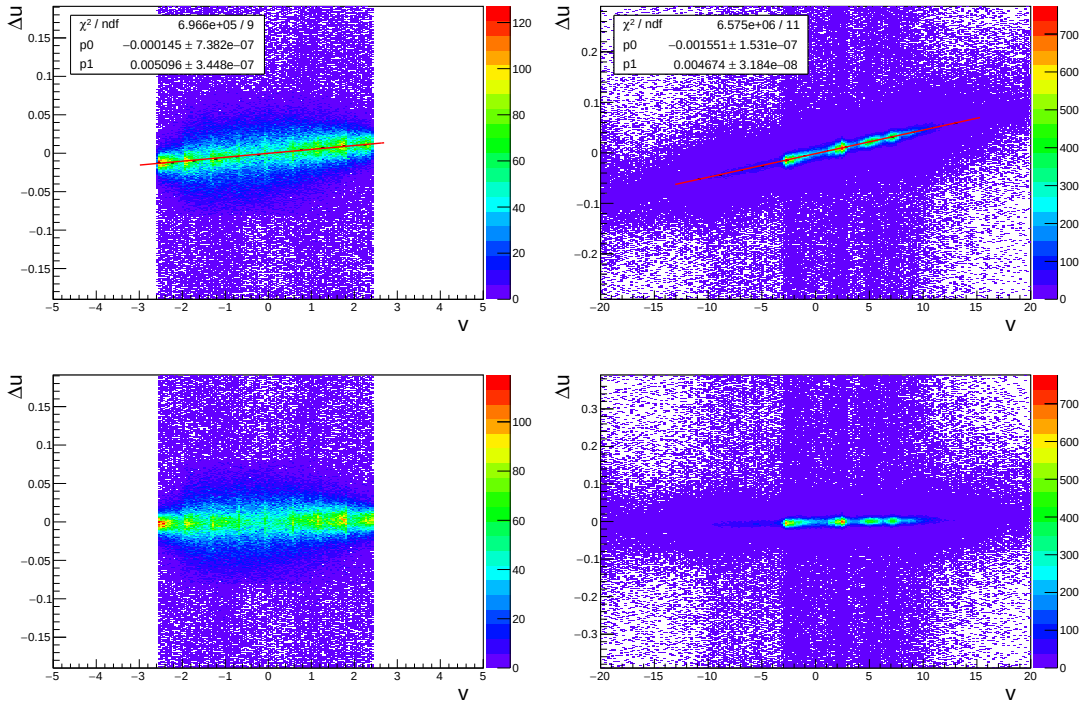

Figure 3.23: 2D distribution of Δu as a function of v before (top) and after (bottom) correction for MP01MY (left) and MP01Y1 (right) for the run 253844

Correction of the $\Delta u/u$ bias

To correct this bias, there exists a technique of correction of the longitudinal position. Indeed if the longitudinal beam (along the beam) is incorrect in the alignment file, it creates a bias on the Δu distribution as illustrated in Fig. 3.24:

$$tan\,\theta \quad = \frac{u}{z} \quad = \frac{\delta u}{\delta z} \tag{3.18}$$

$$\delta u \quad = (\frac{z+\delta z}{z} - 1) \cdot u \quad = \alpha u \tag{3.19}$$

By identifying δu and $\langle \Delta u \rangle$, one can determine the parameter α and then the new position of the detector $z' = (\alpha + 1)z$.

Unfortunately this method didn't improve the bias of Δu as a function of u, which must have another unknown cause. We chose to compute the spatial resolution of the detector after an affine transformation:

$$\Delta u' = \Delta u - \alpha u \tag{3.20}$$

, and then to integrate over the variable u as illustrated in Fig. 3.25.

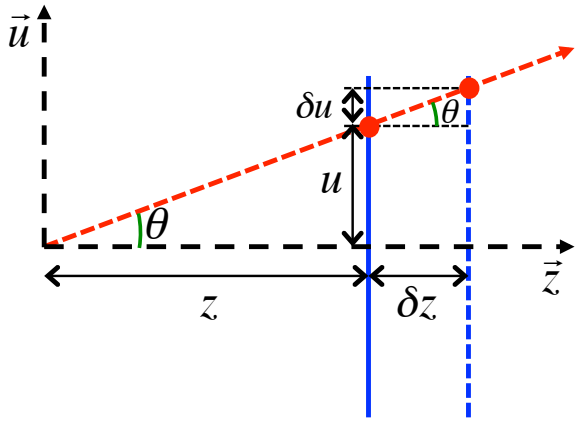

Figure 3.24: Schema of the difference between the real longitudinal position of the detector and the one used in the reconstruction. The red arrow represents the track of a particle with an angle θ

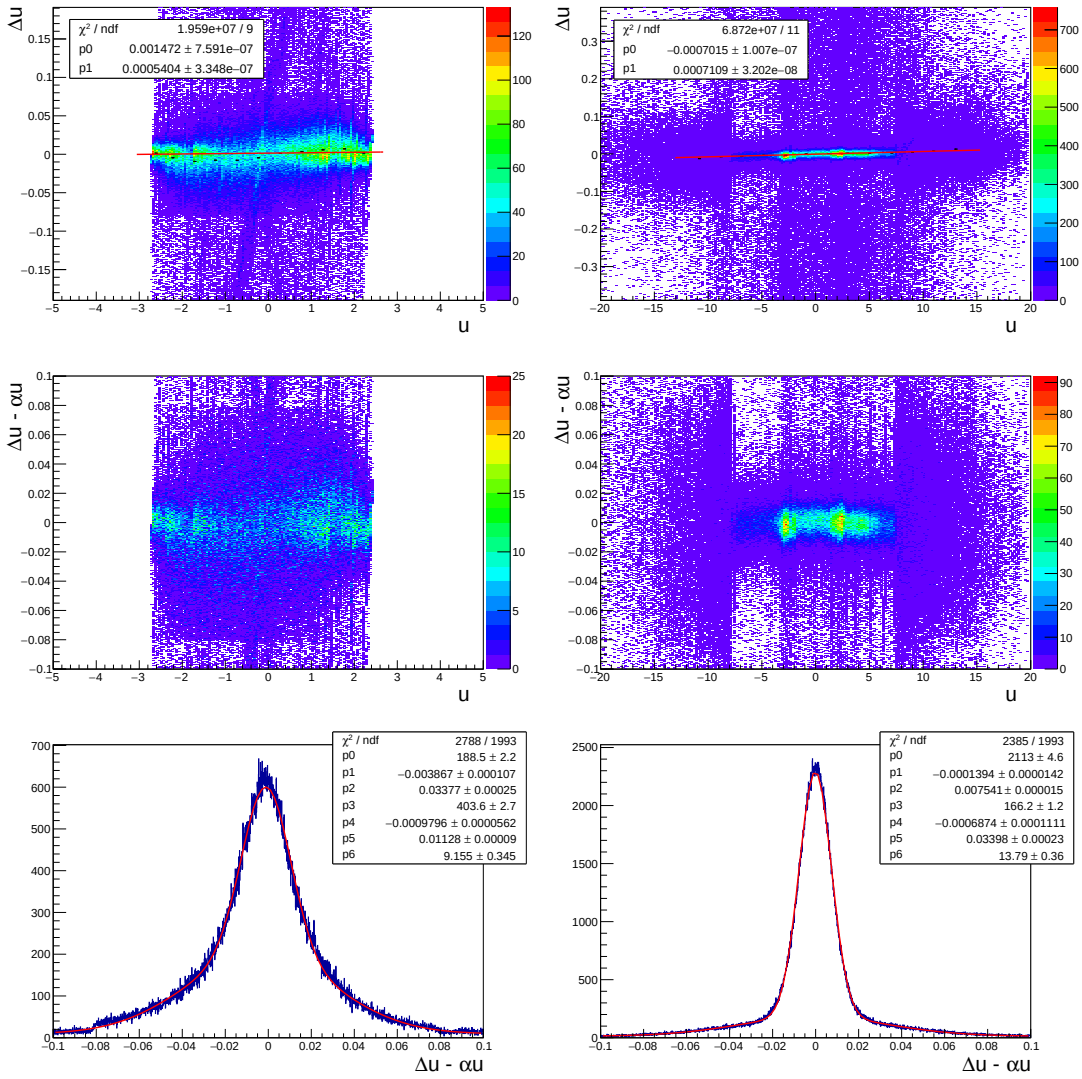

Figure 3.25: 2D distribution of Δu as a function of u before correction (top), and 2D distribution of $\Delta u'$ as a function of u after correction (center) and integrated over u (bottom) for MP01MY (left) and MP01Y1 (right) for the run 253844

The spatial resolution is then obtained using the same method as for the time resolution: one uses a fit with two gaussians and the spatial resolution is the weighted mean of the two gaussian width (Eq. 3.9).

Tab. 3.3 presents a summary of the spatial of all the detectors of the hybrid Micromegas station only for the muon run studied in 2014 (253844), which is the most suited for the study of the spatial resolution of the detector thanks to cleaner tracks. This values are also obtained with geometrical cuts added to select zones where all the electronic cards were functioning and where the tracking was satisfying enough to extract this spatial resolution.

detector plane	U	V	X	Y
σ_{strips} (μm)	61.6	65.4	76.0	73.6
σ_{pixels} (μm)	62.7	×	×	72.6

Table 3.3: Summary of the spatial resolutions for the four planes of the hybrid Micromegas station for the run 253844

Conclusion

The first station of pixel Micromegas showed good performances for the 2014 Drell Yan commissioning run as well in efficiency (97% for muon runs and up to 95% for hadron runs) as in time resolution (16 ns). The results on the spatial resolution that require more track selection are also very satisfying with values around 70 μm for both the pixel and strip parts.

For the 2015 Drell Yan run, the three stations of Micromegas have been replaced by pixel Micromegas and the same study is ongoing.

Chapter 4

Asymmetry Measurements and Analysis Results

4.1 Asymmetry Measurement

4.1.1 Definition of Asymmetry and Hadron Yields

As it has been seen in the first chapter Chap. 1, one needs to compute from the experimental data the asymmetry of polarised cross-sections for the reaction $\mu\, p \rightarrow \mu'\, h\, X$:

$$A_{LL}^{h} = \frac{\overset{\rightleftarrows}{\sigma^{h}} - \overset{\rightrightarrows}{\sigma^{h}}}{\overset{\rightleftarrows}{\sigma^{h}} + \overset{\rightrightarrows}{\sigma^{h}}} \tag{4.1}$$

Each separated cross-section can be expressed as:

$$\sigma^{h} = \frac{N^{h}}{\Phi a n} \tag{4.2}$$

where N^h is the yield of hadron, Φ the beam flux, a the spectrometer acceptance and n the density of the target material. Computing these separated polarised cross-sections would be a really intricate job here since some factors in the asymmetry should cancel out in the division. Fortunately the experimental set-up of COMPASS allows us to compute the asymmetry more directly only with the hadron yields and some information on the target material. The methods described below were introduced by SMC and adapted to COMPASS, and are largely based on the internal notes [81] and [82].

The measurement of the asymmetries comes from the counting of hadron yields for each cell of the target N_{cell}^{h}, where the material is polarised in opposite directions. And this quantity can be expressed as a function of the asymmetry 4.4:

$$\begin{aligned} N_{cell}^{h} &= \Phi a_{cell} n_{cell} \sigma_0 (1 + P_{cell} P_b f A_{LL}^{h}) && (4.3) \\ &= \alpha_{cell}(1 + \beta_{cell} A_{LL}^{h}) && (4.4) \end{aligned}$$

, where σ_0 is the unpolarised cross-section and $\sigma_0 P_{cell} P_b f A_{LL}^{h}$ is the origin of excess or deficit of hadron yield due to polarisation. This last term is indeed weighted by the beam polarisation P_b and the target cell polarisation P_{cell}, giving the sign and the linear effect of the asymmetry on the hadron yield. The weighting factor also includes a dilution factor f, which represents the fraction of polarisable material in the target.

The asymmetry of cross-sections can first be intuitively computed through the asymmetry of hadron yields. Let's note u the upstream cell of the target and d the downstream cell. If the

target is in the configuration where P_u and P_b have opposite signs, the asymmetry of hadron yields will give:

$$\frac{N_u^h - N_d^h}{N_u^h + N_d^h} = \frac{r - 1 + wA_{LL}^h(r|P_u| + |P_d|)}{r + 1 + wA_{LL}^h(r|P_u| - |P_d|)} \tag{4.5}$$

,where $w = P_b f$ and $r = a_u n_u / a_d n_d$ is the ratio of the cell acceptances. For a three cells target, the computation method is the same as using two virtual cells: the joining of the upstream and downstream cells that will be noted u and the central cell that will be noted d. This last expression Eq. 4.5 can be simplified, reasonably assuming that $wA_{LL}^h \ll 1$ and $|r - 1| < 0.1$:

$$\frac{N_u^h - N_d^h}{N_u^h + N_d^h} = wP_t A_{LL}^h + \frac{r - 1}{r + 1} \tag{4.6}$$

,where P_t is the average of target cell polarisation modulus. The term $(r-1)/(r+1)$ produces an asymmetry of acceptances, which can be dealt with by averaging asymmetries of two consecutive periods separated by a rotation of the solenoid magnetic field as explained in Sec. 4.1.4. The quantities of the second period will be noted with the prime symbol. The computation is done without the assumptions done in Eq. 4.6 but by assuming $r = r'$. In the second period, P_u and P_d will have opposite signs giving the following expressions:

$$A_{LL}^h = \frac{1}{2}\frac{1}{1-\rho^2}\frac{1}{wP_t}\left(\frac{N_u^h - N_d^h}{N_u^h + N_d^h} + \frac{N_d'^h - N_u'^h}{N_d'^h + N_u'^h}\right) \tag{4.7}$$

$$\delta A_{LL}^h = \frac{1}{2}\frac{1}{\sqrt{1-\rho^2}}\frac{1}{wP_t}\sqrt{\frac{1}{N_u^h + N_d^h} + \frac{1}{N_d'^h + N_u'^h}} \tag{4.8}$$

, where ρ is the asymmetry of target cell acceptances. The quantities after the field rotation are quoted with prime notation and δA_{LL}^h is the statistical uncertainty associated with A_{LL}^h. This first order method has the benefit of being intuitive but the asymmetry of cell acceptances is not always negligible and requires Monte-Carlo simulation for its estimation.

4.1.2 2^{nd} Order Method for Asymmetry Calculation

A second order method was developed in SMC to compute asymmetries with non negligible cell acceptances asymmetry. This method originates from the same hadron yields given in Eq. 4.4, but in order to cancel out the acceptance a'_{cell} with a_{cell}, the quantity we look into is the ratio of hadron yield polarised in one direction over the hadron yields oppositely polarised:

$$\xi = \frac{N_u^h N_d'^h}{N_d^h N_u'^h} = \frac{\alpha_u \alpha'_d}{\alpha_d \alpha'_u}\frac{(1 + \beta_u A_{LL}^h)(1 + \beta'_d A_{LL}^h)}{(1 + \beta_d A_{LL}^h)(1 + \beta'_u A_{LL}^h)} \tag{4.9}$$

As in the first order method, one can assume $(\alpha_u \alpha'_d)\ (\alpha_d \alpha'_u) = 1$ and one gets to solve a second order equation:

$$0 = \nu_2 (A_{LL}^h)^2 + \nu_1 A_{LL}^h + \nu_0 \tag{4.10}$$

$$\begin{aligned} \nu_2 &= \xi\beta_d\beta'_u - \beta_u\beta'_d \\ \nu_1 &= \xi(\beta_d + \beta'_u) - (\beta_u + \beta'_d) \\ \nu_0 &= \xi - 1 \end{aligned}$$

δA_{LL}^h can also be calculated by deriving the equation Eq. 4.10 with respect to ξ. The uncertainty of ξ is computed by uncertainty propagation of the error on N_{cell}^h which follows a Poisonian distribution, one gets then:

$$\sigma_\delta^2 = \frac{1}{N_u^h} + \frac{1}{N_d^h} + \frac{1}{N_u'^h} + \frac{1}{N_d'^h} \tag{4.11}$$

4.1.3 fP_b-Weighted Asymmetry

Another method was developed by the SMC collaboration to optimise the statistical uncertainty of the asymmetry by weighting the hadron yields by the analysing power of their associated event, which consists mostly in $w = fP_b$. So instead of using directly N^h_{cell}, one uses p^h_{cell}:

$$p^h_{cell} = \int N^h_{cell} w d\vec{x} = \int \Phi n_{cell} \sigma_0 d\vec{x} \langle\alpha\rangle_w (1 + \langle\beta\rangle_w A^h_{LL}) \tag{4.12}$$

, where $d\vec{x}$ represents the measure of all unbinned variables, and:

$$\langle\alpha\rangle_w = \frac{\int \Phi n_{cell} \sigma_0 w \alpha_{cell} d\vec{x}}{\int \Phi n_{cell} \sigma_0 w d\vec{x}} \tag{4.13}$$

$$\langle\beta\rangle_w = \frac{\int \Phi n_{cell} \sigma_0 w \alpha_{cell} \beta_{cell} d\vec{x}}{\int \Phi n_{cell} \sigma_0 w \alpha_{cell} d\vec{x}} \tag{4.14}$$

These quantities are calculated in the same way as before, only adding the weight w for each hadron:

$$p^h_{cell} = \sum_{i,cell} w_i \tag{4.15}$$

$$\langle\beta_{cell}\rangle_w = \sum_{i,cell} w_i \beta_{i,cell} \tag{4.16}$$

The asymmetry is then extracted using the same equation Eq. 4.10 replacing N^h_{cell} by p^h_{cell} in ξ and β_{cell} by $\langle\beta_{cell}\rangle_w$. For the calculation of the error this leads to:

$$\sigma_\xi = \frac{1}{\sum_{i\in u} w_i^2} + \frac{1}{\sum_{i\in d} w_i^2} + \frac{1}{\sum_{i\in u'} w_i^2} + \frac{1}{\sum_{i\in d'} w_i^2} \tag{4.17}$$

4.1.4 Data Grouping

As explained before, the data needs to be grouped to compute the asymmetries. For each cycle of magnetic solenoid field rotation (16-24 h depending on the years), one can compute one asymmetry using the data before and after the field rotation as shown in the previous sections and shown in Fig. 4.1 for a three cells target.

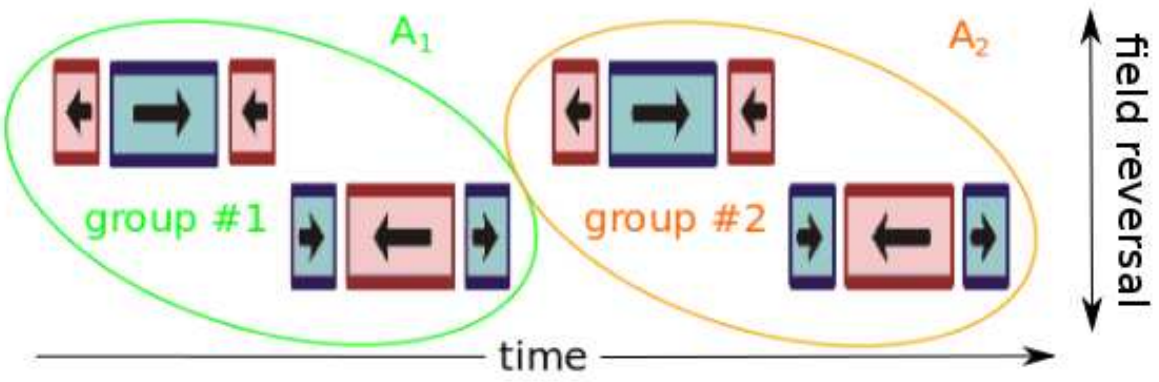

Figure 4.1: Schema presenting data grouping through target cell polarisation

This method unfortunately brings a possible source of systematic errors due to the correlation between the spin states and the magnetic solenoid field. Indeed for one cell and one

solenoid field direction, the spin state will always be the same. To avoid this bias, the COMPASS set-up allows to reverse the polarisation by changing the microwave frequency used in the Dynamic Nuclear Polarisation process. This polarisation reversal is done about once in a year. These microwave configurations will be noted + and -.

The asymmetry is computed for each of these half-year periods through a weighted average:

$$A_{LL}^{h\,\pm} = \sigma^2_{A_{LL}^{h\,\pm}} \sum_{i\in\pm} \frac{A_{LL}^{h\,i}}{\sigma^2_{A_{LL}^{h\,i}}} \tag{4.18}$$

, where $\sigma^2_{A_{LL}^{h\,\pm}} = \sum_{i\in\pm} 1/\sigma^2_{A_{LL}^{h\,i}}$. The weight $1/\sigma_{A_{LL}^{h}}$ corresponds roughly to the hadron yield for all cells N_{tot}^h. The final asymmetry is then just the average of A_{LL}^{h+} and A_{LL}^{h-} without weighting by the hadron yield this time to avoid remaining systematic uncertainties:

$$A_{LL}^{h} = \frac{A_{LL}^{h+} + A_{LL}^{h-}}{2} \tag{4.19}$$

The number of groups for each year and each microwave setting configuration is summarised in Tab. 4.1.

	2002	2003	2004	2006	deuteron data	2007	2011	proton data
+	22	28	36	12	98	11	20	31
-	22	25	50	18	115	12	20	32
total	44	53	86	30	213	23	40	63

Table 4.1: Summary of the number of groups for each year and for each microwave setting configuration

4.2 Data selection

Before computing the asymmetry, a thorough selection has to be done to have clean and stable data, and to place oneself in the kinematic domain where one can compare the data to the theoretical predictions. This selection is done in three steps: identification of bad spills, event selection and hadron selection.

The two last selections are close to the ones used for the analysis on unpolarised cross-section in order to remain in the kinematic domain of applicability of the theoretical framework [30].

4.2.1 Study of Bad Spills

The first selection done on reconstructed data is to move aside spills that are not stable and could add a lot of systematic uncertainties. This selection is not particular to this analysis, contrary to the event and hadron selection.

Some general criteria of the run are first studied like the number of spills per run, the number of detector planes having errors. These data are obviously discarded.

After this preliminary study, some macro-variables of the spill are investigated:

- Number of primary vertices per event.
- Number of tracks per primary vertex.
- Number of beam tracks per event.

For the earlier years only the ratio of acceptances for up and downstream target cells of these macro-variables is investigated. If this ratio is changed, the data are discarded. For the later years, data for which the number of neighbour in a given period is below a threshold for any of the macro-variables, are discarded.

4.2.2 Event Selection

The first selections that one can do are related to the inclusive variables of the $\mu \rightarrow \gamma^* \mu'$ process. Each event is required to have an incoming and scattered muon as well as a vertex in the target cells, inside the polarized material. Moreover the incoming muon must go through all the target material in order to equalise flux between the different target cells. Since we are interested in semi-inclusive processes, one requires also that the number of outgoing particles to be strictly more than one. Then follows the selection on kinematic variables:

- $140 < p_\mu < 180$ GeV/c for 2002 to 2007 and $185 < p_\mu < 215$ GeV/c for 2011, to remain close to the nominal beam line momentum ($p_\mu = 160$ GeV/c for 2002 to 2007 and $p_\mu = 200$ GeV/c for 2011), which is also used in the theory. Additionally there is a cut on the uncertainty of this value to reject incoming muons which track momentum is not well known $\sigma_{|q|/p_\mu} < 20.10^{-9}$ $(\mathrm{c/GeV})^2$.

- $Q^2 < 1$ GeV^2 to be in the photoproduction regime that is required by the theoretical framework.

- $0.1 < y < 0.9$, the lower cut is to reject badly reconstructed virtual photons and the higher one is to remove events which might be strongly affected by radiative events.

Some important variables related to the incoming beam or the event vertex are shown in Fig. 4.2.

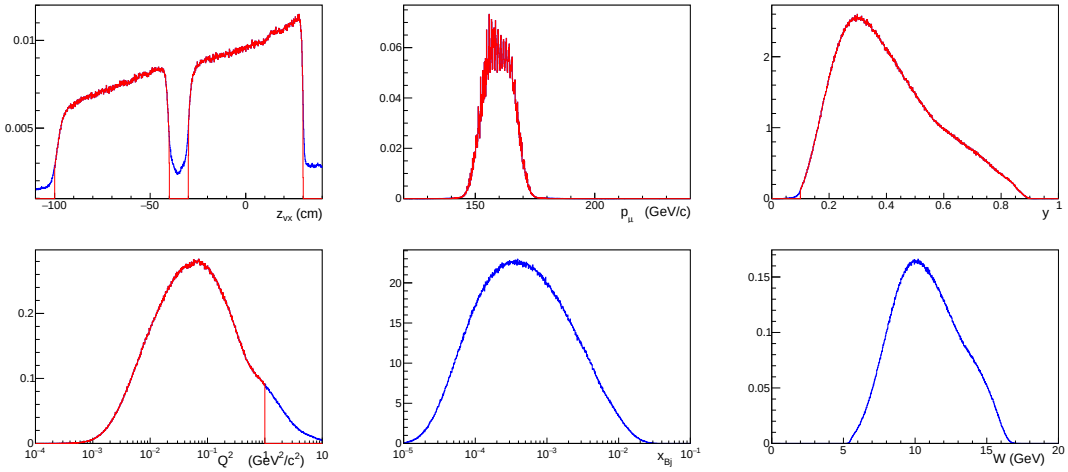

Figure 4.2: Some distributions for the period 2002-2004. The variables presented are z_{vertex} (top left), p_μ (top center), y (top right), Q^2 (bottom left) and x_{Bj} (bottom center) and w (bottom right). The blue (resp. red) line shows the final distribution without (resp. with) its respective cut

4.2.3 Hadron Selection

One needs then to do a selection on the semi-inclusive process $\mu\, p \rightarrow \mu'\, h\, X$. In the kinematic domain of this analysis, these kind of events can be triggered by the Inner Trigger (IT), the Ladder Trigger (LT), the Middle Trigger (MT) or the Calorimeter Trigger (CT), which correspond each to different kinematic domains. In order to not miss any event, the inclusive Middle Trigger (iMT) is also used. The y distributions are shown by trigger in Fig. 4.3, starting by IT, then MT, LT and CT (the remaining iMT is not visible).

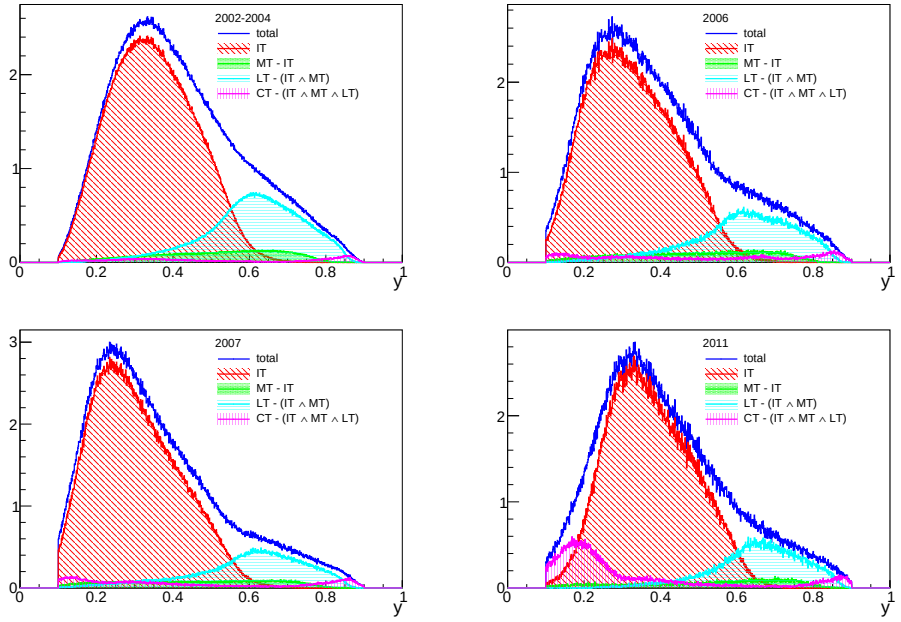

Figure 4.3: Distributions of y for the different triggers used in the analysis

To only retain good tracks, one has to require that they don't cross the solenoid magnet vessel, for this one does a radial cut at the downstream end of the solenoid magnet, this cut depends of course on the target used and it is much wider starting from 2006.

To be sure that the outgoing particles are hadrons, one discards muons by requiring that the number of radiation lengths crossed by the particle has to be smaller than 15; and one discards electrons with a momentum below 8 GeV/c with a cut on RICH likelihoods: $LK_e < 1.8LK_\pi$.

Then follows some cuts on the hadron kinematics:

- $p_T > 0.7$ GeV/c, this variable provides the hard scale for the theoretical QCD calculations: $\mu^2 \approx p_T^2 > 1$ (GeV/c)^2; the cut is chosen wider to have more statistics for the systematic uncertainties study, but only points where $p_T > 1$ GeV/c are compared to the theoretical calculations.

- $0.2 < z < 0.8$, the higher cut is required to avoid contribution from diffractive scattering and the lower one is in order to reject hadrons coming from target fragmentation.

- $0.01 < \theta_h < 0.12$ rad which corresponds roughly to the limits of the spectrometer angular acceptance.

- The final cut on the pseudo-rapidity ($\eta_h = -ln(tan(\theta_h/2)) - 0.5ln(2E_\mu/M_N)$) is a more accurate way of dealing with the spectrometer angular momentum acceptance, since it is the variable used in the theoretical calculations and will be used in the determination of the binning. This cut depends on the setup used for each year:

  - 2002-2004: $0.45 < \eta_h < 2.4$ (which corresponds to $0.01 < \theta_h < 0.07$ rad)
  - 2006-2011: $-0.1 < \eta_h < 2.4$ (which corresponds roughly to $0.01 < \theta_h < 0.12$ rad)

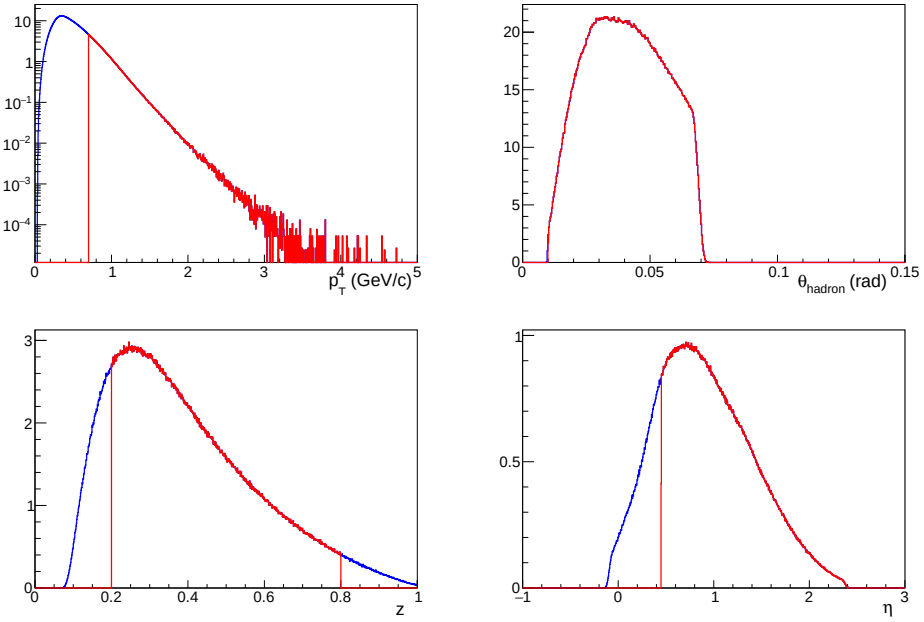

Figure 4.4: Some distributions for the period 2002-2004. The variables presented are p_T (top left), θ_h (top right), z (bottom left) and η_h (bottom right). The blue (resp. red) line shows the final distribution without (resp. with) its respective cut

The variables related to the hadron are shown in Fig. 4.4.

4.2.4 Amount of Data and Selection Ratios

The number of events Tab. 4.2 or hadrons Tab. 4.3 are presented cut after cut with their ratio for all deuteron and proton data. The final number of hadrons by year is summarised in Tab. 4.4

	Deuteron		Proton	
Cut	Events ($\times 10^6$)	Ratio(%)	Events ($\times 10^6$)	Ratio(%)
All events	7468.1	100.0	15744.3	100.0
Has BPV	6828.0	91.4	11868.4	75.4
Has μ and μ'	3901.3	52.2	3391.8	21.5
Has 2 or more particles	2497.4	33.4	2009.2	12.8
Vertex is in target region	1714.3	23.0	2009.2	12.8
Crossed all target cells	1643.6	22.0	1584.3	10.1
Beam momentum cut	1639.3	22.0	1515.9	9.6
$0.1 < y < 0.9$	1583.8	21.2	1379.9	8.8
$Q^2 < 1$ GeV^2	1448.9	19.4	1236.5	7.9
$\max(p_T) > 0.7$	219.1	2.9	228.7	1.5

Table 4.2: Event selection for all deuteron and proton data

Cut	Deuteron		Proton	
	Hadrons ($\times 10^6$)	Ratio(%)	Hadrons ($\times 10^6$)	Ratio(%)
All tracks	724.8	100.0	1030.8	100.0
triggered	721.1	99.0	1029.6	99.0
don't cross solenoid	698.3	96.0	1026.8	99.0
not muon	694.9	95.0	1023.8	99.0
$p_T > 0.7$	220.2	30.0	264.3	25.0
$0.2 < z < 0.8$	139.3	19.0	118.4	11.0
$0.01 < \theta < 0.12$	136.4	18.0	109.2	10.0
not electron	133.2	18.0	106.0	10.0
fringe field	133.2	18.0	106.0	10.0
$-0.1(0.45) < \eta < 2.4$	116.6	15.5	105.4	10.2

Table 4.3: Hadron selection for all deuteron and proton data

period	2002	2003	2004	2006	^{6}LiD	2007	2011	NH_3
#hadrons ($\times 10^6$)	13.61	25.28	43.01	34.71	116.61	65.91	39.52	105.43

Table 4.4: Final number of hadrons for each year and combined for each target material

4.2.5 Asymmetry Binnings

At first A_{LL} was only computed as a function of p_T. To get acceptable statistical uncertainties, one chose the p_T-binning: [1.0,1.25,1.5,2.0,2.5,4.0] (GeV/c). To do the systematic study one expanded the p_T domain to 0.7 GeV/c, adding 4 equal populated bins [0.7,0.75,0.8,0.9,1.0].

It can be noted that the theoretical kinematic cuts presented in Sec. 1.2.5 do not match the one presented for this analysis (presented in Sec. 4.2.2 and Sec. 4.2.3). As it will be further explained in Sec. 5.1, different sets of non perturbative distributions will also be changed in the theoretical calculations and distort the asymmetries.

A study to look in details at the impact of each of these changes has been performed in Sec. 5.1 by changing one parameter at a time. For the kinematic cuts, most of the changes do not impact much the asymmetries, except for the change of η_h integration interval. Fig. 4.5 shows the asymmetries computed in [4] (left) compared to the same asymmetries with just the change of η_h domain from [0.44,2.4] to [-0.1,2.4] (right).

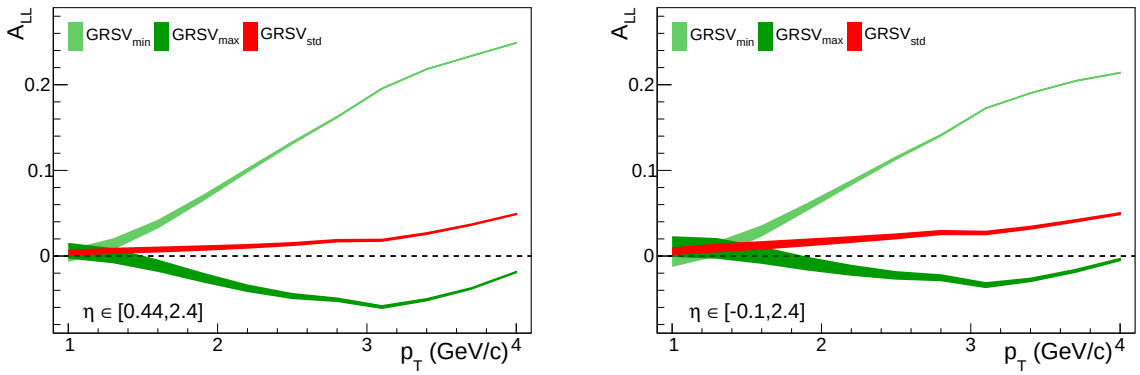

Figure 4.5: $A_{LL}(p_T)$ for a deuteron target with original inputs and kinematic domains (left), and with change of η_h integration interval (right). Uncertainty bands come from the unknown polarised structure of the photon (Sec. 1.2.1)

One can see a substantial loss of sensitivity of the asymmetries to ΔG depending on the range of η_h.

A way to regain the loss of sensitivity coming from the expansion of the η_h domain is to separate the data in several bins of η_h. Moreover since it was also chosen to do a selection on η_h ($0.45 < \eta_h$ for 2002-2004), data couldn't have been combined due to the different range of η_h. To get the best sensitivity to ΔG, we studied the impact of the η_h binning on this sensitivity.

This sensitivity can be quantified using the extreme cases of PDFs of the GRSV parameterisation (GRSV_{min}, GRSV_{max}) and the statistical uncertainty of the experimental asymmetries:

$$\alpha = \sqrt{\sum_{year}\sum_{i_\eta}\sum_{i_{p_T}}\left(\frac{H(A_{LL\,i_\eta\,i_{p_T}}^{GRSV_{min}} - A_{LL\,i_\eta\,i_{p_T}}^{GRSV_{max}}, 0)}{\sigma_{data\,i_\eta\,i_{p_T}}^{stat}}\right)^2} \tag{4.20}$$

$$= \sqrt{\sum_{year}\sum_{i_\eta}\sum_{i_{p_T}}\beta_{i_\eta,i_{p_T},year}} \tag{4.21}$$

, where i_η and i_{p_T} are the index relative to the η_h binning and to the p_T binning. H is here the Heaviside function applied in 0, it is used to nullify the sensitivity at low-p_T where the asymmetries are superposing.

As will be shown in Sec. 5.4, this quantity depends also on the parameterisation used in the calculation of the theoretical asymmetries. Only the FF parameterisations represent a relevant impact to this sensitivity and the values presented in this section are calculated for DSS07.

Since the selection $\eta_h > 0.45$ for 2002-2004 implies a first η_h-bin [-0.1,0.45], it was decided to use three η_h-bins. The results for one η_h-bin and for three are presented in Tab. 4.5 and Tab. 4.6 In order to simplify the situation, one kept the same η_h binning for deuteron and proton data: [-0.1,0.45,0.9,2.4]. By changing this binning from one single bin to three bins, one gains 130% sensitivity for the deuteron asymmetries and 90% for the proton asymmetries.

target	deuteron	proton
α	6.47	5.69

Table 4.5: Table of sensitivity to ΔG for one η_h bin

[-0.1,0.45,x,2.4]	0.7	0.8	0.9	1.0	1.1	1.2	1.3
$\alpha_{deuteron}$	14.51	14.59	14.73	14.68	14.40	13.92	9.88
α_{proton}	10.49	10.71	10.97	9.69	11.10	10.89	7.54

Table 4.6: Table of sensitivity to ΔG for three η_h bins

4.3 Systematic Study

4.3.1 Different Types of Systematic Uncertainties

The asymmetries are sensitive to different kind of systematic effects:

- False asymmetries representing the asymmetries due to the setup.
- Multiplicative uncertainties coming from uncertainty on the measurement of variables used in the analysis such as P_b, P_{cell}, f.
- Uncertainties coming from unknown radiative corrections.

4.3.2 Unphysical Asymmetries

One begins the systematic uncertainty study by a mostly qualitative study on the false asymmetries. One often only checks the compatibility of the false asymmetry with zero in the case that the calculated quantity represents an asymmetry, and that the difference with asymmetries calculated for separated parts of the data is compatible with zero in the other case. A lot of false asymmetries can be calculated, only the most relevant ones are presented here, the other ones are cited in the end of this section. All these "false asymmetries" are calculated for positive/negative hadrons and for every year but one shows here only the results averaged for each target material and for all hadrons.

- As it has been seen in the Sec. 4.1.4, asymmetries are computed through small groups separated by a solenoid field reversal to cancel out the false asymmetry coming mostly from the difference in cells acceptance but also from the possible inhomogeneity of the target cells. We can compute what we call "misconfiguration false asymmetry" using the same groups but separated with two solenoid field reversal (as shown in Fig. 4.6), leading to an asymmetry with same spin state, which should be compatible with zero. Fig. 4.7 and Fig. 4.8 show indeed these false asymmetries with χ^2/ndf of 0.78 for the deuteron data and 1.11 for the proton data.

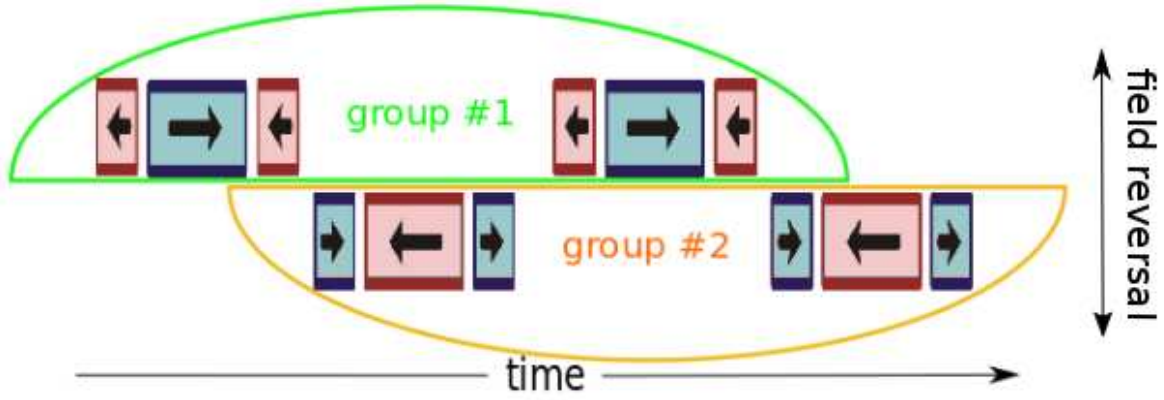

Figure 4.6: Groups for the computation of false asymmetries

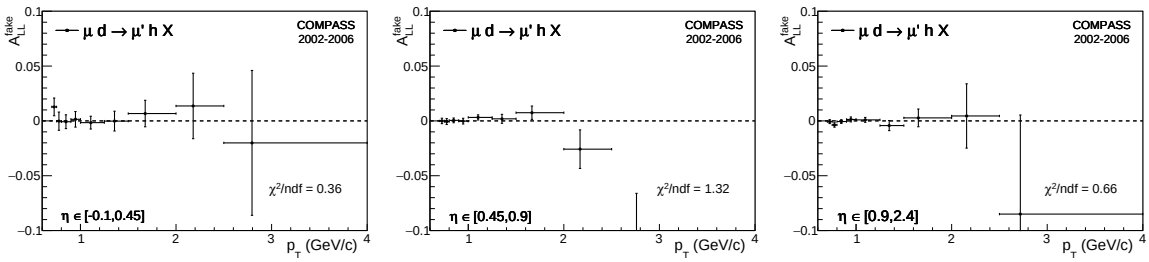

Figure 4.7: Misconfiguration False Asymmetry for all deuteron data for three bins in η_{cms} [-0.1,0.45,0.9,2.4] with a total $\chi^2/ndf = 0.78$

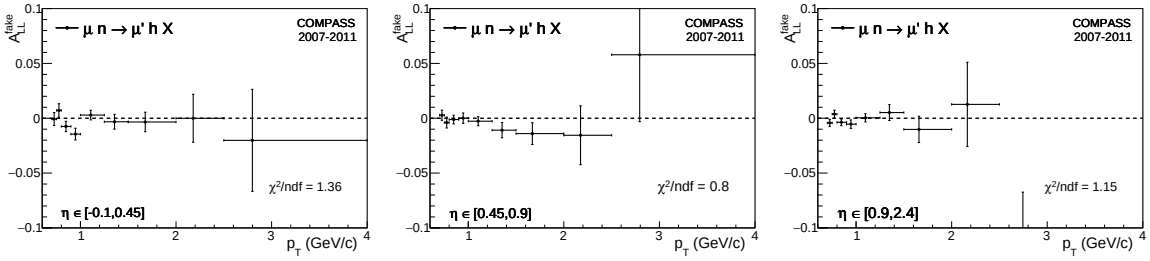

Figure 4.8: Same as Fig. 4.7 for all proton data with a total $\chi^2/ndf = 1.11$

- We did also look at the asymmetries coming from the different microwave settings + and −. The change of frequency of the DNP allows to look at a reproducible false asymmetry A_{rep}^{false} and remove it. It is half the difference between the asymmetry for each configuration + and −. This false asymmetry can let a residual false asymmetry A_{res}^{false} in the final result, which is the fraction of the reproducible false asymmetry which is not cancelled due to unbalanced statistics in the two configurations.

$$A_{res}^{false} = \frac{(\sigma_{A^+}^{stat})^2 - (\sigma_{A^-}^{stat})^2}{(\sigma_{A^+}^{stat})^2 + (\sigma_{A^-}^{stat})^2} \cdot \frac{A^+ - A^-}{2} \tag{4.22}$$

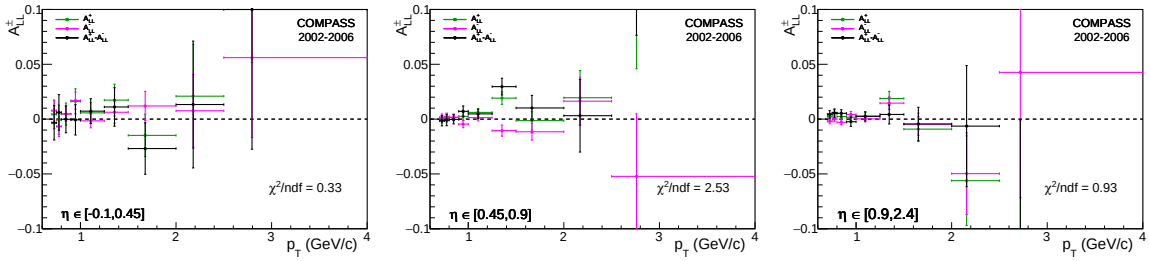

Figure 4.9: Asymmetries $(A_{LL}^{h\ d})^+$,$(A_{LL}^{h\ d})^-$ and their difference for all deuteron data for three bins in η_{cms} [-0.1,0.45,0.9,2.4] with a total $\chi^2 = 1.26$

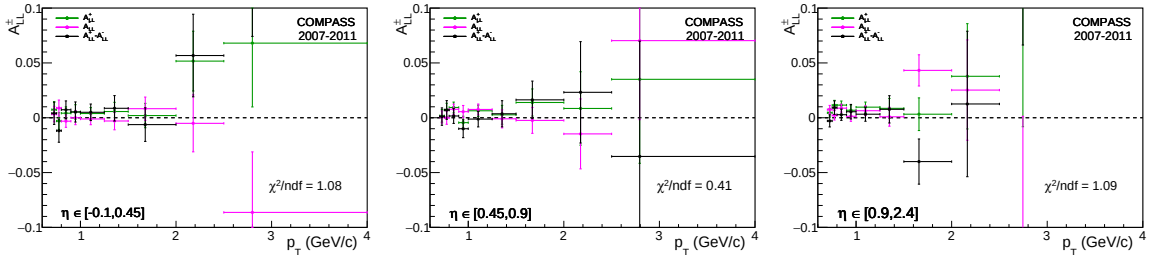

Figure 4.10: Same as Fig. 4.7 for all proton data with a total $\chi^2 = 0.86$

Fig. 4.9 and Fig. 4.10 show that the difference between A^+ and A^- is compatible with zero (at the exception of one point for the second η_h-bin of the deuteron data), and hence that the residual false asymmetry is negligible.

- A lot of asymmetries can also be computed to investigate on the anisotropy of the setup (solenoid field, target or spectrometer).

For the solenoid field part one can compute the asymmetries separately for the magnetic solenoid field in one direction and in the other one. This computation is only possible in a global manner (all data are regrouped together, not by group like in the main analysis) and because of the polarisation reversal with the microwave frequency.
For the target part, one can also compute the asymmetries for opposite parts of the spectrometer: left/right, top/bottom; one can observe some differences between these parts which are mainly due to the magnetic fields, these differences are expected but are not bigger than one σ_{stat} as shown in Fig. 4.11, Fig. 4.12, Fig. 4.13 and Fig. 4.14

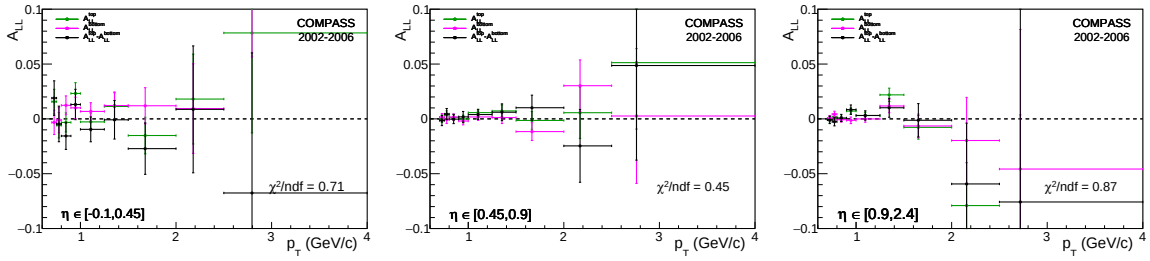

Figure 4.11: Asymmetries $(A_{LL}^{h\ d})^{top}$,$(A_{LL}^{h\ d})^{bottom}$ and their difference for all deuteron data for three bins in η_{cms} [-0.1,0.45,0.9,2.4] with a total $\chi^2 = 0.68$

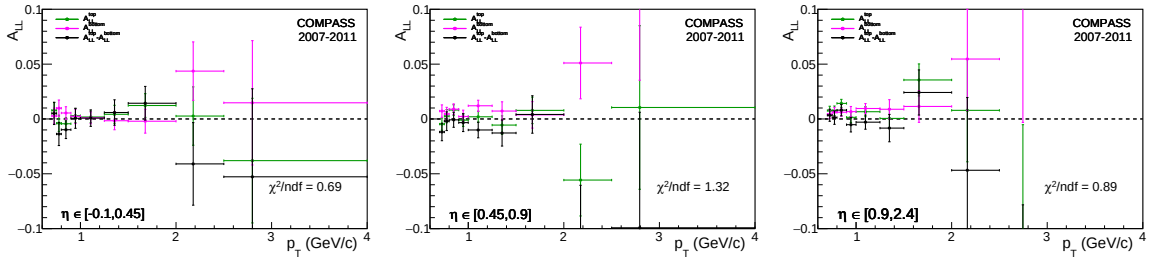

Figure 4.12: Same as Fig. 4.11 for all proton data with a total $\chi^2 = 0.97$

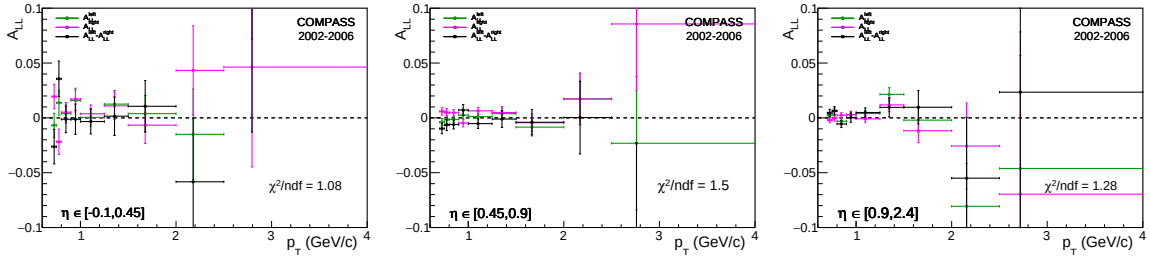

Figure 4.13: Asymmetries $(A_{LL}^{h\ d})^{left}$,$(A_{LL}^{h\ d})^{right}$ and their difference for all deuteron data for three bins in η_{cms} [-0.1,0.45,0.9,2.4] with a total $\chi^2 = 1.29$

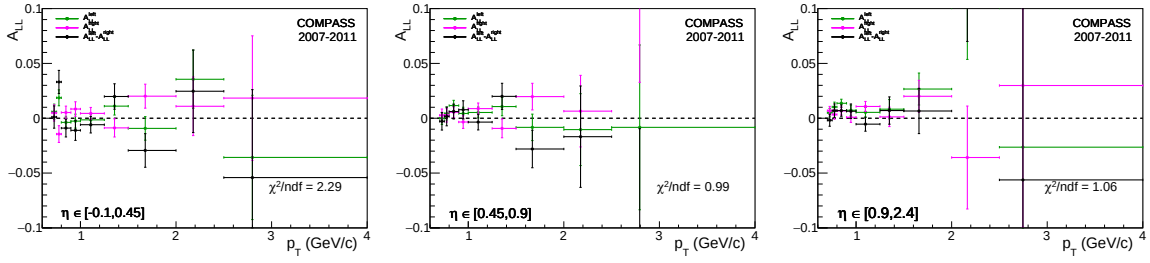

Figure 4.14: Same as Fig. 4.13 for all proton data with a total $\chi^2 = 1.45$

4.3.3 Time Dependent Study of Uncertainties

Since the false asymmetry study presented in the previous section is only qualitative, the systematic uncertainties coming from the false asymmetries are evaluated through a time dependent study, which is presented in this section [83].
The total uncertainty is defined as:

$$(\sigma^2_{tot}) = (\sigma^{syst}_{\Delta r})^2 + (\sigma^{stat}_{\Delta r})^2 \tag{4.23}$$

, and evaluated as:

$$(\sigma^2_{tot}) = (max(\sigma_{\Delta r}, 1) + \delta_{\sigma_{\Delta r}})^2 \tag{4.24}$$

, where Δr is the distribution of the group asymmetries $A_{LL\,i}$ defined in Sec. 4.1.4 centered on the final asymmetry A_{LL} and normalised by the statistical uncertainty. $\sigma_{\Delta r}$ is the width of this distribution and $\delta_{\sigma_{\Delta r}}$ its uncertainty.

$$\Delta r = \frac{A_{LL\,i} - A_{LL}}{\sigma_{A_{LL\,i}}} \tag{4.25}$$

The equations 4.23 and 4.24 can be rearranged to give a maximisation of the fraction of the uncertainty coming from the false asymmetries over its statistical one:

$$\sigma^{syst}_{\Delta r} = \sqrt{(max(\sigma_{\Delta r}, 1) + \delta_{\sigma_{\Delta r}})^2 - 1} \geq \sigma_{A_{false}}/\sigma_{stat} \tag{4.26}$$

This quantity is evaluated for all η_h-bins and p_T-bins, and the results are given in the tables 4.7 depending on the year and also regrouped by target material. An example of these Δr distributions is given in figure 4.15 for all deuteron data, only for the second η_h-bin.

$\eta_h \in [-0.1, 0.45]$

	[0.7,0.75]	[0.75,0.8]	[0.8,0.9]	[0.9,1.0]	[1.0,1.25]	[1.25,1.5]	[1.5,2.0]	[2.0,2.5]	[2.5,4.0]
2006	0.5	0.62	0.52	0.65	0.71	0.44	0.58	0.48	0.47
2007	0.52	0.55	0.68	0.54	0.55	1.05	0.54	0.59	1.21
2011	0.42	0.89	0.48	0.81	0.45	0.69	0.65	1.13	0.69
NH3	0.39	0.65	0.56	0.55	0.41	0.8	0.43	0.89	0.85

$\eta_h \in [0.45, 0.9]$

	[0.7,0.75]	[0.75,0.8]	[0.8,0.9]	[0.9,1.0]	[1.0,1.25]	[1.25,1.5]	[1.5,2.0]	[2.0,2.5]	[2.5,4.0]
2002	1.12	0.69	0.6	0.77	0.9	0.47	0.5	0.69	0.46
2003	0.44	0.49	0.5	0.44	0.79	0.44	0.46	0.5	0.44
2004	0.39	0.38	0.36	0.6	0.55	0.43	0.52	0.51	0.38
2006	0.49	0.64	0.71	0.71	0.58	0.79	0.52	0.81	0.51
LiD	0.44	0.31	0.31	0.42	0.6	0.31	0.31	0.47	0.31
2007	1.02	0.69	0.51	0.68	0.96	0.57	0.51	0.54	0.69
2011	0.77	0.85	0.82	0.47	0.78	0.73	0.48	0.65	0.47
NH3	0.82	0.78	0.56	0.43	0.78	0.62	0.42	0.62	0.43

$\eta_h \in [0.9, 2.4]$

	[0.7,0.75]	[0.75,0.8]	[0.8,0.9]	[0.9,1.0]	[1.0,1.25]	[1.25,1.5]	[1.5,2.0]	[2.0,2.5]	[2.5,4.0]
2002	0.45	0.55	0.87	0.65	0.8	0.44	0.83	0.43	0.64
2003	0.76	0.49	0.46	0.63	0.44	0.87	0.44	0.99	0.86
2004	0.37	0.41	0.57	0.74	0.51	0.38	0.49	0.5	0.82
2006	1.11	0.82	0.48	0.65	0.52	0.76	0.49	0.52	0.8
LiD	0.31	0.36	0.38	0.57	0.49	0.33	0.31	0.41	0.58
2007	0.54	0.52	1.13	0.59	0.9	0.54	0.69	0.51	0.52
2011	0.55	0.55	0.89	0.69	0.49	0.69	0.69	0.95	0.82
NH3	0.43	0.49	0.96	0.71	0.52	0.62	0.71	0.65	0.45

Table 4.7: Values of $\sigma_{\Delta r}^{syst}$ for every η_h and p_T-bin, for all year and regrouped by target material

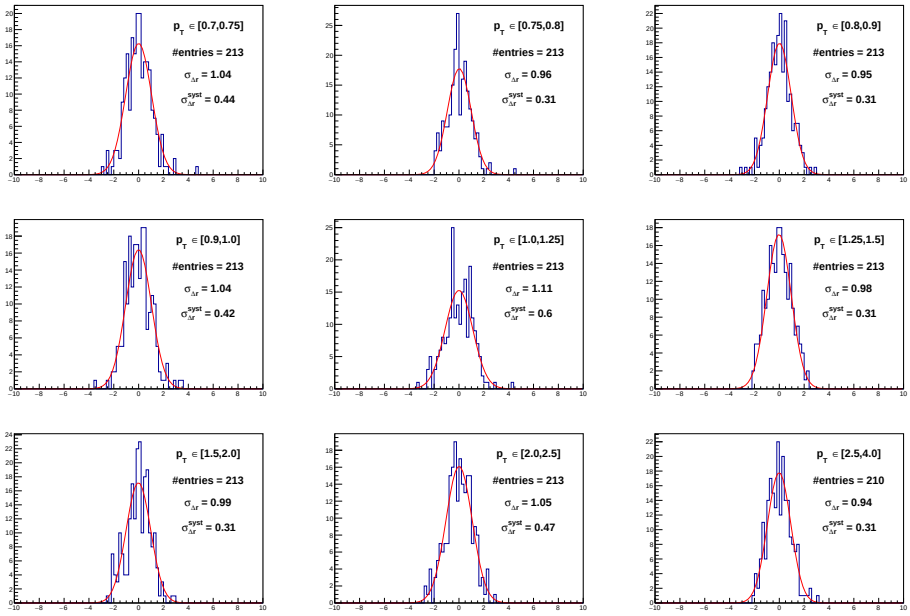

Figure 4.15: Δr distributions for every p_T-bin for the second η_h-bin for all deuteron data

4.3.4 Multiplicative Uncertainties

Apart from the apparatus uncertainties, the asymmetries are affected by systematic uncertainties coming from the variables used in the calculation like P_μ, P_{tar} and f. These variables are related to the asymmetry by the expression:

$$A_{LL} \sim \frac{1}{f P_b P_{cell}} A_{raw} \tag{4.27}$$

The beam polarisation P_b is determined by a Monte-Carlo simulation describing the beam line. This Monte-Carlo simulation has been checked in SMC times with real measurement via a polarimeter when it was present. This comparison leads to the estimation of a relative uncertainty of 5%.

For the target polarisation P_{cell}, the uncertainties of measurement come from the measurement of the temperature equilibrium and the measurements from the NMR coils. One finds a relative uncertainty from 3 to 5%.

Finally the uncertainty on the dilution factor f comes from the uncertainties on the target material and on the total cross-sections.

Using the expression 4.27, all these contributions to the multiplicative uncertainty are added in quadratures:

$$\sigma_{mult} = A_{LL} \sqrt{\left(\frac{\sigma_{P_\mu}}{P_\mu}\right)^2 + \left(\frac{\sigma_{P_{tar}}}{P_{tar}}\right)^2 + \left(\frac{\sigma_f}{f}\right)^2} \tag{4.28}$$

A summary of these multiplicative uncertainties is given in Tab. 4.8.

	2002-2004	2006	2007	2011
σ_{P_μ}/P_μ (%)	5	5	5	5
$\sigma_{P_{tar}}/P_{tar}$ (%)	5	5	2	3.5
σ_f/f (%)	2	3	1	1
σ_{mult}/A_{LL} (%)	7.4	7.6	5.5	6.2

Table 4.8: Summary of uncertainty values for the different multiplicative uncertainty depending on the year

4.3.5 Radiative Corrections

The last part of the systematic study is about the radiative corrections. Until then, one only dealt with one photon exchange inelastic cross-sections. In the actual experiment the incoming muon or the scattered muon can emit Bremsstrahlung photons which change the cross-section. In the figure 4.16 one can see all the cases of radiative corrections: Bremsstrahlung of the incoming muon (also possible for the scattered muon), vertex correction and vacuum polarisation.

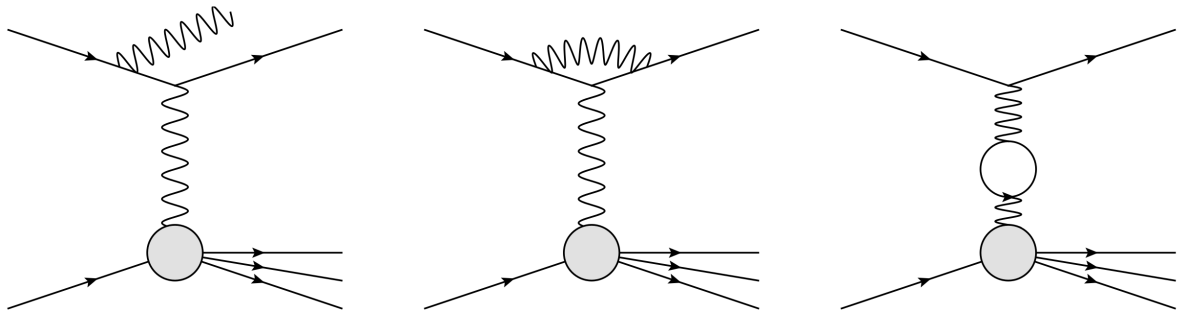

Figure 4.16: From left to right, Feynman diagrams of the radiative processes for the inelastic tail, the vertex correction and the vacuum polarisation

In the asymmetry calculations, some of these effects are already taken into account through the dilution factor f, which is multiplied by a corrective term $\rho(x_{Bj}, y)$ evaluated from precalculated tables obtained with TERAD [84]. Unfortunately these tables are only calculated for a DIS regime ($Q^2 > 1$ GeV^2) and the corrective term was only an extrapolation of the DIS calculation. It has been tried to compute these corrections for the photoproduction regime combining PYTHIA (a Lund Monte-Carlo which can deal with photoproduction) [85] and RADGEN (a Monte Carlo base on TERAD code) [86], but there is no result yet available for COMPASS kinematics.

Fortunately, since the corrective terms are in $O(ln(Q^2/m_\mu^2))$, these corrections are expected to be very small in the photoproduction regime and are not taken into account in this analysis [86].

4.4 Results for unindentified hadrons

4.4.1 Deuteron Asymmetries

In this section all the asymmetries for the deuteron target (2002-2006) are presented for every year and then regrouped with a weight taking into account their statistics. They are also shown for three different hadron yields: all hadrons h in Fig. 4.17 and Fig. 4.20, positive hadrons h^+ in Fig. 4.18 and Fig. 4.21, and negative hadrons h^- in Fig. 4.19 and Fig. 4.22.

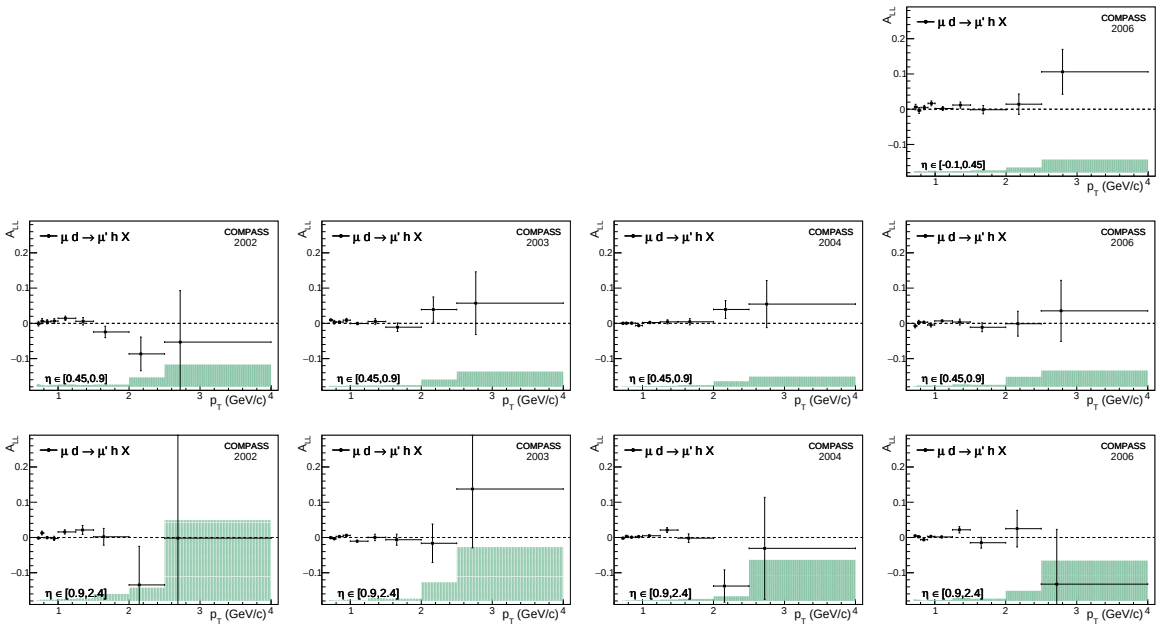

Figure 4.17: Asymmetry A_{LL}^{dh} year by year (2002-2006) (from left to right) for three bins in η_{cms} [-0.1,0.45,0.9,2.4] (from top to bottom)

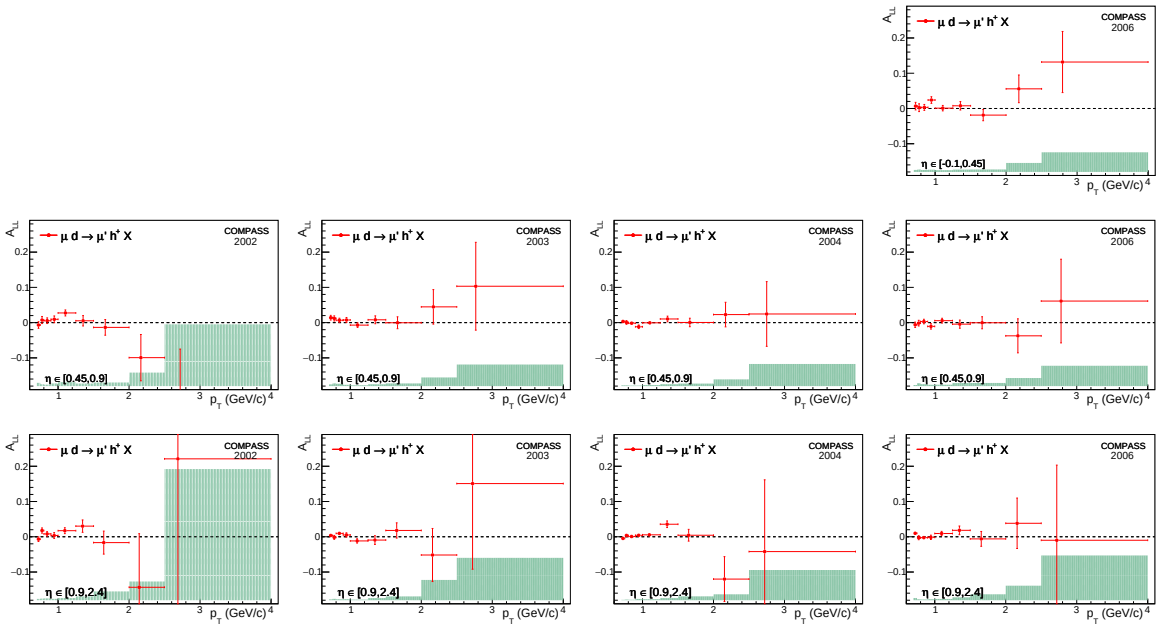

Figure 4.18: Asymmetry $A_{LL}^{dh^+}$ year by year (2002-2006) (from left to right) for three bins in η_{cms} [-0.1,0.45,0.9,2.4] (from top to bottom)

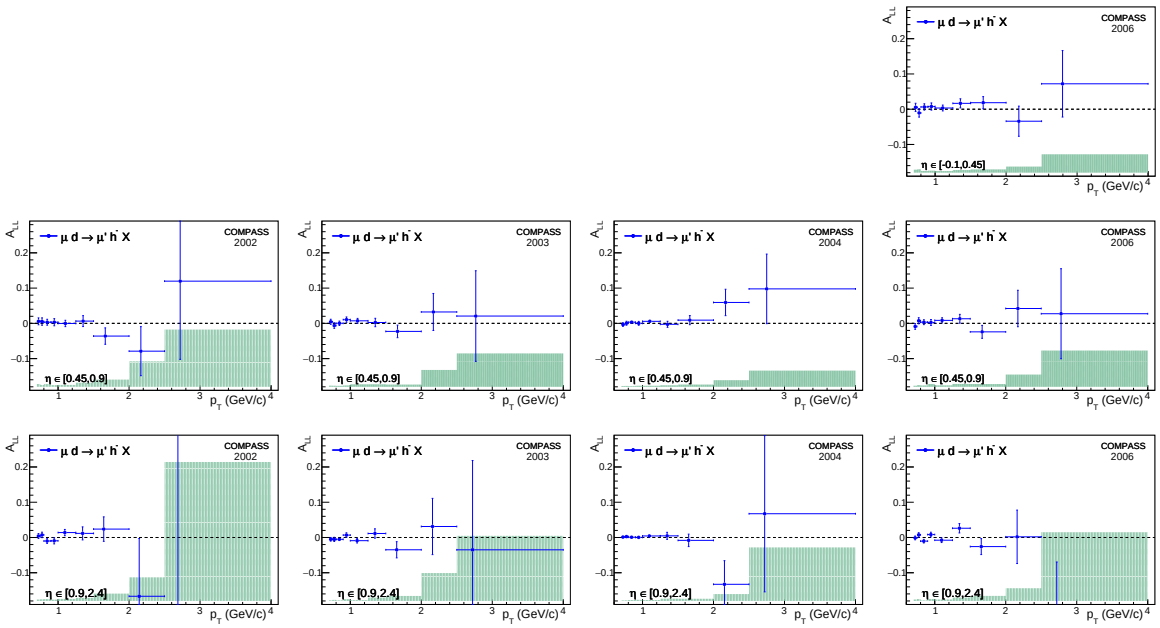

Figure 4.19: Asymmetry $A_{LL}^{dh^-}$ year by year (2002-2006) (from left to right) for three bins in η_{cms} [-0.1,0.45,0.9,2.4] (from top to bottom)

The results show asymmetries compatible with zero within statistical and systematic uncertainties. The compatibility χ^2/ndf of each years compared to the final (average with statistical weight) deuteron asymmetries are given in Tab. 4.9 The values for each years are underestimated since it does not take into account the fact that the asymmetry of the year influences of the final asymmetry in the number of degree of freedom, whereas the total value takes this into account. The values remain inferior or close to 1, showing a good compatibility of these data taken with different setups.

years	2002	2003	2004	2006	total
h	0.805	0.904	0.395	0.410	1.257
h^+	0.973	1.026	0.402	0.495	1.448
h^-	0.508	0.368	0.385	0.342	0.801

Table 4.9: Compatibility χ^2/ndf between the different years for the asymmetries taken with a deuteron target. The values are presented divided by their number of degree of freedom: 18 for 2002-2004 and 27 for 2006 and 54 (=3*18+27-27 (for the averaged values)) for the total

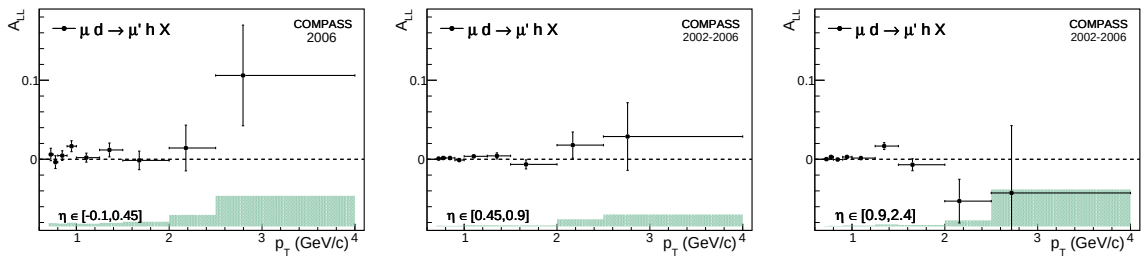

Figure 4.20: Asymmetry A_{LL}^{dh} for all deuteron data for three bins in η_{cms} [-0.1,0.45,0.9,2.4]

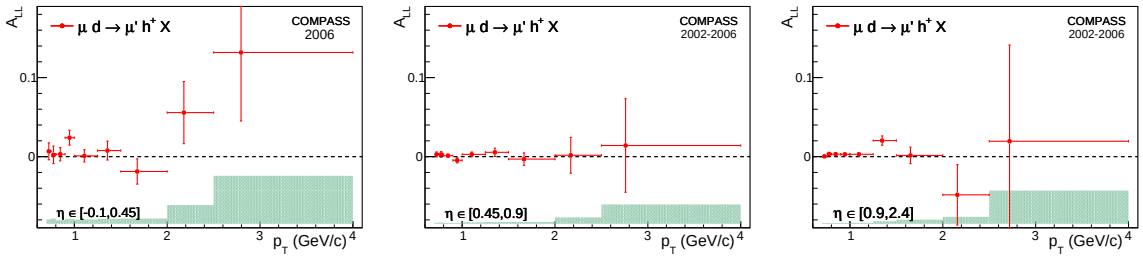

Figure 4.21: Asymmetry $A_{LL}^{dh^+}$ for all deuteron data for three bins in η_{cms} [-0.1,0.45,0.9,2.4]

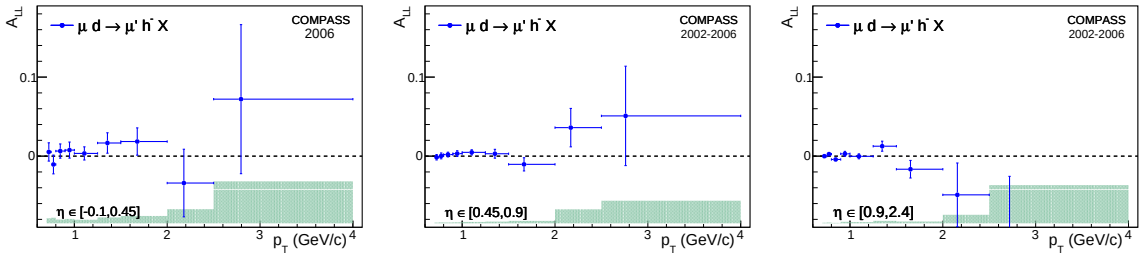

Figure 4.22: Asymmetry $A_{LL}^{dh^-}$ for all deuteron data for three bins in η_{cms} [-0.1,0.45,0.9,2.4]

The physical interpretation of these results is only performed via a comparison with theoretical calculations in Sec. 5.2.

4.4.2 Proton Asymmetries

As in the previous section, the asymmetries are presented for the proton target (2007 and 2011) for three different yields: all hadrons h in Fig. 4.23 and Fig. 4.26, positive hadrons h^+ in Fig. 4.24 and Fig. 4.27, and negative hadrons h^+ in Fig. 4.25 and Fig. 4.28.

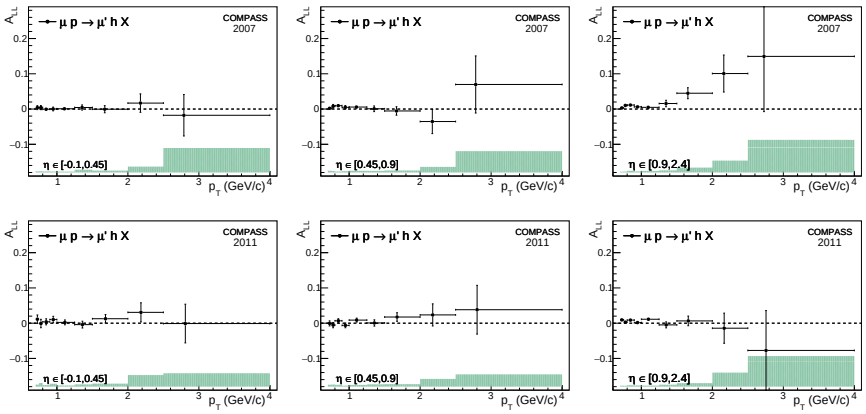

Figure 4.23: Asymmetry A_{LL}^{ph} year by year (2007 and 2011) (from top to bottom) for three bins in η_{cms} [-0.1,0.45,0.9,2.4] (from left to right)

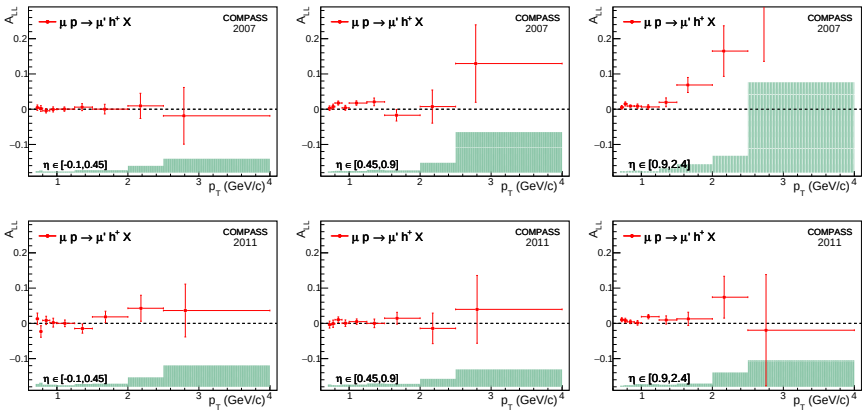

Figure 4.24: Asymmetry $A_{LL}^{p\,h^+}$ year by year (2007 and 2011) (from top to bottom) for three bins in η_{cms} [-0.1,0.45,0.9,2.4] (from left to right)

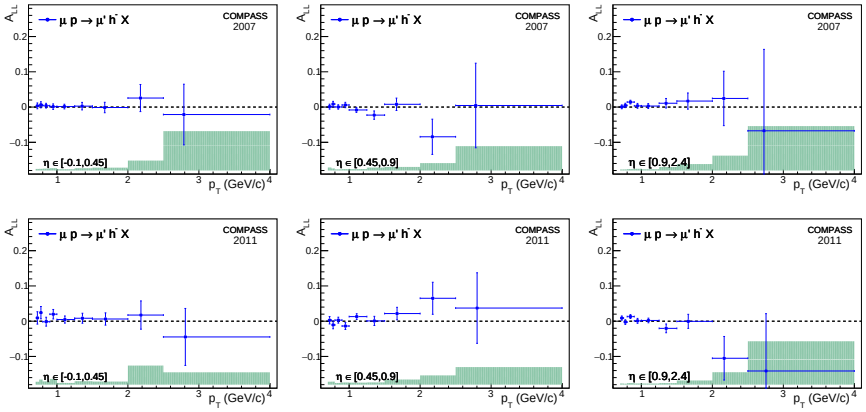

Figure 4.25: Asymmetry $A_{LL}^{p\,h^-}$ year by year (2007 and 2011) (from top to bottom) for three bins in η_{cms} [-0.1,0.45,0.9,2.4] (from left to right)

As for the asymmetries for deuteron target, the compatibility χ^2/ndf presented in Tab. 4.10 shows a good compatibility between the asymmetries for the proton target, even though the beam energy was moved from 160 GeV to 200 GeV. As for the deuteron asymmetries, the values χ^2/ndf for each year are underestimated.

years	2007	2011	total
h	0.458	0.487	0.945
h^+	0.401	0.492	0.893
h^-	0.422	0.518	0.940

Table 4.10: Compatibility χ^2/ndf between the different years for the asymmetries taken with a proton target. The values are presented divided by their number of degree of freedom: 27 for 2007 and 2011 and also 27 (2*27-27) the total

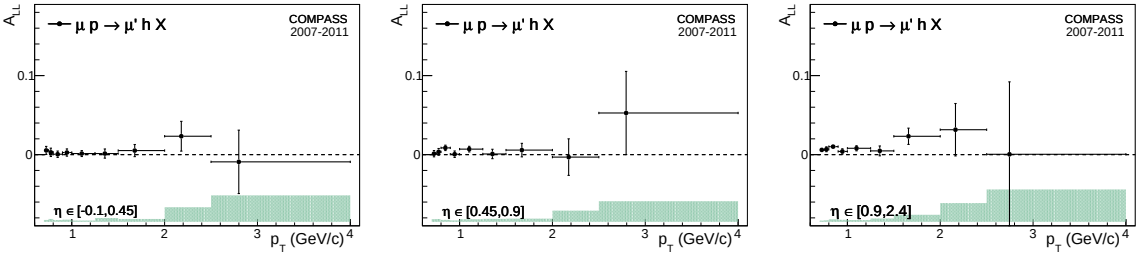

Figure 4.26: Asymmetry A_{LL}^{ph} for all proton data for three bins in η_{cms} [-0.1,0.45,0.9,2.4]

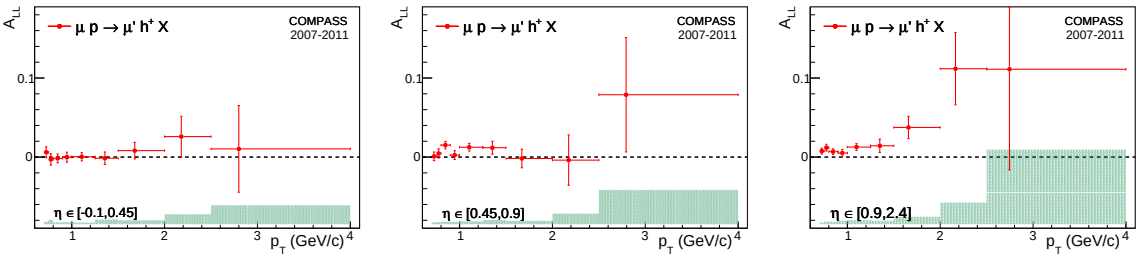

Figure 4.27: Asymmetry $A_{LL}^{ph^+}$ for all proton data for three bins in η_{cms} [-0.1,0.45,0.9,2.4]

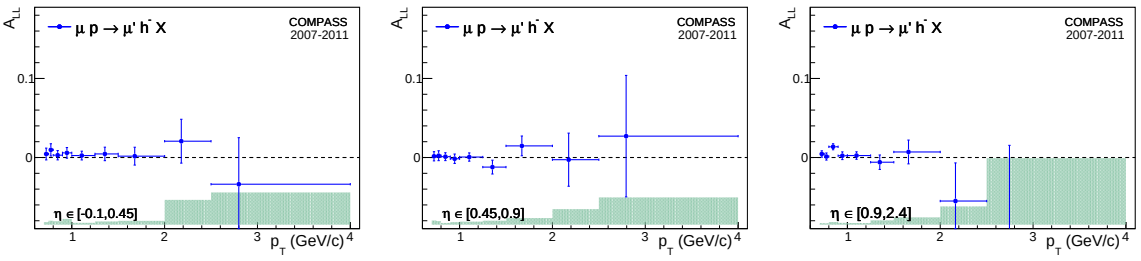

Figure 4.28: Asymmetry $A_{LL}^{ph^-}$ for all proton data for three bins in η_{cms} [-0.1,0.45,0.9,2.4]

4.5 Asymmetries for identified hadrons

To extract more information from the data, we also chose to go further in the separation of hadron flavor and looked at the asymmetries for (positive and negative) pions and (positive and negative) kaons in the final state.

The hadron identification is performed using the information from the RICH detector which is presented in Sec. 2.4. The particle identification in the analysis is done in two steps:

- The particles are identified using likelihood estimators.
- Each particle is given a weight to take into account the possible misindentification in a certain kinematic domain.

For this, one needs to extract the RICH performances and also to study the response to different likelihood tunings. This study is inspired of [87].

4.5.1 RICH Likelihoods

The primary particle identification is performed via an extended likelihood estimator [88] for different hypotheses of mass (m_e, m_μ, m_π, m_k and m_p) and also for the background (bg). The likelihood function can be expressed as:

$$LH(m) = exp(-S_m - B) \prod_{j=1}^{N} (s_m(\theta_j, \phi_j) + b) \tag{4.29}$$

,where N is the number of photons used to reconstruct the Cherenkov angle θ, s_m the probability for the j-photon to belong to the signal, and b the one to belong to the background. The s_m probability takes into account the expected number of photons at the angle Θ_m (Cherenkov angle expected for a particle of mass m), the resolution of the photon detectors and the probability to reach these detectors. b is taken through real data [59].

Knowing all these likelihoods, one first choose the particle corresponding to the maximum of these likelihoods. Then this likelihood is compared especially to the second maximum likelihood and to the background likelihood, but also to all the other likelihoods. These comparisons are done with certain threshold which are chosen through a special study shortly presented in Sec. 4.5.3, called likelihood tuning.

4.5.2 RICH Detector Performances

In order to be able to weight each particle identified through the likelihood identification, one first has to talk about the determination of the rich performances: identification or misidentification probability. This probability of identification (resp. misidentification) is expressed as the number of particle correctly (resp. wrongly) identified out of a 'pure' sample of known hadrons over the total number of particles of this sample.

$$P(t \to i) = \frac{N(t \to i)}{N(t)} \tag{4.30}$$

Through the Eq. 4.30, one can define the (mis-)idenfication probability $P(t \to i)$ as the particle of type t is identified as a particle of type i. In the case of the idenfication $i = t$. These quantities are pure detector properties and can be presented as a matrix where the diagonal terms are the identification probabilities and the other are the misidentification ones Eq. 4.31.

$$M_R = \begin{pmatrix} P(\pi \to \pi) & P(K \to \pi) & P(p \to \pi) \\ P(\pi \to K) & P(K \to K) & P(p \to K) \\ P(\pi \to p) & P(K \to p) & P(p \to p) \\ P(\pi \to X) & P(K \to X) & P(p \to X) \end{pmatrix} \tag{4.31}$$

These matrix are calculated independently for negative and positive particles since the detector performances are different for each charge (mostly because of the different direction of the momentum). In the presentation of this method, the sign will be then omitted.

This determination of these probability is done through the 'pure' samples coming from ϕ_{1020}, K^0_S and Λ, whose branching ratios are summarized in Tab. 4.11

ϕ_{1020}		K^0_L		K^0_S		Λ	
K^+K^-	48.9%	$\pi^\pm e^\mp \nu_e$	40.6%	$\pi^+\pi^-$	69.2%	$p\pi^-$	63.9%
$K^0_L K^0_S$	34.2%	$\pi^\pm \mu^\mp \nu_\mu$	27.0%	$\pi^0\pi^0$	30.7%	$n\pi^0$	35.8%
$\rho\pi^+\pi^+\pi^-\pi^0$	15.3%	$3\pi^0$	19.5%				
		$\pi^+\pi^-\pi^0$	12.5%				

Table 4.11: Decay modes for ϕ_{1020}, K^0 and Λ [89]

To manage to get a really 'pure' sample, these samples follow a selection criteria of their own. These samples undergo a spill selection comparable to the one used in asymmetry, as well as a choice of a best primary vertex. It is also required to have two outgoing particles of opposite charge. Some cuts are also necessary on the track momentum ($10 < p < 50$ GeV/c) to avoid Cherenkov threshold for pions (lower cut) and Cherenkov saturation effects (upper cut). The incident track angle is also limited to 0.4 rad to eliminate particles outside of RICH acceptance. Finally for the years later than 2006 (included), the RICH pipes in the center of the detector ($r_{pipes} = 5cm$) degrade its performance and this zone is removed from the analysis. The following selections are different for all the decay samples:

- for the strong decay of ϕ_{1020} one requires an exclusive reaction and a cut on the missing mass (M_{miss}): $(M^2_{miss} - M^2_p)/(2M_p) < 2.5$ GeV/c^2. This decay gives a very pure kaon sample.

- for the weak decays of K^0_S and Λ, one requires a secondary vertex far enough from the primary vertex with a direction of the outgoing particle collinear enough to the potential K^0_S or Λ. A last cut is done on the invariant mass value to separate the K^0_S or Λ samples ($|M_{inv}| < 10$ MeV/c^2).

Once these samples are determined, the identification probability can be estimated [90]. One only presents this method for the positive pions since it is the same for all samples. One first requires that the spectator of opposite charge is well identified by the RICH [91], for π^+ the spectator in the K^0_S decay is of course π^-. This gives us a subsample $K^0_S(\pi^-)$ of hadrons in the K^0_S sample. Then one looks at what particle Y^+ is identified by the RICH, which gives us for each the subsample $K^0_S(\pi^- Y^+)$ of hadrons. For the last misidentification probability $Y^+ = X^+$ (same X as in Eq. 4.31), Y^+ includes all particle that weren't identify by the RICH.

For these subsamples, one simultaneously fits the K^0_S invariant mass distributions with functions described in Tab. **??** to extract the signal and the background. For each subsample, one can then extract the number $N_{K^0_S}(\pi^-)$ or $N_{K^0_S}(\pi^- Y^+)$ of hadrons corresponding to the signal of the invariant mass distributions. In the simultaneous fit, a certain constraint was added to ensure that $N_{K^0_S}(\pi^-) = \sum_{Y^+} N_{K^0_S}(\pi^- Y^+)$ for $Y^+ = (\pi^+, K^+, p, X^+)$.

With these quantities, one can finally extract the following (mis-)identification probabilities:

$$P(\pi^+ \to Y^+) = \frac{N(\pi^+ \to Y^+)}{N(\pi^+)} = \frac{N_{K^0_S}(\pi^- Y^+)}{N_{K^0_S}(\pi^-)} \tag{4.32}$$

	Background	Signal
ϕ_{1020}	$(x - 2m_K)^n exp(-a_1(x - 2m_K))$	Gaussian$\otimes$ relativistic Breit-Wigner [92]
K^0_S	2^{nd} degree Chebyshev polynomial	Two Gaussians
Λ	$(x - (m_p + m_\pi))^n exp(-a_1(x - (m_p + m_\pi))$	Two Gaussians

Through the (mis-)identification matrix, one can relate the number of identified hadrons ($\vec{I_Y}$) with the true number of hadrons ($\vec{T_Y}$) by a system of equations:

$$\begin{pmatrix} I_\pi \\ I_K \\ I_p \\ I_X \end{pmatrix} = \begin{pmatrix} P(\pi \to \pi) & P(K \to \pi) & P(p \to \pi) \\ P(\pi \to K) & P(K \to K) & P(p \to K) \\ P(\pi \to p) & P(K \to p) & P(p \to p) \\ P(\pi \to X) & P(K \to X) & P(p \to X) \end{pmatrix} \begin{pmatrix} T_\pi \\ T_K \\ T_p \end{pmatrix} \tag{4.33}$$

The results of the 2006 analysis are shown in Fig. 4.29 and Fig. 4.30.

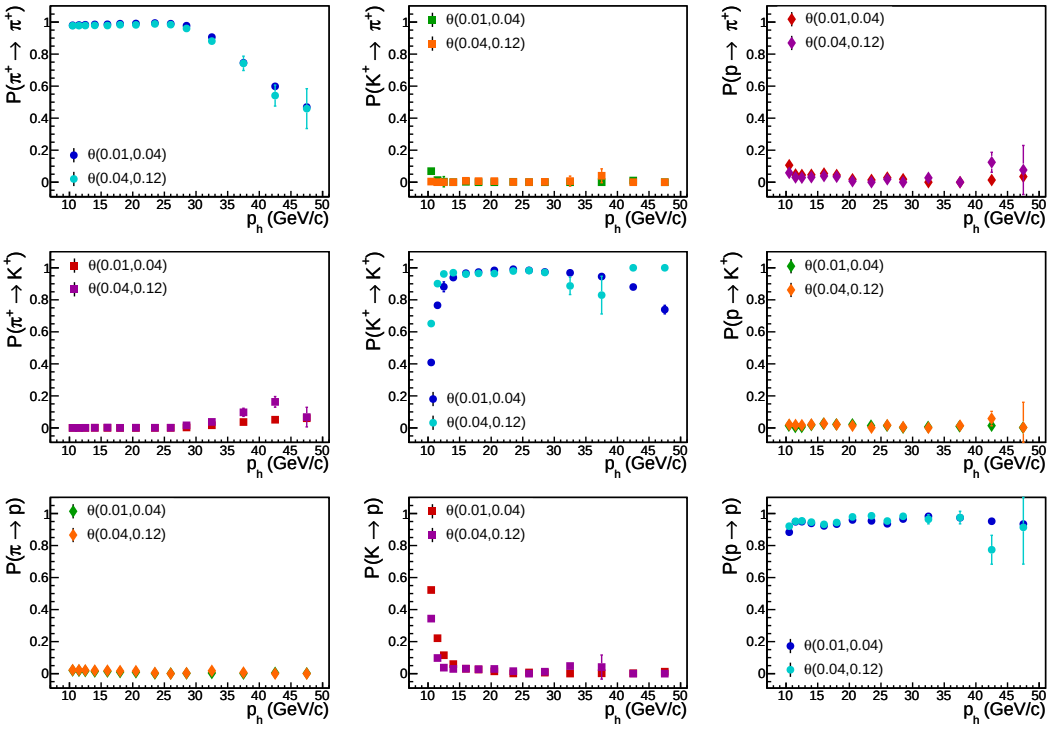

Figure 4.29: Hadron efficiency for 2006 data for positive particles

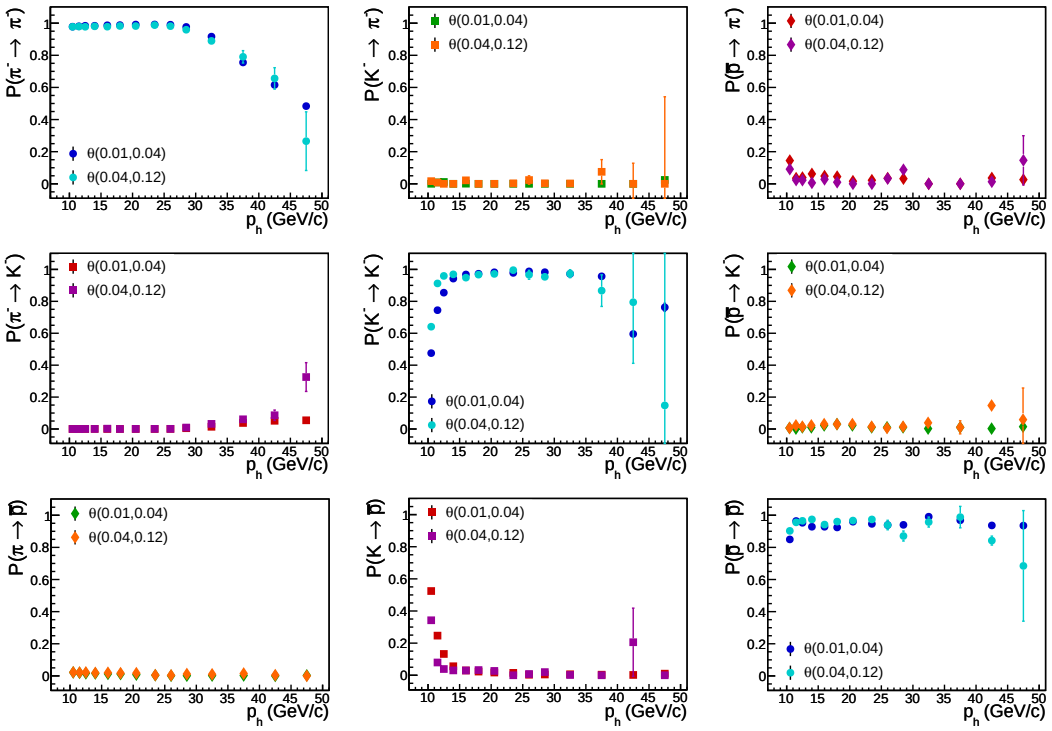

Figure 4.30: Hadron efficiency for 2006 data for negative particles

4.5.3 Likelihood Tunings

From the efficiency (probability of (mis-)identification) matrix, one also defines another quantity, the purity, as the probability that a particle which is identified as a type i is truly of type t:

$$Q(t \to i) = \frac{T_t}{I_i} P(t \to i) \quad i,t = (\pi, K, p) \tag{4.34}$$

This quantity depends on the efficiency but also on the hadron rates. Since the hadron sample is largely dominated by pions, one gets $I_\pi/I_K \sim 7$ and $I_\pi/I_p \sim 20$, hence the kaon and proton samples are impacted by a large contamination of pions.

One can then study the impact of the likelihood cuts on these properties and choose wisely the optimal cuts. This process is called likelihood tuning.

To perform this tuning, several Figures of Merit (FoM) can be used:

- $FoM_1 = purity * efficiency$
- $FoM_2 = purity * N_{id}/N_{all}$

These FoM are taken for different cuts of $LH_{max}/LH_{2^{nd}\,max}$, LH_{max}/LH_{bg}, and for different values of $p_{h\,min}$. One then tries to maximize these FoM and the results are summarised in Tab. 4.12 (the results are different for 2002-2004 and 2006-2007 since the RICH has been upgraded in 2006). The domain chosen for p_h was [10,50] GeV/c to have a roughly good efficiency, especially for the kaon identification.

pion	kaon	proton
	$LH_K > 1.02 * LH_\pi$ for 2002-2004	$LH_p > LH_\pi$
	$LH_K > 1.08 * LH_\pi$ for 2006-2011	
$LH_\pi > LH_K$		$LH_p > LH_K$
$LH_\pi > LH_p$	$LH_K > LH_p$	
$LH_\pi > LH_{bg}$	$LH_K > 1.24 * LH_{bg}$	$LH_p > LH_{bg,e,\mu}$

Table 4.12: Likelihood cuts

4.5.4 Efficiency Corrections

After the primary identification presented in Sec. 4.5.1, one then needs to take into account the possible contamination of the number hadrons by the other hadrons. This can be done using the efficiency matrix defined in Sec. 4.5.2 and taking its inverse. Naturally, one needs a square matrix for this purpose. There are two ways to do this:

- one can add a column (0,0,0,1) representing the fact that the true particle of the background come only from the unidentified particles.
- one can also skip the last line of the efficiency matrix without impacting much the inverse matrix since the matrix elements of this line are close to zero.

For the post 2006 (included) analysis, the proton identification was done so one chose the first method (adding a column). Whereas for the pre 2006 analysis, only pions and kaons were identified without any information on the particle that weren't identified, so one chose to skip the last line. This gives us for 2006-2011:

$$\begin{pmatrix} T_\pi \\ T_K \\ T_p \\ T_X \end{pmatrix} = \begin{pmatrix} P(\pi \to \pi) & P(K \to \pi) & P(p \to \pi) & 0 \\ P(\pi \to K) & P(K \to K) & P(p \to K) & 0 \\ P(\pi \to p) & P(K \to p) & P(p \to p) & 0 \\ P(\pi \to X) & P(K \to X) & P(p \to X) & 1 \end{pmatrix}^{-1} \begin{pmatrix} I_\pi \\ I_K \\ I_p \\ I_X \end{pmatrix} \tag{4.35}$$

, and for 2002-2004:

$$\begin{pmatrix} T_\pi \\ T_K \end{pmatrix} = \begin{pmatrix} P(\pi \to \pi) & P(K \to \pi) \\ P(\pi \to K) & P(K \to K) \end{pmatrix}^{-1} \begin{pmatrix} I_\pi \\ I_K \end{pmatrix} \tag{4.36}$$

Since these matrix are calculated for a binning in $\theta_{h,RICH}$ and p_h, it is more accurate to compute the true number of hadrons on a hadron by hadron basis. For instance, a hadron identified as a pion is treated like 0.9 of a pion, 0.08 of a kaon and 0.02 of a proton. With this true number of pions and kaons free of all contamination, one can then compute the asymmetries as explained in Sec. 4.1.

4.5.5 Results of Identified Asymmetries

In this section are presented the results for the asymmetries with identified hadrons, this gives us eight different asymmetries: two different kind of target material (deuteron and proton) and four different kind of outgoing hadrons (π^+, π^-, K^+, K^-); each of these asymmetries is presented for three bins of η_h and five bins of p_T.

The statistics are further reduced compared to unidentified hadrons since the unfolding requires $p_h \in [10, 50]$ (GeV/c). Due to this requirement, the last point $\eta_h \in [0.9, 2.4]$ and $p_T \in [2.5, 4.0]$ (GeV/c) does not get any statistics and is thus removed.

For each pion (Fig. 4.31 and Fig. 4.32) or kaon (Fig. 4.33 and Fig. 4.34) asymmetry, the corresponding asymmetry for unidentified hadron is presented in black (shifted of 0.01 or 0.03 in the x axis) to be able to compare them. One can see that due to these changes of kinematics, the pion asymmetries, which should look like the hadron ones, are actually a little different.

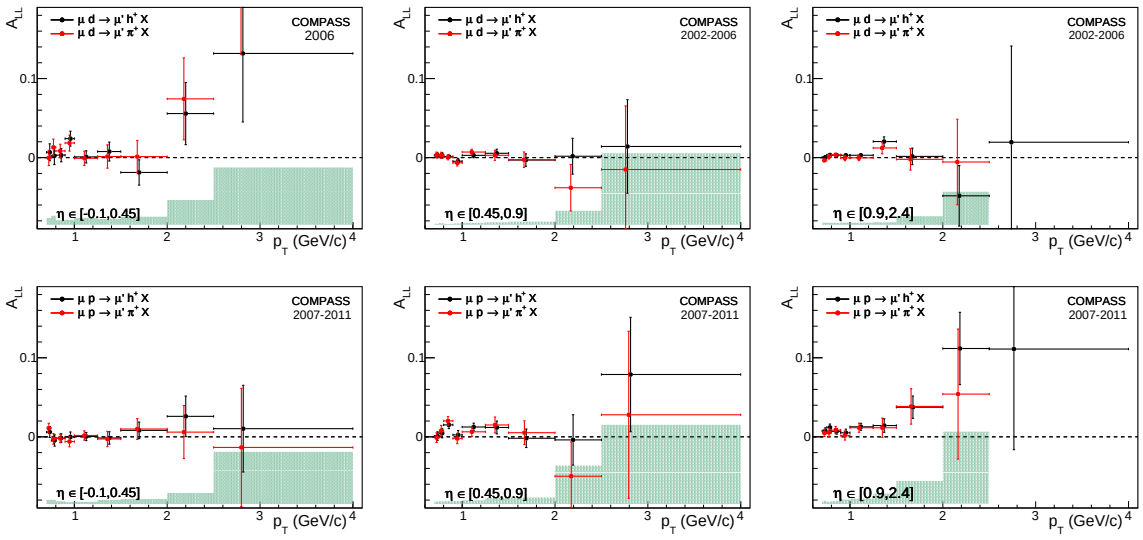

Figure 4.31: Asymmetry $A_{LL}^{\pi^+}$ in red for all deuteron (top) and proton (bottom) data for three bins in η_{cms} [-0.1,0.45,0.9,2.4] with $A_{LL}^{h^+}$ in black

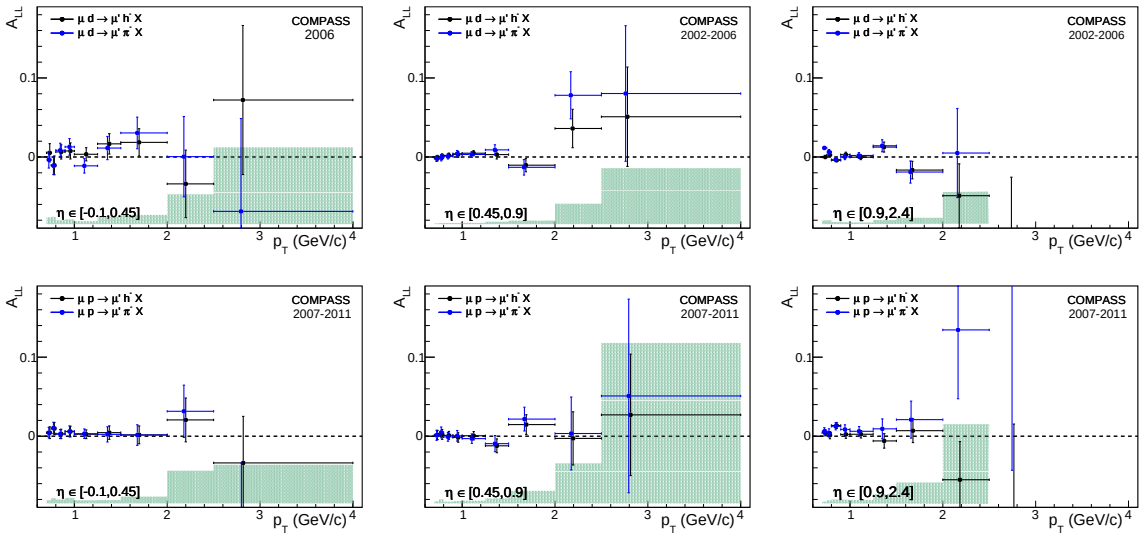

Figure 4.32: Asymmetry $A_{LL}^{\pi^-}$ in blue for all deuteron (top) and proton (bottom) data for three bins in η_{cms} [-0.1,0.45,0.9,2.4] with $A_{LL}^{h^-}$ in black

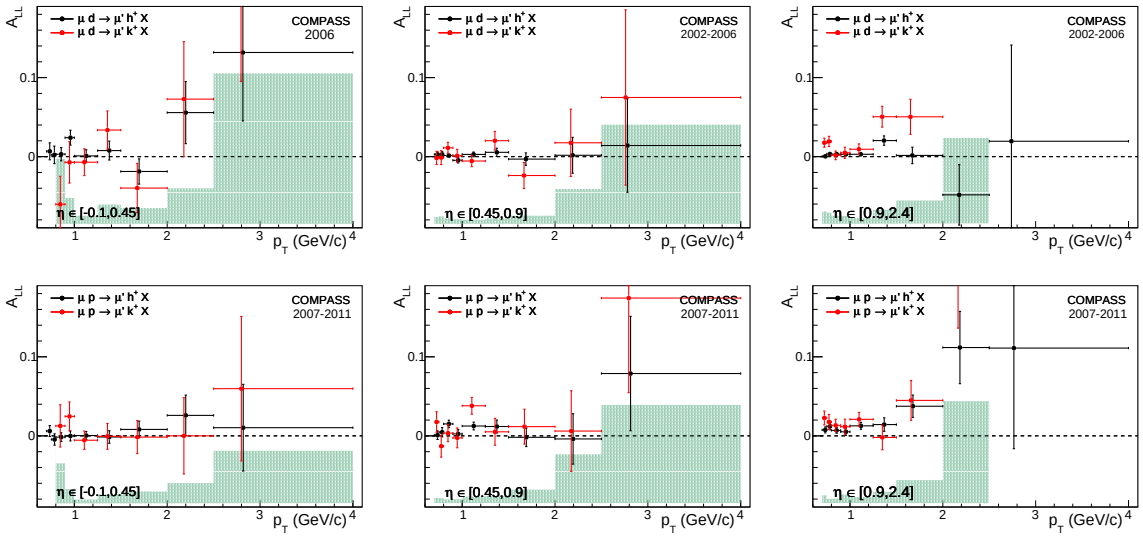

Figure 4.33: Asymmetry $A_{LL}^{k^+}$ in red for all deuteron (top) and proton (bottom) data for three bins in η_{cms} [-0.1,0.45,0.9,2.4] with $A_{LL}^{h^+}$ in black

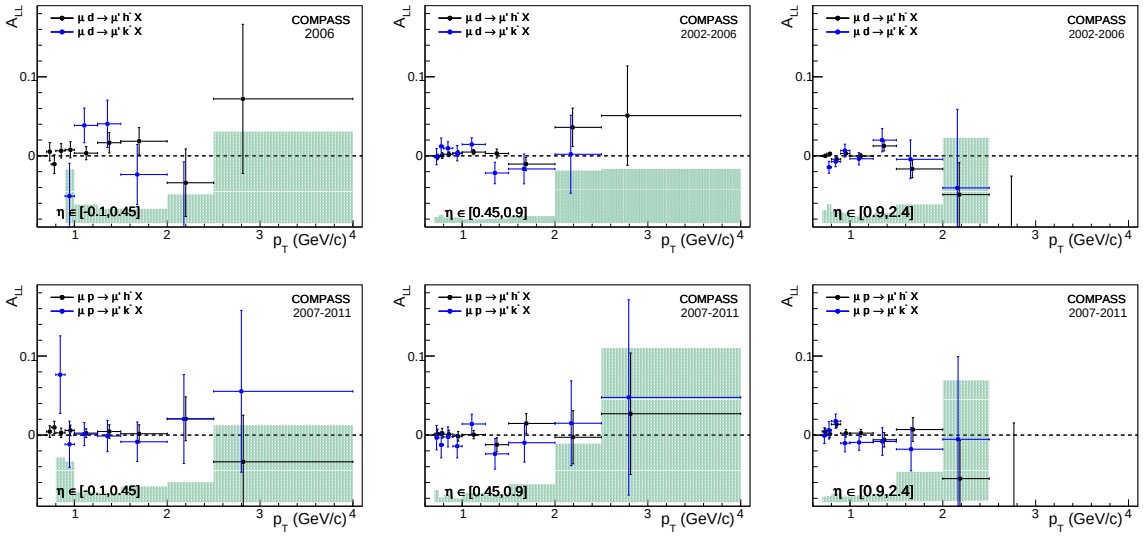

Figure 4.34: Asymmetry $A_{LL}^{k^-}$ in blue for all deuteron (top) and proton (bottom) data for three bins in η_{cms} [-0.1,0.45,0.9,2.4] with $A_{LL}^{h^-}$ in black

All these results can give cleaner data to compare to theoretical calculations and bring new information via the kaon asymmetries. Unfortunately since the statistics of these samples are more restrained and also since the cross-check of this analysis is not yet performed, these asymmetries have not yet been compared to theoretical calculations and will not be presented in the next chapter which only deals with unidentified asymmetries.

Chapter 5

Comparison between Experimental and Theoretical Asymmetries

The ultimate goal of this analysis was to be able to perform a fit of a new PDFs parameterisation with data including the asymmetries showed in Sec. 4.4. Unfortunately, as one will see in Sec. 5.6, the last part of this analysis was not yet possible due to the progress of theoretical calculations. So to be able to interpret the results of these asymmetries in terms of gluon polarisation, the only choice left is to compare them with the current theoretical calculations using inputs from the global fits already published.

The detail of how to calculate the theoretical asymmetries has been given in Sec. 1.2. Compared to the inputs used in [4], we decided to update the following inputs in the theoretical calculations in order to get the best possible comparison with our data:

The unpolarised PDFs

The different sets studied are CTEQ65 [34], MTSW08 [93] and NNPDF [94]. These distributions do not impact too much the calculation of the asymmetries, so they will not be discussed in detail. Nevertheless one can note that NNPDF, which does not use SIDIS data to avoid a bias coming from the FFs, gives a slightly different result for the unpolarized nucleon structure.

The polarised PDFs

We will use DSSV14 [95], the former version of the same group DSSV08 [19], GRSV (standard and extreme cases) [38], LSS (two versions: one with a positive Δg distribution $LSS10_+$ and one with change of sign $LSS10_0$) [24] or polNNPDF [96]. These distributions differ quite a lot from the previous ones, however they are more up to date and are based on QCD fits using a lot more world data, as summarised in Tab. 5.1. For the extreme cases of GRSV ($GRSV_{min}$, $GRSV_{max}$), the polarised gluon distributions are identified with the unpolarised one (with a factor -1 for $GRSV_{min}$) at a reference scale μ_0 and evolved at a μ scale following the DGLAP [15] evolution equations, as first introduced in Sec. 1.2.5.

PDF	DIS	SIDIS	RHIC
DSSV	✓	✓	✓
LSS 2010	✓	✓	×
NNPDFpol 2013	✓	×	✓
GRSV 2001	✓	✓	×

Table 5.1: Types of data used in the analysis of polarised PDFs

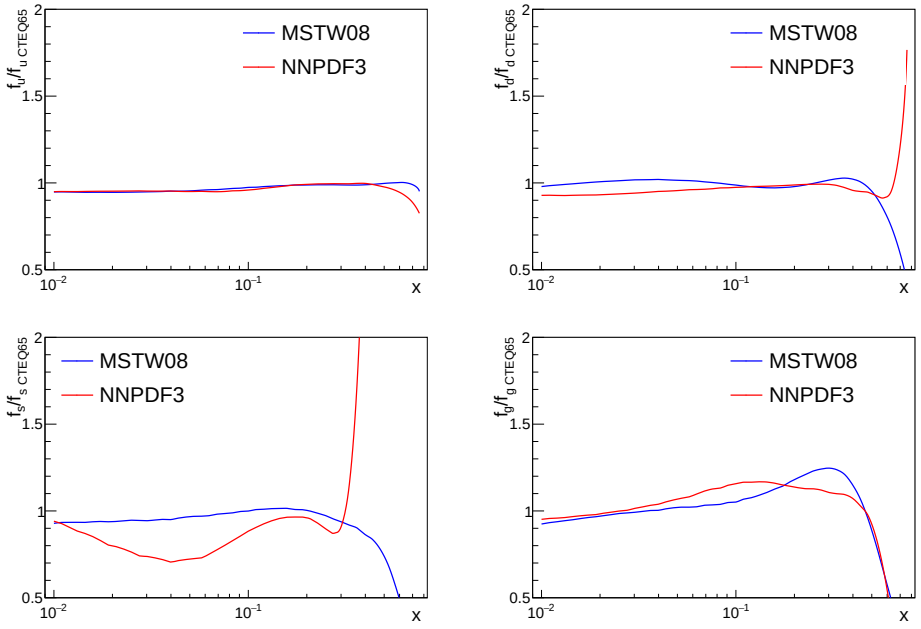

Figure 5.1: Ratio of unpolarized PDFs from the global fits MSTW08 and NNPDF over CTEQ65 for u, d, s and g

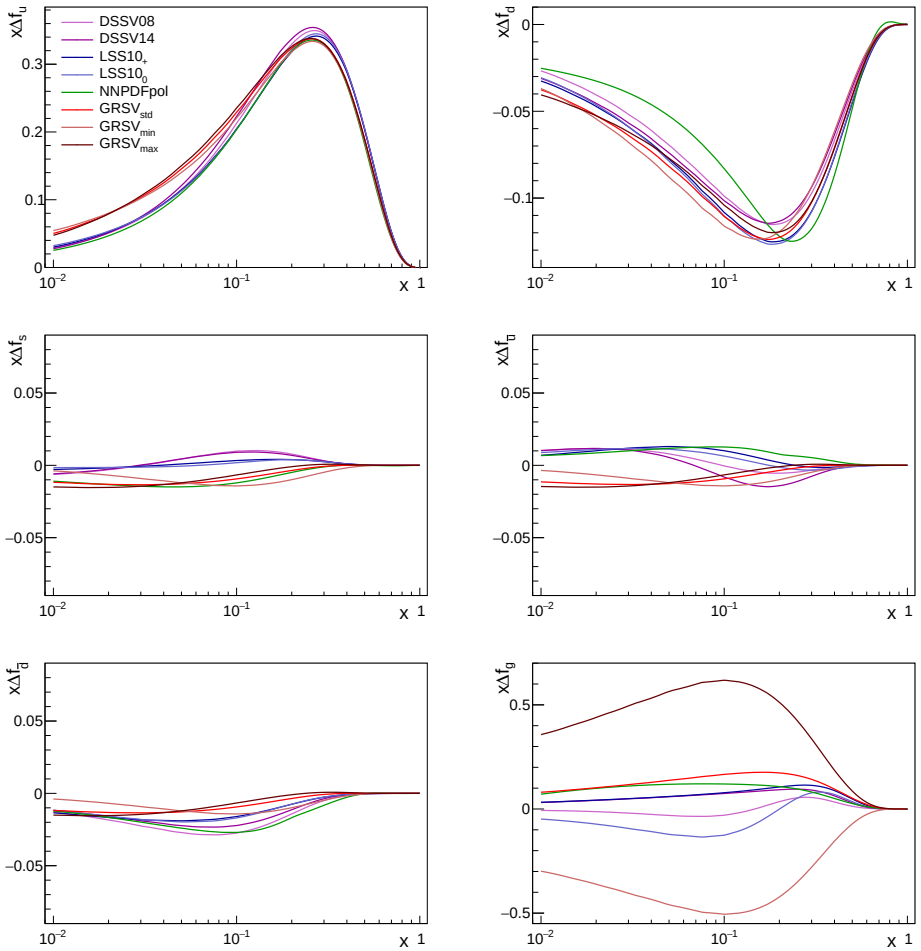

Figure 5.2: Polarized PDFs for quarks, antiquarks and gluons from the global fits DSSV14, LSS10, NNPDFpol and GRSVs. The extreme sets of GRSVs are close to $GRSV_{std}$ for the quarks and are presented only for the gluon distribution.

The fragmentation functions

For the comparison between theory and experiment, we will use the FFs from DSS07 [97], KKP [36], Kretzer [98], DSS14 [99] and LSS15 [100] to look at their impact on the asymmetries. The first three sets are more outdated and do not use all the data currently available.
Unfortunately these sets of fragmentation functions are also used in the extraction of the parton distribution functions from SIDIS data. The possible impact of these FFs sets on the polarised PDFs allows then a systematic uncertainty. The two new sets DSS14 and LSS15 only provide for the moment the fragmentation functions for pion yields, and are thus not complete for a full analysis of unidentified SIDIS reactions.

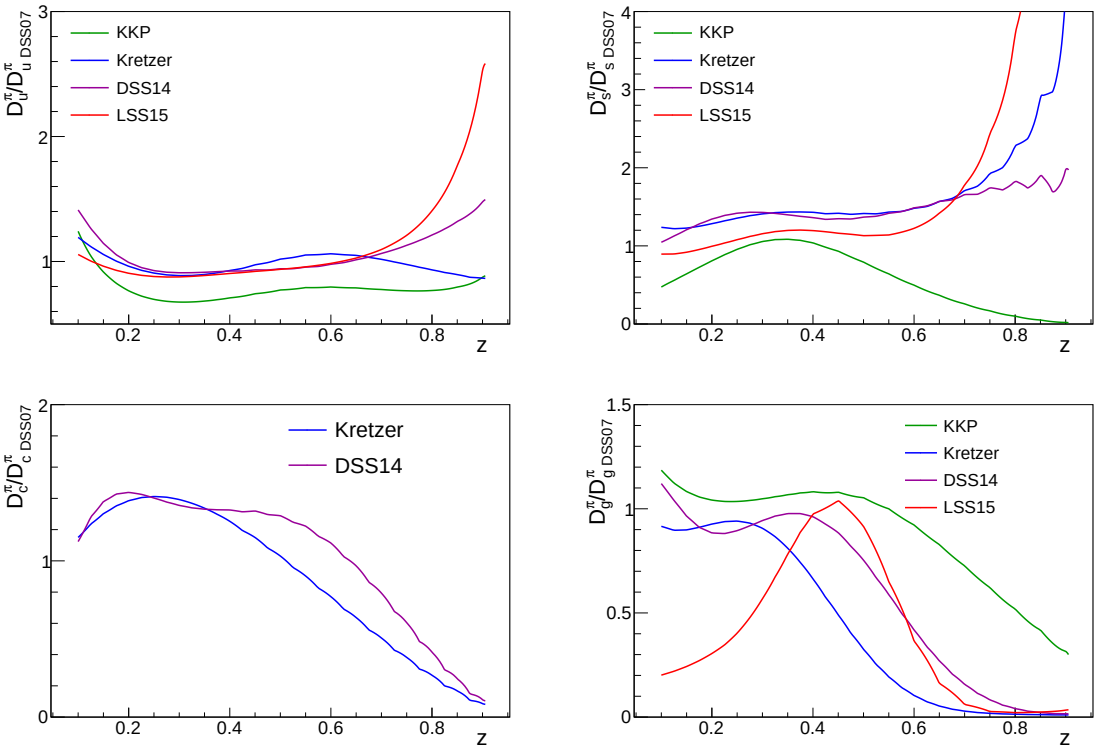

Figure 5.3: Ratio of pion fragmentation functions over DSS07 for u,s,c and g at $\mu^2 = 5\text{GeV}^2$

Every first input presented above is considered the standard one in this comparison analysis: CTEQ65, DSSV14 and DSS07.

5.1 Comparison of theoretical asymmetries computed with different inputs

As presented in Sec. 4.2, the selection of the physical events has quite changed since the theoretical computations done in 2005 by B. Jäger et al. Moreover, the input sets of FFs and polarised PDFs parameterisations that one will use as standard in this final comparison has also evolved since KKP and GRSV parameterisations.

5.1.1 Kinematic Parameters

The different kinematic parameters used in the present analysis differ from the ones in [4]:

- The Q^2_{max} of the Weizsäcker-Williams probability has extended to 1 GeV^2 to have a more significant statistical power.
- The range of the fractional loss of energy was extended for the same reason to $0.1 < y < 0.9$ without problems since the uncertainties due to the parton helicities of the photon are not very important for the interesting range ($p_T > 1.5$ GeV/c)
- As introduced in Sec. 1.2.3, one added a kinematic selection on the fractional energy of the final state hadron $0.2 < z < 0.8$
- As explained in Sec. 4.2.5, the asymmetry have a better sensitivity to ΔG and are better adjusted to the different spectrometer acceptances if they are calculated with a η_h binning [-0.1,0.45,0.9,2.4]

5.1.2 Parameterisation Sets

As presented in the previous section, one will use different default non-perturbative sets for the calculations of the asymmetries:

- The most updated PDFs sets: DSSV14 (the extreme cases of GRSV are still used to visualise the sensitivity to ΔG)
- The most updated and complete sets of FFs DSS07 for unidentified hadrons. Some studies will be performed with DSS14 for identified pions.
- For the parton densities of the photon, we will use the GRS [26] parameterisation (update of the former GRV [35])

5.1.3 Evolution of the Asymmetries

All these changes are presented consecutively in ascending order of the impact on ΔG sensitivity (width of the gap between asymmetries of extreme GRSV parameterisation) for the reaction $\mu d \to \mu' h X$ (Fig. 5.4). Of course, we do not discuss the change of η_h binning already discussed in Sec. 4.2.5 and only present asymmetries integrated over $\eta_h \in [0.45, 2.4]$. The change of polarised PDFs is also presented last since it does not impact the ΔG sensitivity but only represents the best fit to the world data.

As Fig. 5.4 shows, all these changes do not impact much the expectations of the theory, except the change of the FFs, which will be further described in Sec. 5.3. The only notable changes in these asymmetries are produced at low p_T and covered by the uncertainties of the parton helicities of the photon.

5.2 Comparison of asymmetries for unidentified hadrons with theoretical calculations

In the same way as the results were presented in Sec. 4.5.5, the comparison between the experimental asymmetries and the theoretical ones using inputs described in Sec. 5 are presented here for each target material data (deuteron and proton), for each charge of final state hadrons (h^+ and h^-) and for each η_h-bin. Each plot shows the dependence of the asymmetries as a function of p_T.

On every plot, one can qualitatively evaluate the sensitivity of the asymmetries to ΔG by comparing the difference between the extreme $GRSV$ curves with the statistical error bars of

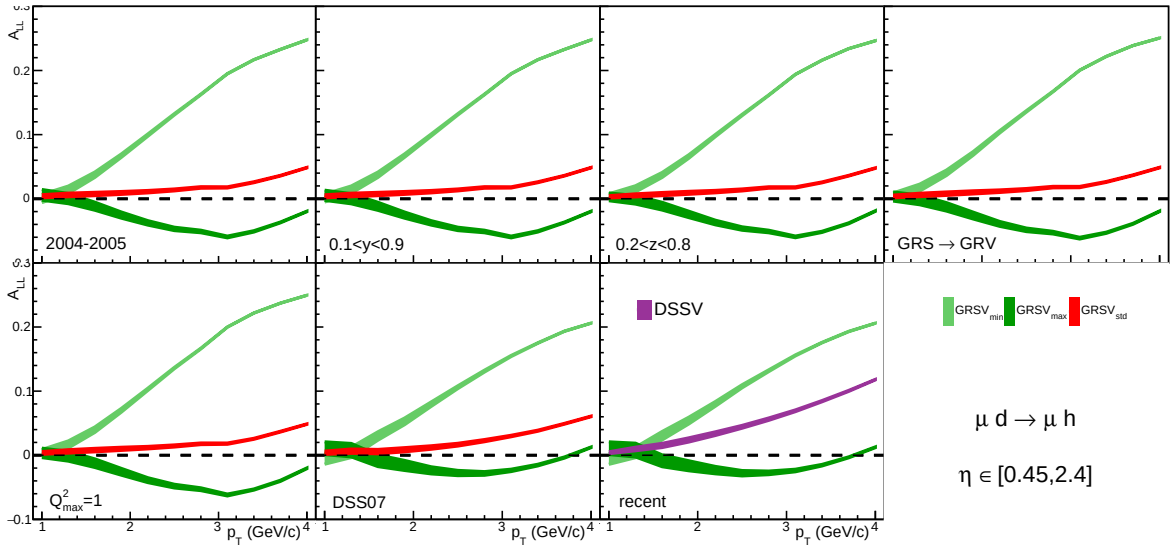

Figure 5.4: Evolution of the theoretical asymmetries from the cuts and inputs in [4] to the most up to date ones for $\mu d \to \mu' h X$. From left to right and top to bottom, one presents the original calculations [4] including one after the other change in y domain, in z domain, with updated parton densities of the photon, with new Q^2_{max} range, with new FFs, and finally the most up to date calculations with new polarised PDFs

the experimental asymmetries (the effect the systematic uncertainties have on the statistical ones would represent less than a 15% increase). In most of the cases, one improves the sensitivity going to higher values of η_h and using the negative hadrons as final state. But of course, to evaluate the final sensitivity to ΔG, all the values are taken into account as in Sec. 4.2.5.

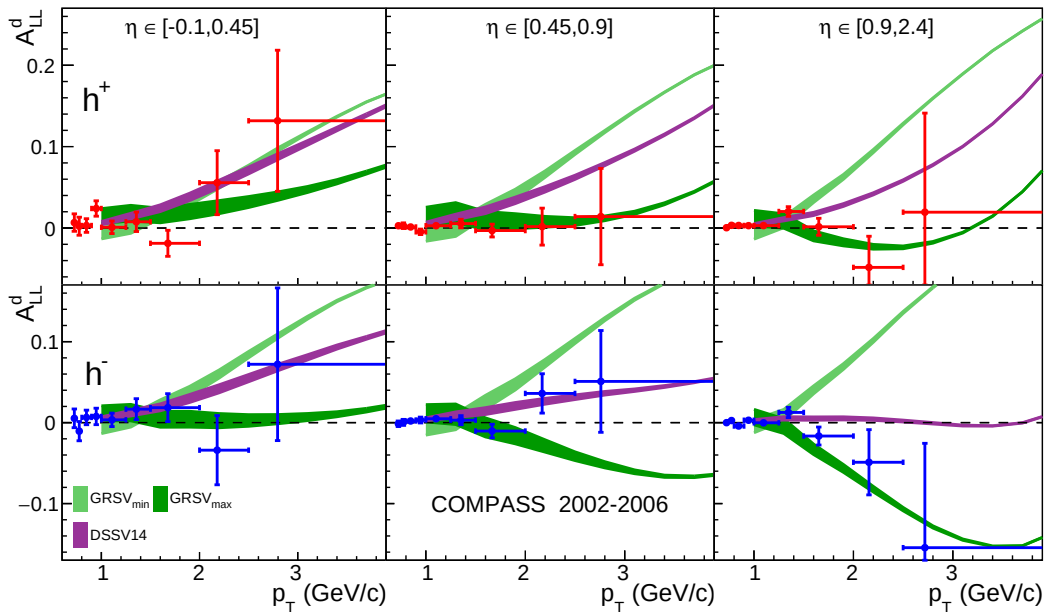

Figure 5.5: Asymmetries $A_{LL}^{d\,h^-}$ (top) and $A_{LL}^{d\,h^-}$ (bottom) for all deuteron data for three bins in η_{cms} [-0.1,0.45,0.9,2.4] compared to theoretical asymmetries for DSSV and extreme GRSV polarised PDFs. DSS07 FFs are used

The first bin in η_h is not really sensitive to ΔG, but allows to check the validity of the theoretical model at low η_h. Indeed for most of these curves, the experimental asymmetries lie between the extreme *GRSV* asymmetries accounting for their statistical uncertainties. The only notable exception to that being the asymmetries for the proton target data for the positive hadrons as final state Fig. 5.6. We will see in Sec. 5.3 that this discrepancy is resolved partly using updated sets of fragmentation functions. Also, the resummation calculations, done so far only for other kinematic domains and for the direct processes case, tend to show an average reduction of the asymmetry by a factor 0.6-0.8.

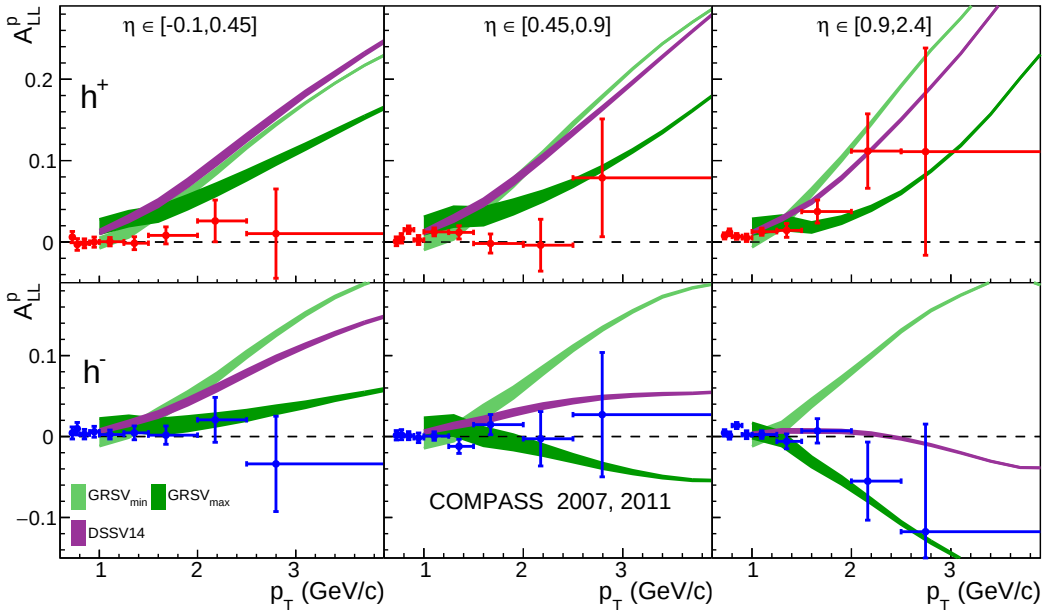

Figure 5.6: Asymmetries $A_{LL}^{p\,h^+}$ (top) and $A_{LL}^{p\,h^-}$ (bottom) for all proton data for three bins in η_{cms} [-0.1,0.45,0.9,2.4] compared to theoretical asymmetries for DSSV and extreme GRSV polarised PDFs. DSS07 FFs are used

5.3 Influence of the FFs on the asymmetries

As shown in Sec. 5.1, the asymmetries are sensitive to the FFs used in the calculations, to the point that it can strongly influence the compatibility between the experimental measurements and the theoretical calculations.

As already mentioned, the most updated FFs set available for parton fragmentation into pions, kaons and protons, DSS07, is quiet different from the most updated ones DSS14 and LSS15, using new measurements from HERMES and COMPASS. Unfortunately, these two sets are only available for pion fragmentation functions, we will therefore compare the asymmetries for the reaction $\mu p \to \mu' \pi$ to study the effect of the FFs on sensitivity of the asymmetries to ΔG. This reaction is chosen because it emphasises the dependence of the asymmetries upon FFs, but the effects are comparable for all the other reactions.

Fig. 5.7 shows the asymmetries integrated over η_h from 0.45 to 2.4 for the latter reaction using different FFs. One clearly sees that the two FFs previously used (KKP and DSS07) lead to different asymmetries, especially for $GRSV_{max}$, thus strongly restraining the sensitivity of the asymmetries to ΔG compared to Kretzer or the newest parameterisations (DSS14 and LSS15).

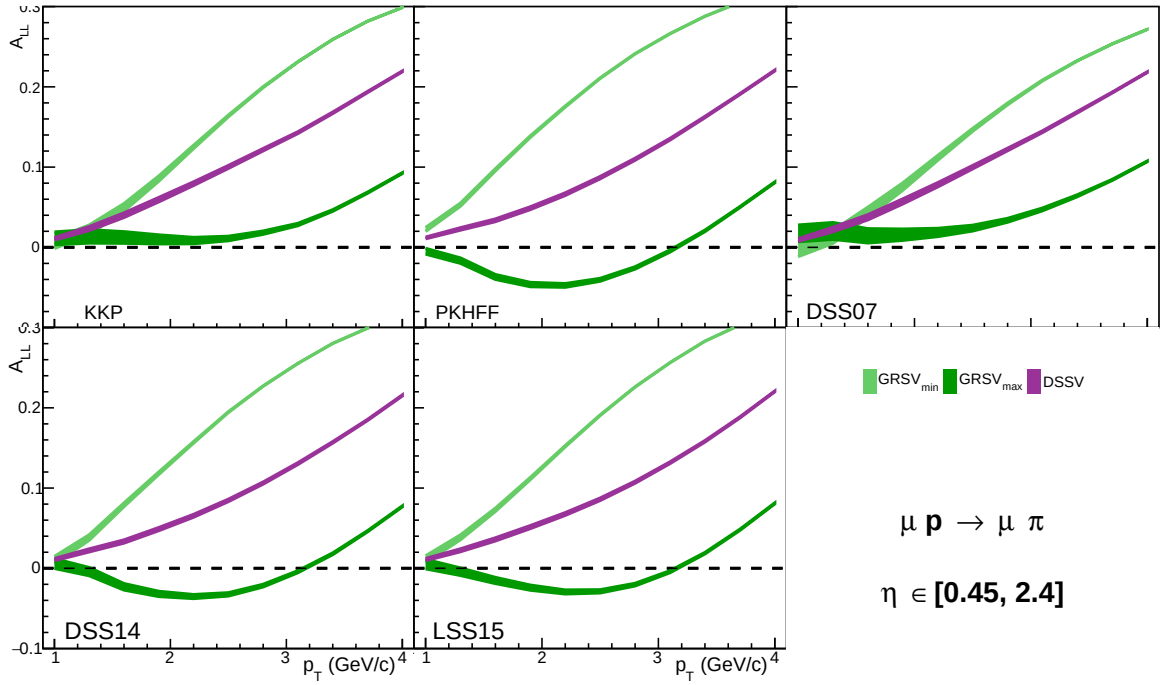

Figure 5.7: Asymmetries $A_{LL}^{p\pi}$ for all the FFs sets available for the three standard polarised PDFs

This seems strange at first order, since the fragmentation functions are not that different, as illustrated in Fig. 5.8 (top) which shows that DSS07 FFs are compatible within Hessian uncertainties to DSS14 FFs, one can wonder how these Hessian uncertainties propagates to asymmetries. Indeed if the uncertainties on the asymmetries were large enough to explain the difference between asymmetries obtained for $GRSV_{min}$ or $GRSV_{max}$ with different FFs, they would become one of the most dominant uncertainties of the asymmetries and would dangerously impact the accuracy of this method to extract ΔG. Fig. 5.8 shows that these uncertainties remain acceptable and do not endanger the possible extraction of ΔG.

However, looking closely to the differences between the FFs sets of Fig. 5.8, emphasized in Fig. 5.3 which shows the ratio of FFs to DDS07 FF, one can see that DSS07 gluon fragmentation into pion differs a lot from other FF sets at high z. In order to test the influence on the asymmetries of this specific D_g^π, we did exchange in the calculations using DSS07 FFs D_g^π with the one from DSS14 set. The effect of D_g^π on the computed asymmetries is summarized in Fig. 5.9, which compares asymmetries with the full DSS07 set, with DSS07 where D_g^π is taken from DSS14, and with the DSS14 set. Although D_g^π does not account fully to explain the difference between asymmetries based on DSS07 and DSS14 sets, it does contribute for a large part to the difference. Based on this finding, and because D_g^π from DSS14 is closer at high z to other FF sets, we use at the end DSS14 FF set for the final comparison between theory and experiment, although we only dispose of the pion FFs for DSS14 and can thus only compute $\mu N \to \mu' \pi X$ asymmetries. It has however been shown in [4] that the computed $\mu N \to \mu' \pi X$ asymmetries are very similar to the $\mu N \to \mu' h X$ asymmetries, so it will very little influence the comparison theory/experiment.

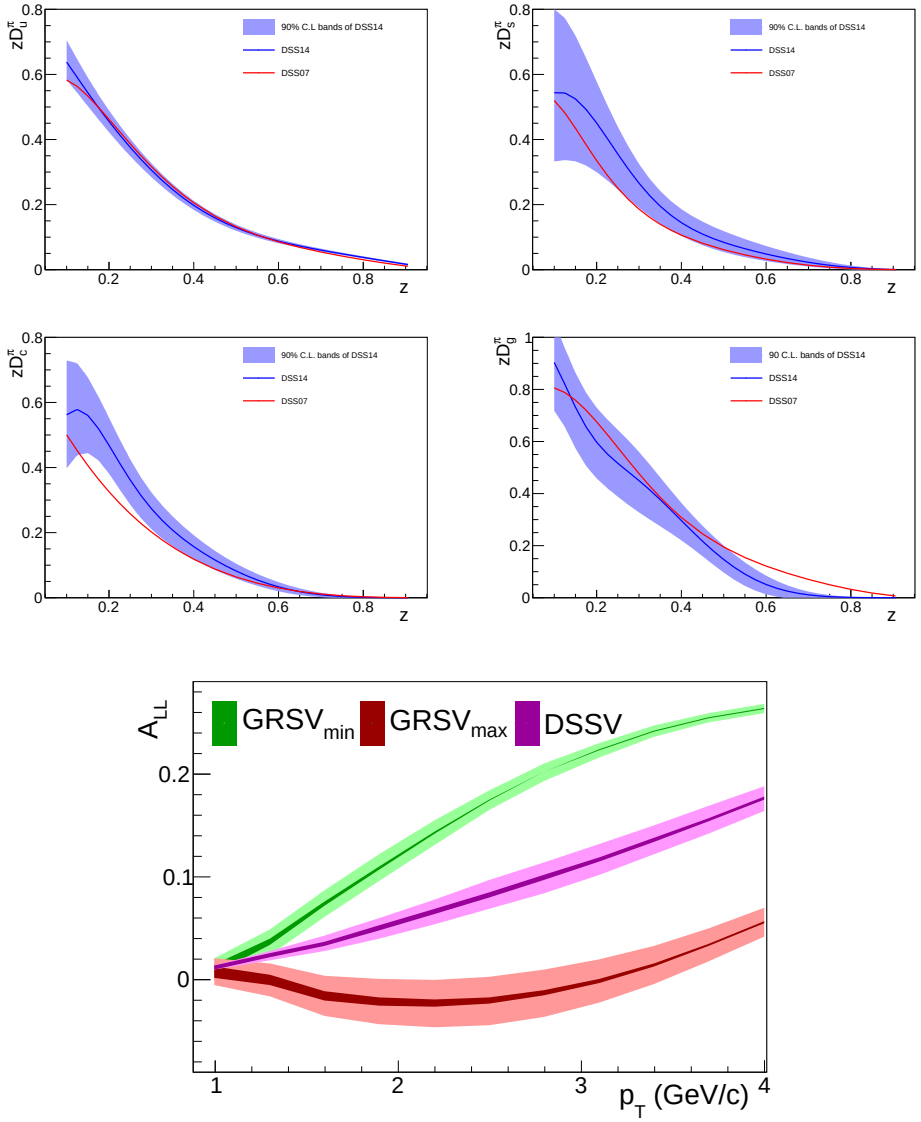

Figure 5.8: $A_{LL}^{p\,\pi}$ for DSS14 FFs with their uncertainty propagation

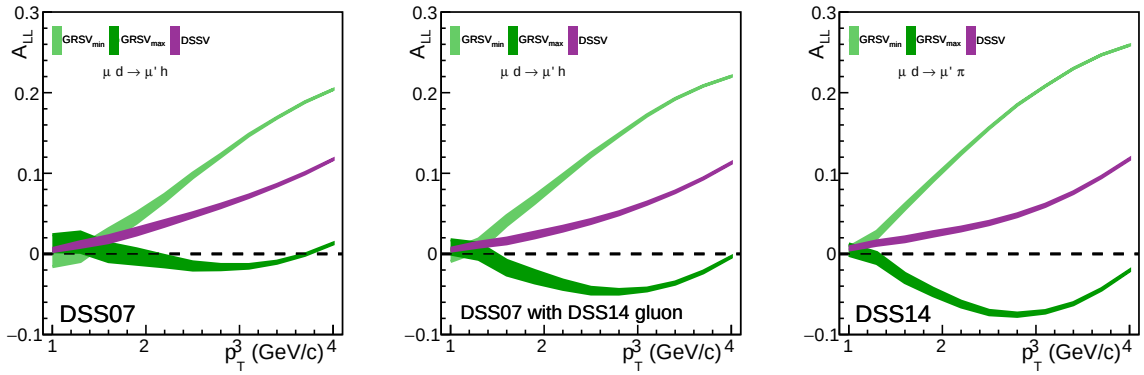

Figure 5.9: $A_{LL}^{d\,h}$ for DSS07 FFs (left) and for DSS07 with D_g^π from DSS14 (center) and $A_{LL}^{d\,\pi}$ for the second η_h bin [0.45,0.9]

Fig. 5.10 and Fig. 5.11 present the final measurements for positive and negative hadrons compared to the theoretical asymmetries computed with DSS14 parton-to-pion FF set.

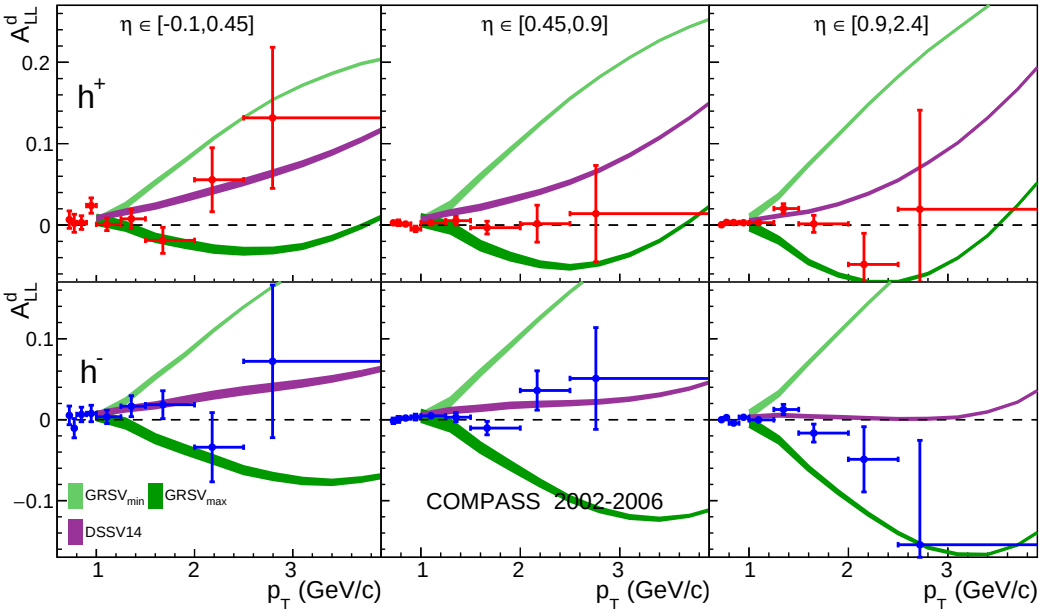

Figure 5.10: Asymmetries $A_{LL}^{d\,h^+}$ (top) and $A_{LL}^{d\,h^-}$ (bottom) for all deuteron data for three bins in η_{cms} [-0.1,0.45,0.9,2.4] compared to theoretical asymmetries for DSSV and extreme GRSV polarised PDFs. DSS14 FFs are used

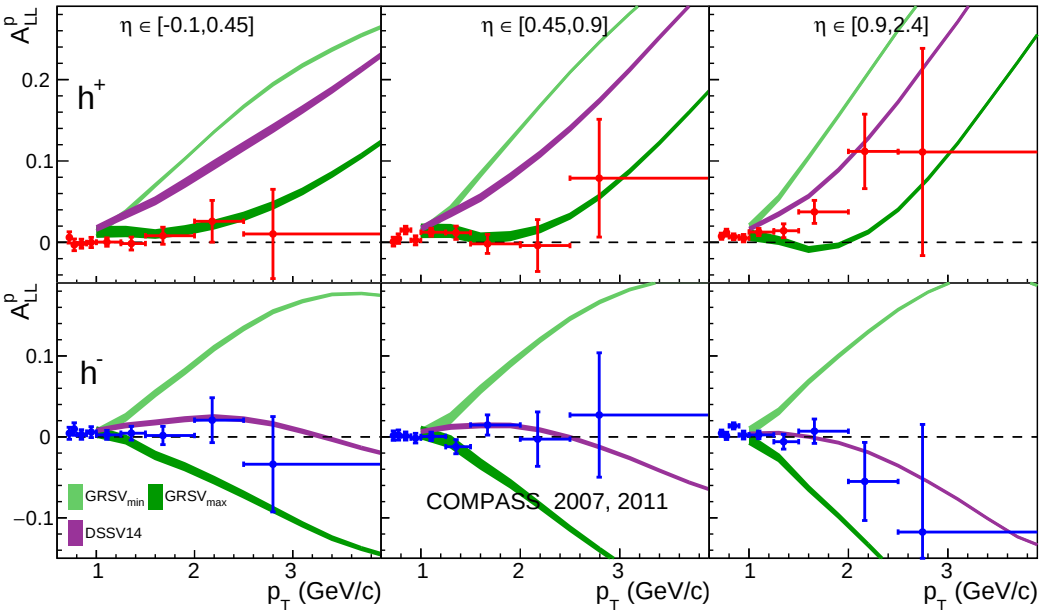

Figure 5.11: Asymmetries $A_{LL}^{p\,h^+}$ (top) $A_{LL}^{p\,h^-}$ (bottom) for all proton data for three bins in η_{cms} [-0.1,0.45,0.9,2.4] compared to theoretical asymmetries for DSSV and extreme GRSV polarised PDFs. DSS14 FFs are used

At this step of the analysis it is complicated to make a definitive statement on ΔG value, the only thing that one can get from the two last η_h-bin is that the experimental asymmetries

seems to lie between the $DSSV$ and $GRSV_{max}$ asymmetries, favouring thus a large positive ΔG.

One will nevertheless try to quantify in more detail the compatibility between the measurements and the different asymmetry calculations in the next section, and evaluate ΔG from the COMPASS asymmetries.

5.4 ΔG^{trunc} for different sets of polarised PDFs

The estimation of ΔG can not be done for $x_g \in [0,1]$ and for any $< \mu^2 >$ from the measurement of only one experiment. The only accessible quantity is ΔG^{trunc} defined as:

$$\Delta G^{trunc} = \int_{x_g^{min}}^{x_g^{max}} dx\, \Delta g(x, < p_T^2 >) \tag{5.1}$$

The first step is then to evaluate the domain $[x_g^{min}, x_g^{max}]$ and $< \mu^2 = p_T^2 >$ and then evaluate the truncated integral for each PDFs set at our disposal.

5.4.1 Evaluation of $< p_T^2 >$

This quantity, which represents the hard scale of our data can be evaluated as:

$$< p_T^2 >= \frac{\int_{h \in data} w p_T^2}{\int_{h \in data} w} \tag{5.2}$$

, where w is a weight taking into account the sensitivity of the data to ΔG. One will use for w the quantity $\beta_{i_\eta, i_{p_T}, year}$ defined in Sec. 4.2.5, that uses the ratio of the difference between the asymmetries of GRSV$_{max}$ and GRSV$_{min}$ over the statistical uncertainties of the data. The expression Eq. 5.2 can then be translated as:

$$< p_T^2 >= \frac{\sum_{year} \sum_{i_\eta} \sum_{i_{p_T}} \beta_{i_\eta, i_{p_T}, year} (p_T^2)_{i_{p_T}}}{\sum_{year} \sum_{i_\eta} \sum_{i_{p_T}} \beta_{i_\eta, i_{p_T}, year}} \tag{5.3}$$

Of course the study in Sec. 5.3 shows that the this sensitivity strongly depends on the choice of the FFs set. One chooses to do the study for DSS07 and DSS14, which give the most different values, given in Tab. 5.2. Since the DGLAP evolution hardly impacts the values at this scale, the value taken in the following studies is $< p_T^2 >= 3$ (GeV/c)^2.

FFs set	DSS07	DSS14
$< p_T^2 >$	3.65	2.91

Table 5.2: Values of $< p_T >^2$ of the data for the asymmetry study for DSS07 and DSS14 FFs sets

5.4.2 x_g distributions

Determining the x_g domain is a little more complicated since one can not access the partonic information of the experimental event in a NLO framework. The usual way of studying this domain is to use Monte Carlo simulation, but here again, they are only available at LO.

To evaluate the limits of the x_g domain, one takes advantage of the form of calculation of the cross-sections presented in Sec. 1.2.2. Indeed the integration is performed via a *Vegas Integration* [101]. To simplify the explanation, the cross-section are calculated for a lot of random

points in the phase space, and are then averaged.

In the theoretical calculations, one can separate the processes by virtually cancelling the parton densities that one does not want to observe as explained in Sec. 1.2.5. For this particular study, only the processes involving the gluon are taken into account: $\gamma g \to cX$, $qg \to cX$ and $gg \to cX$.

In the output of the calculation, the x_g distributions can be plotted to determine the domain relevant to this analysis. Several weights have been envisaged for the x_g distributions:

- the unpolarised cross-sections σ_{ab} which do not take into account the polarised calculations, are dependent of unpolarised PDFs and FFs and under-evaluate the influence of high p_T.

- the unpolarised partonic cross-sections $\hat{\sigma}_{ab}$ which do not take into account the polarised calculations, nor the fact that the gluon have no impact at high x_g, and under-evaluate the influence of high p_T.

- the analysing power $\Delta\hat{\sigma}_{ab}/\hat{\sigma}_{ab}$ which do not take into account the fact that the gluon have no impact at high x_g.

- a pseudo analysing power $\Delta\sigma_{ab}/\sigma_{ab}$ including the PDFs and FFs which is dependent of the polarised PDFs.

The pseudo analysing power and the partonic unpolarised cross-sections are the most unfavourable and will not be used. Since one tries to grasp the shape of the x_g distribution and the analysing power do not allow this at high x_g, it will not be used either, letting only the unpolarised cross-sections as weight for these distributions.

To take into account the sensitivity of the x_g distributions to high p_T, the same method as for the evaluation of $< p_T^2 >$ is used: the x_g distributions are evaluated by bins of η_h and p_T, then summed up using the weight $\beta_{i_\eta, i_{p_T}, year}$ defined in Sec. 4.2.5.

Fig. 5.12 shows these x_g distributions for the three kinds of processes. One compute the limits of the x_g domain by taking the interval at 1 sigma from the mean of the sum of these distributions. The final x_g interval is [0.07,0.25].

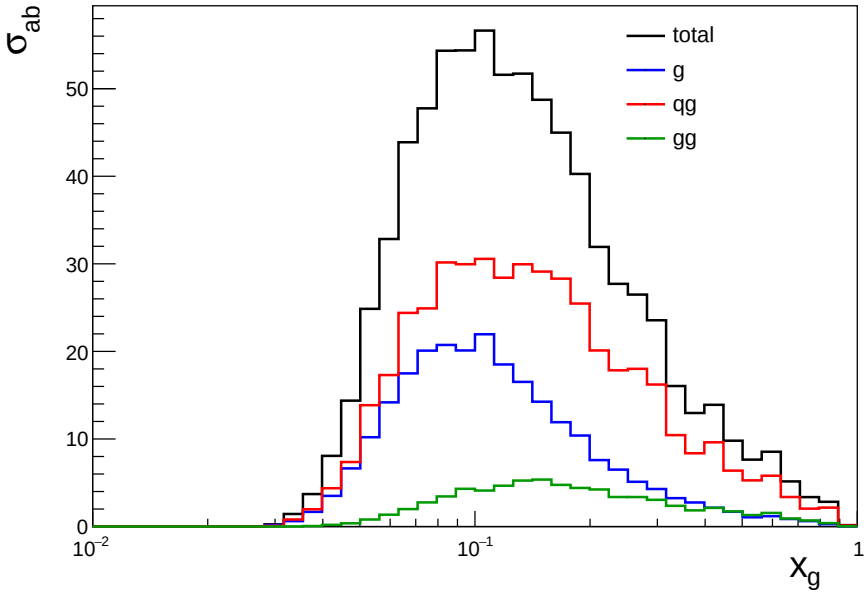

Figure 5.12: x_g distributions by process and summed up

5.4.3 ΔG^{trunc} values

The values of ΔG^{trunc} for all the PDFs sets used in the theoretical calculations are shown in Tab. 5.3 and Tab. 5.4, and they lie all in the interval $-0.67 < \Delta G^{trunc} < 0.82$ and the most recent ones (DSSV14, LSS10, LSS14, NNPDFpol) are in the domain $0.1 < \Delta G^{trunc} < 0.2$. LSS14 is not shown anywhere else in this analysis since it doesn't separate q and $\bar{q}$, which is required to compute the asymmetries.

sets	GRSV$_{min}$	LSS10$_0$	DSSV08	GRSV$_{std}$	GRSV$_{max}$
$\Delta G^{trunc}(\mu^2 = 3)$	-0.620	-0.128	-0.027	0.202	0.736

Table 5.3: Values of ΔG^{trunc} for former standard and extreme PDFs sets for $x_g \in [0.07, 0.25]$ and $< p_T^2 >= 3$ (GeV/c)^2

sets	DSSV14	LSS10$_+$	LSS14	NNPDFpol
$\Delta G^{trunc}(\mu^2 = 3)$	0.087	0.095	0.110	0.139

Table 5.4: Values of ΔG^{trunc} for most updated PDFs sets for $x_g \in [0.07, 0.25]$ and $< p_T^2 >= 3$ (GeV/c)^2

5.5 Extraction of ΔG^{trunc} from the measurements

The experimental asymmetries can now be compared to the theoretical ones using compatibility χ^2 as a quantifier. The goal will then be to evaluate a pseudo ΔG^{trunc} of the measurements by χ^2 minimisation.

5.5.1 Compatibility χ^2

The compatibility χ^2_{PDF} are calculated taking into account both the theoretical uncertainties of the parton densities of the nucleon and the statistical ones coming from the data. It is defined as:

$$\chi^2_{PDF} = \sum_{i_\eta} \sum_{i_{p_T}} \frac{(A_{LL}^{data} - A_{LL}^{PDF})^2}{\sigma^2_{stat}} \tag{5.4}$$

These values are calculated for every sets of PDFs for h, h^+ and h^- as a final hadron state, and for the deuteron and proton asymmetries. These values are also averaged over h^+ and h^-, which gives a more accurate (and somehow different) comparison since it uses a higher number of degree of freedom. And finally the final average between deuteron and proton is calculated to show the final agreement of our data with the theoretical estimations.

Once again these values are also given for theoretical asymmetries calculated with DSS07 and DSS14 FFs since it shows a great impact on the χ^2_{PDF}. These values are given in Tab. 5.5 and Tab. 5.6.

sets	GRSV$_{min}$	LSS10$_0$	DSSV08	DSSV14	LSS10$_+$	NNPDFpol	GRSV$_{std}$	GRSV$_{max}$
$^6LiD + h$	10.26	3.95	3.93	3.87	3.31	3.39	2.01	4.82
$^6LiD + h^+$	4.96	2.53	2.67	2.93	2.5	2.7	1.72	3.9
$^6LiD + h^-$	6.03	2.06	1.9	1.65	1.52	1.43	1.03	2.38
$^6LiD + (h^+ + h^-)$	5.5	2.29	2.29	2.29	2.01	2.07	1.37	3.14
$NH_3 + h$	8.05	6.78	7.77	8.26	7.63	7.39	3.85	5.84
$NH_3 + h^+$	4.82	5.77	6.45	7.16	6.57	6.29	3.69	5.23
$NH_3 + h^-$	4.0	2.0	2.33	2.28	2.19	2.19	1.17	2.17
$NH_3 + (h^+ + h^-)$	4.41	3.88	4.39	4.72	4.38	4.24	2.43	3.7
$(^6LiD + NH_3) + (h^+ + h^-)$	4.95	3.09	3.34	3.5	3.2	3.15	1.9	3.42

Table 5.5: Compatibility χ^2 between experimental and theoretical asymmetries for all the PDFs sets and calculated with DSS07 FFs

The χ^2_{PDF} of Tab. 5.5, based on the use of DSS07 FFs, which are comprised between 1.03 and 10.26 with most of the values between 1.0 and 3.0, what tends to indicate that the measurements fail to clearly differentiate between the different estimations of the asymmetry. That is why one chooses to also do the same comparison with theoretical calculations performed with DSS14 FFs set for pions, even though the data samples contain kaon and other hadrons, since the asymmetries for hadrons and pions remain really close.
The only clear result is that the measurements seem to agree better with sets with larger ΔG^{trunc} (the sets are placed in ascending order of ΔG^{trunc}).

sets	GRSV$_{min}$	LSS10$_0$	DSSV08	DSSV14	LSS10$_+$	NNPDFpol	GRSV$_{std}$	GRSV$_{max}$
$^6LiD + h$	35.11	9.03	6.88	4.14	3.32	2.64	1.77	15.19
$^6LiD + h^+$	18.33	5.49	4.61	3.15	2.47	2.08	1.38	7.37
$^6LiD + h^-$	17.43	4.24	3.0	1.74	1.56	1.25	1.08	8.58
$^6LiD + (h^+ + h^-)$	17.88	4.87	3.81	2.44	2.02	1.67	1.23	7.98
$NH_3 + h$	30.81	13.64	11.71	8.47	7.37	6.01	2.49	4.72
$NH_3 + h^+$	20.0	12.64	11.51	9.63	8.33	6.86	3.54	2.04
$NH_3 + h^-$	11.39	2.82	2.22	1.31	1.28	1.08	0.72	5.46
$NH_3 + (h^+ + h^-)$	15.7	7.73	6.87	5.47	4.8	3.97	2.13	3.75
$(^6LiD + NH_3) + (h^+ + h^-)$	16.79	6.3	5.34	3.96	3.41	2.82	1.68	5.86

Table 5.6: Same as Tab. 5.5 but with theoretical asymmetries calculated with DSS14 FFs

The results of Tab. 5.6, based on the use of DSS14 FFs, show a lot stronger power of discriminating between the different theoretical sets since the χ^2_{PDF} values extend from 1.08 to 35.11. In most cases, the experimental asymmetry agrees best with the set of GRSV$_{std}$, except for the proton data with positive hadron yield, which one already mentioned in Sec. 5.2 is a little outside of the domain of theoretical predictions.

5.5.2 ΔG^{trunc} values

These compatibility χ^2_{PDF} values for different PDFs sets can be used to extract a pseudo ΔG^{trunc} of these COMPASS measurements. Indeed one can consider the χ^2_{PDF} as a function of ΔG^{trunc}_{PDF} and follow a method of χ^2 minimisation by a parabolic function. This method is based on the assumption of a linear effect of the parameterisations on the asymmetries, which is optimistic for such different parameterisations, but this allow us to find an optimal ΔG^{trunc}_{data} for the measurements.

This method was used to try and extract ΔG^{trunc} from the standard theoretical calculations with DSS07. Unfortunately since $\chi^2(\Delta G^{trunc})$ is strictly decreasing in some cases, the optimal ΔG^{trunc}_{data} can either be between the two last points (which is the most probable for these measurements) or outside the last point (GRSV$_{max}$). Since the set of GRSV$_{max}$ is supposed to present the upper constraint on ΔG, the fits converging above have no real physical meaning. This issue is illustrated in Fig. 5.13 where one can see fits converging (for the deuteron data and for proton with h^- yield) and others that can not fit the data (proton data with h and h^+ yields).

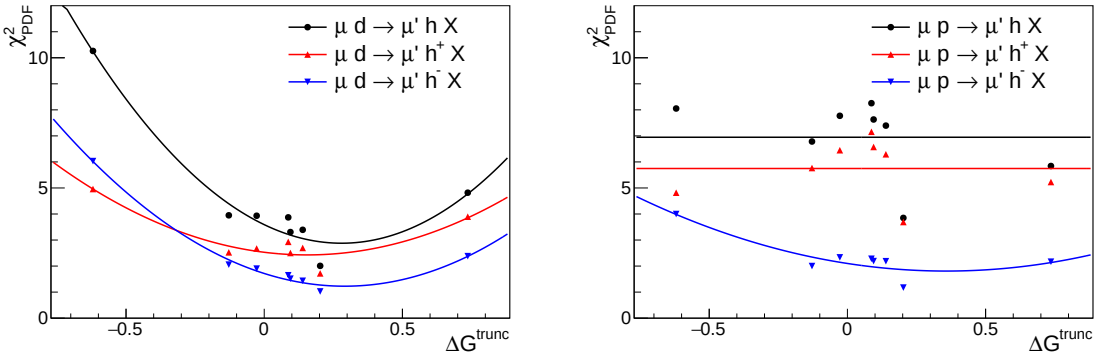

Figure 5.13: Illustration of χ^2 minimisation to extract ΔG^{trunc}_{data} based on DSS07 FFs set: on the left for the deuteron data and on the right for proton data. The straight lines show a non-converging fit for the proton data with positive and all hadron yield.

Since they discriminate more between the different PDFs sets, the theoretical calculations with DSS14 FFs (even with only pion yields) are better suited to extract ΔG^{trunc}_{data}. The values obtained for the different kinds of data are shown in Tab. 5.7. As previously foreseen, the fit for the proton data with positive hadron yield does not converge. All the deuteron data have a really close agreement in their ΔG^{trunc}_{data} value which ranges from 0.25 to 0.31, whereas proton data are more unstable in this manner, certainly because of the issue for the positive hadron asymmetry. By only taking account deuteron data with h^+ and h^- yields, and proton data with h^- yield, the value obtained is $\Delta G^{trunc} = 0.216$. The fits for proton and deuteron χ^2 are illustrated in Fig. 5.14.

target (nucleon)	${}^6LiD$ (deuteron)	NH_3 (proton)	all
h	0.224 (3.5)	0.538 (16.0)	
h^+	0.253 (1.7)	1.301 (17.3)	
h^-	0.197 (0.4)	0.205 (0.3)	
$h^+ + h^-$	0.223 (0.9)	0.520 (5.3)	0.314 (2.6)

Table 5.7: $\Delta G^{trunc}_{[0.07,0.25]}$ for the different targets and the different hadron yields extracted from a parabolic fit based on DSS14 FFs set, with the χ^2 of the fit in parenthesis.

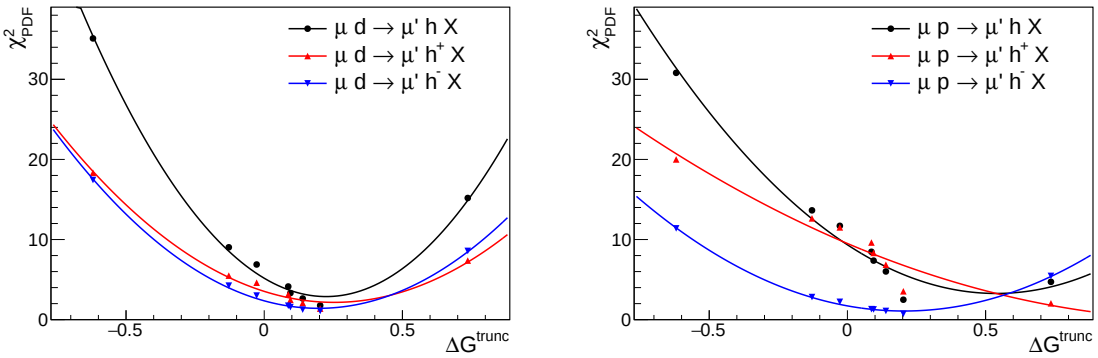

Figure 5.14: Illustration of χ^2 minimisation to extract ΔG^{trunc}_{data} based DSS14 FFs set

The same study can be performed by bin of η_h. As expected it will obviously be more difficult to get a consistent fit at low η_h. Hopefully, as mentioned in Sec. 1.2.3, the impact of the resummations are expected to be stronger as low η_h and could explain these difficulties.

5.6 Outlooks

All the results presented in this section based upon the comparison to theory are naturally preliminary, since there are some fundamental pieces missing on the theoretical side.

Fragmentation Functions

There is no doubt that the changes recently brought to the fragmentation functions greatly impact the asymmetries. The better sensitivity to ΔG allows at least to perform some converging fits to see where the COMPASS measurements are placed among the data used in the different theoretical fits.

These new sets are on the other hand not complete yet. The theorists are missing some information on kaon multiplicities to perform the fit producing the kaon fragmentation functions. This final piece of input would allow this analysis to extract a real ΔG at NLO.

Threshold Gluon Resummation

Naturally the COMPASS measurements can not be explained with a theory only at NLO and require a correction at NLL as explained in Sec. 1.2.3. As mentioned earlier, the calculations have already been done for the direct case and they show a dilution of the asymmetries of a factor 0.6 to 0.8. If this tendency remains, it would bring two opposite consequences to the results:

- the dilution of the asymmetries would bring the asymmetries closer to zero and the sensitivity of the measurements to ΔG would be deteriorated from the same factor.
- the biggest discrepancy between the measurements and the theoretical expectations are for the proton at low η_h for a positive hadron yield. For this particular domain the theoretical asymmetries are positive compared to the experimental ones which are closer to zero. With this kind of dilution effect, the measurements would better agree with the theoretical expectations.

World data Fit

Once all these calculations are done, these double longitudinal spin asymmetries at high p_T and low Q^2 measurement of COMPASS can be added to world data fits like the ones presented in Sec. 5. For these fits, the PDFs are parameterised as Eq. 5.5 for a hard scale reference $\mu^2 = \mu_0^2$ and for a range of longitudinal momentum fraction x representing the domain covered by the whole of the world experiments.

$$x\Delta f(x, \mu_0^2) = Nx^{\alpha}(1-x)^{\beta}(1 + \gamma\sqrt{x} + \eta x) \tag{5.5}$$

The parameter N, α, β and γ are kept free for each distributions taken into account, for example Δu, Δd, $\Delta\bar{u}$, $\Delta\bar{d}$, Δs and Δg; and they are determined by a fit with the world measurements.

For this, all the theoretical expectations for the observable A_1, g_1, A_{LL} and more are calculated with this parameterisation at NLO with the resummations at NLL necessary. The χ^2 between theoretical expectations and measurements are then calculated for the appropriate weight taking into account the uncertainties on the measurements. The best fit is obtained by minimising this χ^2 and the ΔG^{trunc} can be extracted from the Δg distribution.

All along this comparison analysis, one could notice that the theoretical expectations were depending both on FFs and polarised PDFs parameterisations. This is the case for all polarised SIDIS theoretical calculations. Hence doing the fits for FFs and polarised PDFs one after another can introduce a bias that could be solved by performing a common fit for both parameterisations.

Conclusion

The double longitudinal spin asymmetries for single inclusive hadron quasi real photoproduction at high p_T were extracted for all longitudinally polarized data of COMPASS experiment. From 2002 to 2006, the cross-sections for the reaction $\mu d \to \mu' h X$ were taken with a ^{6}LiD target, and for 2007 and 2011 the cross-sections for the reaction $\mu p \to \mu' d X$ were taken with a NH_3 target.

The asymmetries are also extracted for some sub-samples of the data corresponding to different final hadron state yields: h^+, h^-, π^+, π^-, k^+ and k^-. For the identified hadrons (pions and kaons), a method of identification and unfolding hadron by hadron was used to extract these special asymmetries.

This analysis is accompanied with an accurate study of the systematic uncertainties taking into account multiplicative uncertainties, an evaluation of false asymmetries through a time dependent study, and a qualitative study of several unphysical asymmetries.

The theoretical calculations unfortunately do not reach a sufficient order in the QCD perturbations yet to allow to include our data in a global fit with the other world measurements about the spin structure of the nucleon. In order to get a grasp on the relevance of these measurements, the asymmetries are compared with theoretical predictions at NLO for different sets of polarised PDFs.

Before this comparison between theory and experiment, every change of parameter and parameterisation of the theoretical calculations is investigated. This study shows a sensitivity of these asymmetries to the integration interval of η_h and to the fragmentation functions set. In order to minimise the sensitivity to the η_h interval, the asymmetries are extracted from the data in a η_h binning. For the sensitivity to fragmentation functions, the comparison theory/experiment is done for two different parameterisations consisting of the most complete one and the most up to date one.

The comparison study shows experimental asymmetries which mostly lie between the theoretical asymmetries for the current standard PDFs parameterisation (DSSV14) and for a parameterisation maximising the Δg distribution ($GRSV_{max}$), leading to a possible large ΔG estimation. For the NH_3 data with a positive hadron yield at the lower η_h bins, the experimental asymmetries do not lie the range of the theoretical predictions, leading to some interesting expectations for the future NLL resummation calculations, which could explain these discrepancies.

To push further the interpretation of our data, the ΔG^{trunc} are evaluated for $\mu^2 = 3$ GeV^2 and $x_g \in [0.07, 0.25]$, using a χ^2 minimisation method. For the most favorable fragmentation functions set (DSS14), this method gives stable results for the ^{6}LiD data between 0.2 and 0.25 for ΔG^{trunc}. For the NH_3 data, they remain more unstable since they include data which showed discrepancy with the theory. Overall, the value found for this study is $\Delta G^{trunc} = 0.314$ using all data and 0.216 excluding the NH_3 data for a positive hadron yield.

On the experimental side, a first characterisation of the new pixel Micromegas detectors of the COMPASS experiment is performed for the Drell Yan commisionning run of 2014. The main feature of these new detectors is an active pixelised central area. This study is preceded by calibrations to evaluate accurate efficiency, time resolution and spatial resolution. These new detectors show some promising results and are replacing all the Micromegas for the 2015 Drell Yan run.

Bibliography

[1] C. A. Aidala, S. D. Bass, D. Hasch, and G. K. Mallot, Rev. Mod. Phys. **85**, 655 (2013). 7

[2] C. Adolph *et al.*, Physics Letters B **718**, 922 (2013). 7

[3] COMPASS Collaboration, C. Adolph *et al.*, Phys. Rev. D **87**, 052018 (2013). 7, 27

[4] B. Jäger, M. Stratmann, and W. Vogelsang, The European Physical Journal C - Particles and Fields **44**, 533 (2005). 7, 8, 16, 17, 19, 23, 24, 72, 93, 95, 97, 99

[5] D. de Florian, R. Sassot, M. Stratmann, and W. Vogelsang, Phys. Rev. Lett. **113**, 012001 (2014). 7, 14

[6] PHENIX Collaboration, A. Adare *et al.*, Phys. Rev. D **76**, 051106 (2007). 7

[7] STAR Collaboration, B. I. Abelev *et al.*, Phys. Rev. D **80**, 111108 (2009). 7

[8] COMPASS Collaboration, C. Adolph *et al.*, Phys. Rev. D **88**, 091101 (2013). 7, 19, 20, 21

[9] D. de Florian, M. Pfeuffer, A. Schäfer, and W. Vogelsang, Phys. Rev. D **88**, 014024 (2013). 7, 20, 22

[10] E. D. Bloom *et al.*, Phys. Rev. Lett. **23**, 930 (1969). 9

[11] M. Breidenbach *et al.*, Phys. Rev. Lett. **23**, 935 (1969). 9

[12] C. Lorcé, B. Pasquini, and M. Vanderhaeghen, Journal of High Energy Physics **2011** (2011). 11

[13] R. Hofstadter and R. W. McAllister, Phys. Rev. **98**, 217 (1955). 12

[14] D. J. Gross and F. Wilczek, Phys. Rev. Lett. **30**, 1343 (1973). 12

[15] G. Altarelli and G. Parisi, Nuclear Physics B **126**, 298 (1977). 12, 93

[16] A. Buras and K. Gaemers, Nuclear Physics B **132**, 249 (1978). 12, 13

[17] J. Ellis and R. Jaffe, Phys. Rev. D **9**, 1444 (1974). 14

[18] E. Leader, A. V. Sidorov, and D. B. Stamenov, Phys. Rev. D **91**, 054017 (2015). 14, 15

[19] D. de Florian, R. Sassot, M. Stratmann, and W. Vogelsang, Phys. Rev. D **80**, 034030 (2009). 14, 15, 93

[20] M. Alekseev *et al.*, Physics Letters B **676**, 31 (2009). 15, 27

[21] E. Ageev *et al.*, Physics Letters B **633**, 25 (2006). 15, 27

[22] A. Airapetian *et al.*, Journal of High Energy Physics **2010** (2010). 15

[23] M. Stolarski and Compass Collaboration, American Institute of Physics Conference Series **1441**, 244 (2012). 15

[24] E. Leader, A. V. Sidorov, and D. B. Stamenov, Phys. Rev. D **82**, 114018 (2010). 15, 93

[25] M. Klasen, Rev. Mod. Phys. **74**, 1221 (2002). 16

[26] M. Glück, E. Reya, and I. Schienbein, Phys. Rev. D **60**, 054019 (1999). 17, 96

[27] D. de Florian and S. Frixione, Phys. Lett. **B457**, 236 (1999), hep-ph/9904320. 17, 18

[28] C. Bourrely and J. Soffer, The European Physical Journal C - Particles and Fields **36**, 371 (2004). 19

[29] D. de Florian and W. Vogelsang, Phys. Rev. D **71**, 114004 (2005). 19

[30] C. Höppner, PhD thesis, Munich, Tech. U. (2012). 20, 21, 68

[31] G. Sterman, Nuclear Physics B **281**, 310 (1987). 22

[32] S. Catani and L. Trentadue, Nuclear Physics B **327**, 323 (1989). 22

[33] L. G. Almeida, G. Sterman, and W. Vogelsang, Phys. Rev. D **80**, 074016 (2009). 22

[34] J. Pumplin *et al.*, Journal of High Energy Physics **2002**, 012 (2002). 23, 93

[35] M. Glück and W. Vogelsang, Zeitschrift für Physik C Particles and Fields **55**, 353 (1992). 23, 96

[36] B. Kniehl, G. Kramer, and B. Pötter, Nuclear Physics B **582**, 514 (2000). 23, 95

[37] STAR, G. Rakness, Nucl. Phys. Proc. Suppl. **146**, 73 (2005). 23

[38] M. Glück, E. Reya, M. Stratmann, and W. Vogelsang, Phys. Rev. D **63**, 094005 (2001). 23, 93

[39] COMPASS Collaboration, G. Baum, J. Kyynäräinen, and A. Tripet, CERN Report **CERN-SPSLC-96-14** (1996). 27

[40] COMPASS Collaboration, G. Baum, J. Kyynäräinen, and A. Tripet, CERN Report **CERN-SPSLC-96-30** (1996). 27

[41] M. Alekseev *et al.*, Physics Letters B **693**, 227 (2010). 27

[42] Q. Curiel, N. du Fresne, D. Hahne, and F. Thibaud, COMPASS release note (2014). 27

[43] COMPASS Collaboration, CERN Report **CERN-SPSC-2009-025** (2009). 27

[44] COMPASS Collaboration, C. Adolph *et al.*, Phys. Rev. Lett. **108**, 192001 (2012). 27

[45] N. Makke, PhD thesis, Université Paris-Sud XI (2011). 28, 49

[46] C. Iselin, CERN Report **CERN-1974-017** (1974). 28

[47] G. K. Mallot, Thesis, Mainz U. (1996). 29

[48] A. Abragam and M. Goldman, Reports on Progress in Physics **41**, 395 (1978). 29

[49] D. G. Crabb and W. Meyer, Ann. Rev. Nucl. Part. Sci. **47**, 67 (1997). 30

[50] K. Kurek *et al.*, Nucl. Instrum. Methods **485**, 720 (2002). 31

[51] S. Horikawa *et al.*, Nucl. Instrum. Methods **516**, 34 (2004). 32

[52] H. Angerer *et al.*, Nucl. Instrum. Methods **512**, 229 (2003). 32

[53] B. Ketzer, Q. Weitzel, S. Paul, F. Sauli, and L. Ropelewski, Nucl. Instrum. Methods **535**, 314 (2004). 33

[54] C. Bernet *et al.*, Nucl. Instrum. Methods **536**, 61 (2005). 33

[55] H. Pereira Da Costa, PhD thesis, Université Paris-Sud XI (2001). 33

[56] V. Bychkov *et al.*, Nucl. Instrum. Methods **556**, 66 (2006). 33

[57] P. Abbon *et al.*, Nucl. Instrum. Methods **577**, 455 (2007). 34, 39

[58] N. Vlasov *et al.*, Instruments and Experimental Techniques **49**, 41 (2006). 34

[59] P. Abbon *et al.*, Nucl. Instrum. Methods **631**, 26 (2011). 34, 86

[60] C. Bernet *et al.*, Nucl. Instrum. Methods **550**, 217 (2005). 35

[61] H. Fischer *et al.*, Nucl. Instrum. Methods **461**, 507 (2001). 39

[62] H. van der Bij, R. McLaren, O. Boyle, and G. Rubin, Nuclear Science Symposium **1**, 465 (1996). 39

[63] ALICE Collaboration, W. Carena *et al.*, **ALICE-INT-2005-015** (2005). 40

[64] L. Schmitt *et al.*, IEEE Trans. Nucl. Sci. **51**, 439 (2004). 40

[65] K. Kurek *et al.*, Nucl. Instrum. Meth. **A485**, 720 (2002). 41

[66] R. Brun and F. Rademakers, Nucl. Instrum. Meth. **A389**, 81 (1997). 42

[67] E. Rutherford and H. Geigerg, Proceedings of the Royal Society of London A: Mathematical, Physical and Engineering Sciences **81**, 141 (1908). 43

[68] H. Geiger and O. Klemperer, Zeitschrift für Physik **49**, 753 (1928). 43

[69] G. Charpak, R. Bouclier, T. Bressani, J. Favier, and C. Zupancic, Nuclear Instruments and Methods **62**, 262 (1968). 44

[70] W. R. Leo, *Techniques for nuclear and particle physics experiments: a how-to approach* (Springer, 1994). 44, 46

[71] G. Charpak, D. Rahm, and H. Steiner, Nuclear Instruments and Methods **80**, 13 (1970). 44

[72] F. Sauli, Nucl. Instrum. Methods **386**, 531 (1997). 45, 47

[73] Y. Giomataris, P. Rebourgeard, J. Robert, and G. Charpak, Nucl. Instrum. Methods **376**, 29 (1996). 45

[74] M. Vandenbroucke, PhD thesis, Université Pierre et Marie Curie / Technische Universität München (2012). 48

[75] H. Raether, *Electron avalanches and breakdown in gases* (Butterworths, London, 1964). 48

[76] D. Thers, PhD thesis, Université Blaise Pascal (2000). 48

[77] C. Bernet, PhD thesis, Université Paris 7 - Denis Diderot (2004). 48

[78] R. De Oliveira *et al.*, COMPASS Collaboration Meeting (2010). 49

[79] M. French *et al.*, Nucl. Instrum. Methods **466**, 359 (2001). 49

[80] I. Giomataris *et al.*, Nucl. Instrum. Methods **560**, 405 (2006). 50

[81] J.-M. Le Goff, COMPASS note **3** (2004). 65

[82] J. Pretz, COMPASS note **11** (2004). 65

[83] M. Stolarski, PhD thesis, Warsaw U. (2006). 77

[84] A. V. Lipatov and N. P. Zotov, Phys. Rev. D **90**, 094005 (2014). 80

[85] T. Sjöstrand, S. Mrenna, and P. Skands, Journal of High Energy Physics **2006**, 026 (2006). 80

[86] I. Akushevich, H. Bottcher, and D. Ryckbosch, Monte Carlo generators for HERA physics (1998). 80

[87] Q. Curiel, PhD thesis, Université Paris-Sud XI (2014). 85

[88] R. Barlow, Nucl. Instrum. Methods **297**, 496 (1990). 86

[89] Particle Data Group, J. Beringer *et al.*, Phys. Rev. D **86**, 010001 (2012). 87

[90] G. Pesaro, PhD thesis (2010). 87

[91] A. M. F. Sozzi, Paolo. Schiavon, COMPASS note **14** (2006). 87

[92] S. Margulies and J. Phelan, Il Nuovo Cimento A **58**, 804 (1968). 87

[93] A. Martin, W. Stirling, R. Thorne, and G. Watt, The European Physical Journal C **63**, 189 (2009). 93

[94] NNPDF, E. R. Nocera, R. D. Ball, S. Forte, G. Ridolfi, and J. Rojo, Nucl. Phys. **B887**, 276 (2014). 93

[95] D. de Florian, R. Sassot, M. Stratmann, and W. Vogelsang, Phys. Rev. Lett. **113**, 012001 (2014). 93

[96] E. R. Nocera, R. D. Ball, S. Forte, G. Ridolfi, and J. Rojo, Nuclear Physics B **887**, 276 (2014). 93

[97] D. de Florian, R. Sassot, and M. Stratmann, Phys. Rev. D **75**, 114010 (2007). 95

[98] S. Kretzer, Phys. Rev. D **62**, 054001 (2000). 95

[99] D. de Florian, R. Sassot, M. Epele, R. J. Hernández-Pinto, and M. Stratmann, Phys. Rev. D **91**, 014035 (2015). 95

[100] E. Leader, A. V. Sidorov, and D. Stamenov, Workshop on High Energy Spin Physics (DSPIN-13) **15** (2013). 95

[101] T. Ohl, Computer Physics Communications **120**, 13 (1999). 102

université PARIS-SACLAY | ÉCOLE DOCTORALE PHENIICS

Titre: Asymétrie de spin doublement longitudinal dans un régime de photo-production à grands p_T à COMPASS

Mots-clés:

Résumé: Cette thèse présente une nouvelle étude ayant pour but de contraindre la contribution du gluon au spin 1/2 du nucléon. Cette analyse se place dans le cadre théorique de la pQCD colinéaire pour calculer des asymétries de section efficaces pour des hadrons inclusifs à grande impulsion transverse ($p_T > 1$ GeV/c) dans le régime de photo-production quasi-réelle ($Q^2 < 1$ GeV^2). Ces calculs sont réalisés jusqu'à NLO (*Next-to-Leading Order*) avec une inclusion prévue de resommation des gluons au seuil jusqu'à NLL (*Next-to-Leading Logarithm*), qui n'est pour l'instant faite que pour le cas non-polarisé. Cela rend les asymétries sensibles non seulement à la fusion photon-gluon ($\gamma^* g$) mais aussi à des processus de photon résolu tel que qg ou gg.
La mesure des asymétries est réalisée pour toutes les données de COMPASS de 2002 à 2011 avec un faisceau de muons polarisés à 160-200 GeV diffusé sur une cible de deuterium (^{6}LiD de 2002 à 2006) ou de proton (NH_3 pour 2007 et 2011). Ces asymétries sont présentées en fonction de p_T et de la pseudo-rapidité η_h ($p_T \in [1, 4]$ avec $\langle p_T^2 \rangle = 3$ (GeV/c)^2, et $\eta_h \in [-0.1, 2.4]$).
Les calculs de resommation n'étant pas terminés pour le cas polarisé, les mesures sont seulement comparées aux calculs théoriques en utilisant différents jeux de parametrisations de *Parton Distribution Functions* polarisées ayant des valeurs de ΔG assez étendues. Ces comparaisons sont ensuite utilisées pour évaluer le ΔG des mesures.
De façon complémentaire à cette analyse, une étude sur de nouveaux détecteurs, les Micromegas pixelisés, servant à pister le passage des particules, a été réalisée. Après certaines calibrations, ces détecteurs montrent des résultats prometteurs aussi bien en terme d'efficacité qu'en terme de résolution temporelle et spatiale.

Title: Double longitudinal spin asymmetries in single hadron photoproduction at high p_T at COMPASS

Keywords:

Abstract: This thesis presents a new study aiming at constraining the gluon contribution ΔG to the 1/2 nucleon spin. The collinear pQCD theoretical framework, on which it is based, deals with asymmetries calculated from cross-sections for single inclusive hadron in the regime of quasi-real photoproduction ($Q^2 < 1$ GeV^2) at high hadron transverse momentum ($p_T > 1$ GeV/c). These calculations are done up to Next-to-Leading order with a foreseen inclusion of Next-to-Leading logarithm threshold gluon resummation, only performed for the unpolarised cross-sections yet. This makes the asymmetries sensitive to the gluon polarisation not only through Photon Gluon Fusion ($\gamma^* g$) but also through resolved γ^* processes such as qg or gg.
The measurement of the asymmetries is performed for all the COMPASS data available from 2002 to 2011 with a polarised muon beam at 160-200 GeV scattered off a longitudinally polarised target of deuteron (^{6}LiD for 2002-2006) or proton (NH_3 for 2007 and 2011). The asymmetries are presented in bins of p_T and of pseudorapidity η_h ($p_T \in [1, 4]$ with $\langle p_T^2 \rangle = 3$ (GeV/c)^2, and $\eta_h \in [-0.1, 2.4]$).
Since the resummation calculations are not completed yet for the polarised case, the measurements are only compared with theoretical calculations using different parameterisation sets of polarised Parton Distribution Functions with a large range of different ΔG. This comparison is then used to evaluate the ΔG of these measurements.
Complementary to this analysis, a study of new tracking detectors, the pixelised Micromegas, is performed. After calibration, it shows promising efficiencies and time and spatial resolutions.

Université Paris-Saclay
Espace Technologique / Immeuble Discovery
Route de l'Orme aux Merisiers RD 128 / 91190 Saint-Aubin, France